High-temperature induction air heater for Brayton Carnot battery application

A thesis accepted by the Faculty of Energy-, Process- and Bio-Engineering of the University of Stuttgart to fulfill the requirements for the degree of Doctor of Engineering Sciences (Dr.-Ing.)

by

Sergej Belik

born in Samarkand

Main examiner: Prof. Dr. rer. nat. habil. André Thess

Co-examiner: Prof. Dr.-Ing. Egbert Baake

Date of oral exam: 21st November 2023

Institute for Building Energetics,

Thermotechnology and Energy Storage (IGTE)

at the University of Stuttgart

2023

Dedication

Dedicated to the memory of my closest spiritual friend Dr. Kai Holländer, who departed from us during the final stage of my doctoral journey. Beyond being my spiritual brother, he was my writing buddy who earned his Ph.D. with summa cum laude despite facing numerous hurdles caused by the cancer he finally defeated in flames.
As a sympathizer of Buddhism, you have found energy and wisdom in its teachings, particularly during the last year. Your creative spirit and your encouraging attitude were a constant source of enlightenment for everyone. In the words of Buddha:

"In the end, only three things matter: how much you loved, how gently you lived, and how gracefully you let go of things not meant for you."

May this work reflect the spirit of our shared worldly passions and our spiritual friendship that transcends the boundaries of space and time.

Declaration

I hereby certify that this dissertation is entirely my own work except where otherwise indicated. Passages and ideas from other sources have been clearly indicated.

Stuttgart, _____

_____

Sergej Belik

Sergej Belik
June 2023

Acknowledgements

This is the time to thank all the individuals who have inspired and supported me during this exciting research journey. Therefore, I would like to express my gratitude to:

Prof. Dr. rer. nat. habil. André Thess, for believing in me and giving me this one-time chance to prove myself in the interdisciplinary field of thermodynamics and electromagnetism.

Prof. Dr.-Ing. Egbert Baake, for giving me the inspiration for the topic CO_2 emissions of inductive process heating methods and for accepting to co-referee this thesis at XIX International UIE Congress in Pilsen, Czech Republic.

Dr. Volker Dreissigacker and Dr. Stefan Zunft, for their supervision, co-authorship, critical feedback, patient revision of my scientific writing, fruitful discussions, strong support and believe in me throughout these challenging years of various project work and my dissertation.

PD Dr. Marc Linder, Dr. Inga Bürger and Dr. Matthias Schmidt, for being inspiring individuals and exceptional scientists always giving me extraordinary and valuable advice.

Gerrit Lucht, Lukas Hofer and Manuel Moosmann, for providing helpful technical solutions for IVAN and enthusiastically discussing countless technical problems at HOTREG.

Omar Khater, Nataly Segel, Kai Sommer and Thorsten Ott, for the valuable experimental and simulative work giving further insights during their internships and master's theses.

All my colleagues providing an extraordinary and very interesting time at TT: Alex, Andrea, Annelies, Christian, Inga, Jonas, Joni, Jörg, Marc,

Markus, Matthias, Michael, Moritz, Philipp, Sandra, Venizelos, and Wolf-Dieter, as well as Inesa and Moni, for their positive attitudes, their very professional support and organization in the recruitment of students.

And of course, my family and especially my partner Sophie, for her restless support and encouragement particularly at the final phase of this thesis.

Table of contents

List of figures

Nomenclature

Greek Symbols

ε	void fraction
η_{PtH}	electric heating efficiency
η_{rt}	round-trip efficiency
λ	thermal conductivity, W $\mathrm{m}^{-1}\mathrm{K}^{-1}$
ρ	density, kg m^{-3}
τ	duration of charging/discharging, s
Γ	dimensionless heater loss number
Λ	dimensionless heater length
Π	dimensionless heater period duration
Φ	dimensionless heat source number

Indices

in	inlet
out	outlet

s	solid phase
f	fluid phase
el	electrical
th	thermal

Latin letters

a_v	specific surface area, m^{-1}
c_p	specific heat capacity, $\mathrm{J\ kg^{-1}K^{-1}}$
H	total length, m
k	heat transfer coefficient, $\mathrm{W\ m^{-2}K^{-1}}$
$\dot{m}_f$	mass flow rate, $\mathrm{kg\ s^{-1}}$
P_{el}	electrical power input, W
$\dot{Q}_{\mathrm{PtH}}$	Joule heat induced by electrical heating, W
$\dot{q}_{\mathrm{vol}}$	volumetric power density, $\mathrm{W\ m^{-3}}$
St	Stanton number
w_t	specific technical work, $\mathrm{J\ kg^{-1}}$
t	time scale, s
T	temperature, K
V	volume, m^3
w_f	free flow velocity, $\mathrm{m\ s^{-1}}$

Abbreviations

A-CAES	adiabatic compressed air energy storage
A-LAES	adiabatic liquid air energy storage
CAPEX	capital expenditures
CB	Carnot battery
D-CAES	diabatic compressed air energy storage
EES	electrical energy storage
EFH	electric flow heater
ESOI	energy stored on invested
HT	high-temperature
LCOS	levelized cost of storage
PB	pebble bed
PHES	pumped hydro energy storage
PTES	pumped thermal energy storage
PtH	power-to-heat

RESs	renewable electricity sources
RTE	round-trip efficiency
STES	solid media thermal energy storage
TES	thermal energy storage
WF	working fluid
SiC	silicon carbide

Abstract

Future power systems relying on intermittent renewable electricity sources require cost-efficient and energy-efficient electrical energy storage (EES) solutions to ensure a reliable and flexible electricity supply. The Brayton Carnot battery (CB) is an emerging EES option that addresses this need. However, to further improve its cost efficiency and flexibility, this thesis investigates the integration of a compact induction air heater within the Brayton CB. The main objectives of this study are to quantify the tradeoff between system capital expenditures (CAPEX) and round-trip efficiency (RTE) resulting from this integration while developing a novel design solution for such a high-temperature (HT) electric heater component.

A multi-scale approach is employed to achieve these objectives, applying the micro, meso, and macro scales. Technological developments on the micro and meso scales led to identifying an inductively heated pebble bed air heater concept using silicon carbide (SiC) ceramics as a favorable HT induction heater material solution. Experimental results validated the numerical multi-physics model and proved the suitability of this novel HT induction heater solution for integration into the Brayton CB.

A techno-economic analysis was conducted on the macroscale for a Brayton CB air system with a storage capacity of 210 MWh. The findings demonstrated that applying a compact induction air heater based on SiC is a cost-effective solution for reducing system CAPEX. However, the external HT heat integration at 1050 °C was accompanied by a slight decrease in RTE. Thus, a tradeoff was observed between RTE and the system CAPEX, with a 23% reduction in CAPEX achieved at the expense of a 5% decrease in RTE. These results validated the study's main hypothesis, highlighting the remarkable cost advantage of

integrating a compact induction air heater within the Brayton CB. The study contributes valuable insights into developing and integrating the induction air heater solution for HT applications in the Brayton CB and retrofitting natural gas-fired systems in industrial furnaces, such as tunnel kiln. The proposed SiC-based induction air heater concept represents a unique power-to-heat solution for air heating purposes above 900 °C, expanding the existing state of the art in this field.

Altogether, this research provides a comprehensive analysis of integrating an induction air heater in the Brayton CB. The study demonstrates its potential to improve system cost-efficiency while recognizing the tradeoff in RTE. The findings contribute to the advancement of EES solutions and offer practical insights for developing HT heating systems in industrial applications.

Kurzfassung

Zur Gewährleistung einer zuverlässigen und flexiblen Stromversorgung erfordern künftige Stromversorgungssysteme, die sich auf fluktuierende erneuerbare Stromquellen stützen, kosten- und energieeffiziente Lösungen für elektrische Energiespeicher (EES). Die Brayton Prozess-basierte Carnot Batterie (CB) ist eine aussichtsreiche EES-Option, die diesem Bedarf gerecht wird. Um deren Kosteneffizienz und Flexibilität weiter zu verbessern, wird in dieser Arbeit die Integration eines kompakten Induktionsluftheizers in der Brayton-Batterie untersucht. Übergeordnete Ziele dieser Untersuchung sind die Quantifizierung des Zielkonflikts zwischen den Investitionskosten (CAPEX) und dem elektrischen Wirkungsgrad (RTE) des Systems sowie die Erarbeitung einer neuartigen Entwurfslösung für solch einen elektrischen Hochtemperatur-Induktionsheizer.

Um diese Ziele effektiv zu erreichen, wird ein Multiskalenansatz zugrunde gelegt, der eine anwendungsorientierte Technologieentwicklung auf der Mikro-, Meso- und Makroebene forciert. Die Simulationsbasierte Untersuchung auf der Mikro- und Mesoebene ergibt eine Hochtemperaturlösung, welche aus einer induktiv beheizten und mit Luft durchströmten Kugelschüttung aus einer Siliziumkarbid-Keramik (SiC) besteht. Dessen multi-physikalisches Modell wird durch experimentelle Ergebnisse validiert und für den Einsatz in der Brayton CB abgesichert.

Auf der Makroebene wird eine techno-ökonomische Analyse für ein Brayton Prozess-basiertes System mit einer Speicherkapazität von 210 MWh durchgeführt. Die Ergebnisse zeigen kosteneffiziente Systemkonfigurationen mit deutlich reduzierten Investitionskosten, die durch den Einsatz eines kompakten Hochtemperatur-Induktionsheizers auf SiC-

Basis ermöglicht werden. Die Integration von elektrisch erzeugter Hochtemperaturwärme bei bis zu 1050 °C geht jedoch mit Wirkungsgradeinbußen einher, so dass ein Zielkonflikt zwischen dem elektrischen Systemwirkungsgrad (RTE) und der Systemkosten (CAPEX) entsteht. Diese Ergebnisse verdeutlichen das Kostensenkungspotential durch die Integration solch einer kompakten Induktionsheizung und bestätigen damit die Haupthypothese dieser Arbeit.

Weiterhin liefert die Studie wertvolle Erkenntnisse für die Entwicklung und Integration einer solchen Heizerlösung für die Hochtemperaturanwendung in der Brayton Prozess-basierten CB und für die Nachrüstung von Erdgas-befeuerten Systemen in Industrieofenanlagen wie etwa dem Tunnelofen. Das erarbeitete Induktionsheizerdesign stellt eine einzigartige Lösung für Lufterwärmungszwecke oberhalb von 900 °C dar und erweitert den bestehenden Stand der Technik auf diesem Gebiet.

Diese Untersuchung stellt insgesamt eine umfassende Analyse der Integration eines Hochtemperatur-Induktionsluftheizers in der Brayton Prozess-basierten CB dar. Die Studie zeigt das Potenzial zur Verbesserung der Kosteneffizienz des Systems unter Berücksichtigung des elektrischen Systemwirkungsgrads. Die Erkenntnisse tragen zur Weiterentwicklung von kosteneffizienten EES-Lösungen bei und bieten praktische Einblicke für die Entwicklung von elektrischen Hochtemperatur-Heizsystemen für industrielle Anwendungen.

Chapter 1

Introduction

Achievements in developing renewable energy technologies have reduced their cost and improved their performance, leading to the rapid growth of renewable energy sources in the global electricity supply [1]. However, the reduced predictability of intermittent renewable electricity sources (RESs), such as solar photovoltaics and wind power, requires sufficient power system flexibility and reliability. Utility-scale electrical energy storage (EES) technologies can provide a flexible and reliable supply of electricity from RESs at low cost [2], promising to cover the required world energy storage demand of 250 GW by 2030 [3, 4].

1.1 Utility-scale electric energy storage systems

An EES converts electrical energy into another energy form that can be sufficiently stored over days and reconverts it to the initial form when needed. Extensive research has been conducted over the past two decades, proposing various solutions for medium-duration and utility-

scale EES technologies. Xue et al.[5], Luo et al. [6], and Olympios et al. [7] provided a comprehensive review of such EES for load-balancing applications in power systems. Most of the reviewed works have conducted a technical analysis [5–8], while some have evaluated the economics, giving cost estimations for initial investment cost [6, 7]. However, only a few works [8, 9] have assessed investment and operational costs together with round-trip efficiency (RTE) over the system lifecycle.

Jülch [8] and Smallbone et al. [10] presented a cost metric that considers the RTE and enables the comparison of EES system cost consistently over their lifecycles. The proposed levelized cost of storage (LCOS) indicates the ratio of discounted costs to dispatched electricity over the lifecycle. The LCOS method was used to analyze medium-term EES with 100 MW power output and 400 MWh energy storage capacity. The results indicated LCOS of up to 130 €/MWh for commercially-available EES solutions such as pumped hydro energy storage (PHES) and diabatic compressed air energy storage (D-CAES). Battery energy storage systems such as lithium-ion (Li-ion) and vanadium redox flow were expected to become competitive with similar LCOS by 2030 [8]. However, recent cost reductions driven by economies of scale have led to current economics, launching EES projects with 524 MWh Li-ion batteries in Idaho (US) [9] and 800 MWh vanadium redox flow batteries in Dalian (China) [11]. Emerging EES technologies with LCOS below 150 €/MWh [8] are adiabatic compressed air energy storage (A-CAES) and Brayton pumped heat energy storage, also referred to as Brayton pumped thermal energy storage (PTES) or the Brayton Carnot battery (CB).
For a comprehensive overview of CBs, references [12–15] can be consulted, while Rabi et al. [16], Budt et al. [17], and de Sisternes et al. [18] presented the state of the art of CAES.

Although the LCOS is an appropriate indicator for investment planning that considers RTE, accumulated costs, and cycle stability over the expected operating life of the EES, it omits the energy efficiency aspect concerning primary energy demand. Therefore, Barnhart et al. [19] proposed the energy stored on invested (ESOI) metric derived from the energy returned on energy invested ratio (EROI). This metric quantifies the amount of energy stored by an EES compared to the primary energy required for its manufacture and installation. The authors used the ESOI to compare various utility-scale EESs regarding energy efficiency. This comparison revealed that battery energy storage systems store a maximum of 10 times (ESOI = 10 for Li-ion) the energy required to build them. In contrast, thermo-mechanical EESs such as CAES (ESOI = 240) and PTES (ESOI = 210) have much higher energy efficiency. Although these thermo-mechanical EESs are highly energy-efficient (high ESOI) and cost-efficient (low LCOS), they depend on particular geographical morphologies, such as large water reservoirs for PHES or large underground caverns for both CAES technologies. An additional drawback of the D-CAES concept is the system's inherent limitation in RTE [9, 11]. In contrast, Brayton CB is independent of geographical constraints; its RTE is only limited by component irreversibility but additionally benefits from high energy density, a high ESOI, and a low LCOS [7–9, 12–14].

The Brayton CB operates based on the reversible Brayton cycle, which most widely uses air, nitrogen, or argon as the working fluid (WF) [7]. In this storage system, electric energy is used to transform low-temperature heat into high-temperature heat and store the thermal energy in two thermal energy storage (TES) systems, one for low temperatures and pressures and the other for high temperatures and pressures. The TES systems usually comprise solid media thermal energy storage (STES) or liquid phase two-tank storage. While state of the art atmospheric

liquid phase two-tank storage systems with nitrate molten salt ($T_{max} < 565$ °C for nitrate molten salt [7]) require an additional heat exchanger for the heat transport to the WF, the pressurized STES system is characterized by direct heat transfer from the storage material to the WF and is limited to the operating temperature in the range of 500 °C to 1050 °C [9, 12, 14]. During the discharging period, the stored thermal energy is converted back into electrical energy using a gas turbine cycle. The excess heat leaving the gas turbine is given to the low-temperature TES system to cyclically provide heat for the heat pump cycle. In addition, the Brayton CB system comprises two compressors and two expanders, one each for the charging and discharging cycles. The idea of PTES was developed a century ago by Maguerre [21] and proposed by various authors during the 20th century as a suitable solution to improve the operational flexibility of fossil-fired power plants [22]. Then, as the penetration of RESs into the power system increased in the last decades, the need for supply security and grid stability prompted adapting of the Brayton CB concept for grid-scale load-balancing applications.

The most popular Brayton CB systems that have been patented to address this application are the Saipem S.A. [23] and Isentropic Ltd. [24] grid-scale CB systems. Both use argon as a WF for direct heat transfer to the STES systems. Desrues et al. [25] first modeled the recuperated Brayton CB system proposed by Saipem S.A. with an energy storage capacity of 602.6 MWh and a power output of approximately 100 MW. This system employs four axial turbomachines for compression and expansion to achieve a RTE of 67%, with maximum and minimum system temperatures of 995 °C and – 73 °C, respectively.

Moreover, Howes [26], White et al. [27, 28], and McTigue et al. [29] introduced, analyzed, and optimized a 16 MWh/2 MW system patented by Isentropic Ltd. [24], which stores thermal energy at a maximum

of 600 °C and a minimum of –164 °C in two packed-bed STESs using only two reciprocating piston engines for compression and expansion. This system achieves a RTE of 59% and 87%, respectively, considering piston engines' polytropic efficiency of 0.90 and 0.99 [24]. The first experimental results from the recently commissioned 600 kWh/150 kW demonstrator revealed a RTE of 73.1% for a single-cycle operation with a polytropic efficiency of 0.98 at full-load conditions, using argon as the WF [30]. However, considering mechanical and electrical losses, the system demonstrated a total RTE of 54.6%.

Although these studies marked significant progress in the technical development of Brayton CB solutions for the power grid, the current revenue options from energy arbitrage and frequency regulation are insufficient to cover the high capital expenditures (CAPEX) and overcome the barriers to market integration [31, 32]. Hence, it is crucial to focus on improving cost-efficiency and system performance to promote the economic feasibility of Brayton CB systems. Therefore, the concept of utilizing power-to-heat (PtH) in A-CAES inspired by Dreissigacker and Belik [33] was adapted to Brayton CB systems by incorporating an electric flow heater (EFH) component into the heat pump cycle, as illustrated in Figure 1.1.

1.1.1 Motivation and objectives

The underlying idea for cost-efficiency and system performance improvements is based on integrating an EFH downstream of the heat pump compressor. In addition to the heat provided by the compressor, high-temperature heat is generated by Joule heating and transported to the hot STES, where it is stored at a high-temperature level using low-cost storage materials [34]. During the discharging period, the hot STES provides this high-temperature heat to power the heat engine cycle by reversing the flow direction of the WF. As a result,

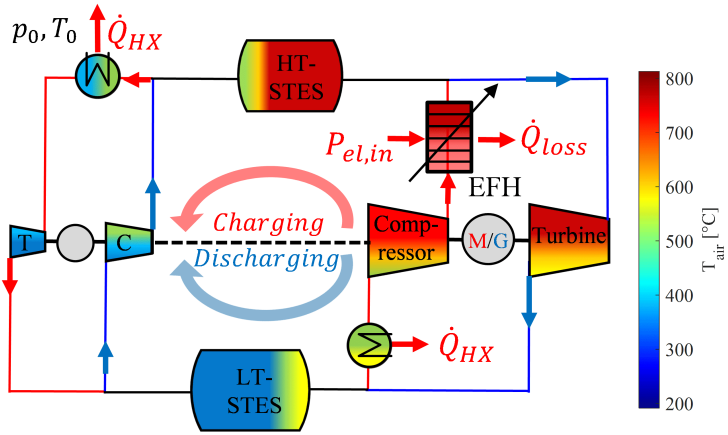

Fig. 1.1 Schematic of Brayton CB configuration with an additional power-to-heat unit (electric flow heater – EFH).

the utilization of additional PtH increases the power output and the energy density of the system, leading to two major benefits. Firstly, providing heat at various temperature levels to the heat engine cycle independently from the operating pressure of the heat pump improves the system's performance, enabling a high electrical power output for a lower pressure setting while maintaining a high system temperature. Secondly, it reduces the components' required size and equipment cost, significantly improving cost efficiency. However, the major drawback of PtH integration is decreased RTE due to process irreversibilities accompanied by the limited Carnot efficiency of the gas turbine cycle. Therefore, the key challenge addressed in this thesis is quantifying the tradeoff between the costs and RTE, which strongly depends on the quality of the EFH component.

Previous research has not extensively explored the impact of adding electric heating to Brayton CB systems on cost efficiency and RTE. Benato [34] and Chen et al. [36] proposed integrating an electric heater between the heat pump compressor and hot STES to reduce the cost of the compressor by limiting its capability. Benato achieved the cost limitation by reducing the compressor pressure, limiting its outlet temperature to 550 °C while using the EFH to raise the STES inlet temperature to 1050 °C. Results of this techno-economic assessment indicated a 105% increase in STES energy density to 430 kWh/m^3, a 35% cost reduction to 54 $/kWh, and an unexpected improvement in RTE from 6.3% to 7.0%. Moreover, Chen et al. [36] presented a hybrid system with a bottoming organic Rankine cycle requiring an EFH outlet temperature of 1127 °C, resulting in more than double the energy density to 62.2 kWh/m^3, but a 5.89% lower RTE compared to operation without the EFH.

Although both studies demonstrated the increase in energy density demanding high EFH outlet temperatures above 1000 °C, neither revealed technical details on the PtH concept, EFH component shape, size, or dimension. Moreover, Benato's assessment showed an unexpected improvement in the RTE alongside cost reduction, which is usually a tradeoff. Therefore, this research aims to address these knowledge gaps by answering two central research questions:

1. What impact does the electric flow heater have on the system cost and round-trip efficiency of the Brayton CB?
2. Which electric flow heater concept, design, and heating material are suitable to meet the requirements of a Brayton CB application?

This thesis hypothesizes that PtH integration offers a significant cost advantage for the Brayton CB system when a compact EFH component

is added downstream of the HP compressor. Consequently, this research aims to achieve primary, secondary, and tertiary objectives. The primary objective is to investigate the influence of additional PtH integration on system costs and RTE. The secondary objective is to elaborate and verify a novel design solution with suitable heating element material for the EFH that meets the application-specific requirements of a Brayton CB. Moreover, a time-efficient design tool is essential as a modeling basis for design studies on a system level. Therefore, the tertiary objective is to provide a compact and time-efficient electrothermal model that specifies the EFH size for further techno-economic analysis addressed in the primary objective.

Overall, achieving these thesis objectives will advance knowledge in the field of EFH and provide essential insights into the potential of PtH as a practical and cost-efficient solution for facilitating the development of cost-effective and sustainable Brayton CB systems.

1.1.2 Methodology and contributions

A multi-scale approach was applied to address the central objectives and research questions, where each of the research questions and the associated objectives were allocated to the macro, meso, and micro scales of Figure 1.2.

According to this holistic approach, the energetic and economic impact of the EFH component on the Brayton CB system was investigated at the system scale (paper III) using wide-ranging parameter studies with varying technical and economic parameters. This extensive simulation study required easy-to-implement and time-efficient component models to obtain reliable findings. Therefore, a compact design model for the EFH component was developed at the meso scale (paper II), using simplifications for the detailed numerical model from the micro scale.

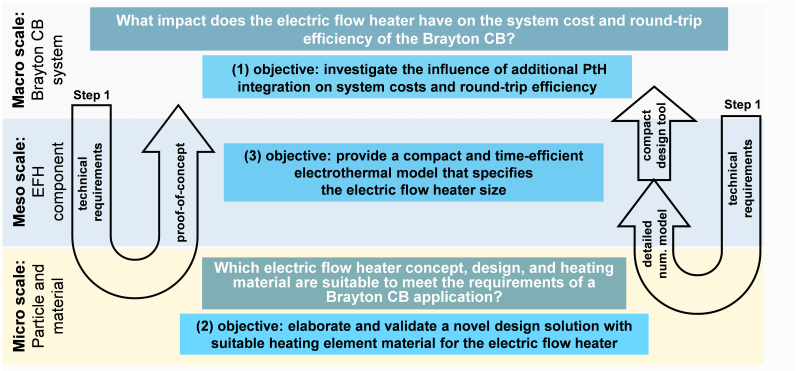

Fig. 1.2 Research questions and objectives embedded in the multi-scale approach.

In parallel, a technical solution was provided for the heater concept elaborated at the micro scale (paper I), where technical aspects of the electrothermal process, its multi-physical phenomena, and material aspects were addressed in a detailed modeling approach. Moreover, the numerical and experimental investigation on this deepest scale provided the in-depth process understanding needed to prove the elaborated concept solution for the technical requirements of the Brayton CB system. Therefore, the initial step in this thesis was the definition of the technical requirements in Sec. 2.1, in descending order from system to component and material scales, to obtain application-specific findings for developing the EFH solution.

In Figure 1.2, the findings were obtained in ascending order from the micro and meso scales, contributing to the primary objective of this thesis at the macro scale. This methodology allowed for the following crucial *contributions* in nine steps, starting with defining the technical requirements based on idealized system simulation without EFH design

and cost data at the macro scale. The approach completed with a loop at the same scale, assessing system costs and RTE using a specified EFH design solution with its corresponding equipment cost.

1. Definition of key technical requirements for the EFH from the idealized system model

These requirements were given at the micro scale for the following:

2. Comparison of PtH technologies and specification of the EFH concept: a high-temperature *EFH concept solution*

3. Identification of a suitable material solution (Sec. 2.2.4.5): *Efficient high-temperature ceramic material* for operation temperatures above 1000 °C

4. Model development of the EFH concept solution (Sec. 2.2.2.2): A *numerical multi-physics model* for calculating the distribution of the temperature field, velocity field, volumetric heat generation, power density, and efficiency

5. Proof-of-concept and model validation (Sec. 2.2.1.2 and Sec. 2.2.4.1): Laboratory setup of the EFH concept, its *experimental proof* for the application in Brayton CB, and the *model validation*

This EFH concept with the validated numerical model was given to the meso scale for the following:

6. Model simplification: *A compact and dimensionless Φ-Λ-St model* for time-efficient calculations and comparison with other EFHs concepts and their characterization

7. Verification of the simplified model: *a verified and easy-to-implement universal modeling approach* for time-efficient design studies at the macro scale.

The elaborated and proofed EFH solution and its validated and simplified modeling approach were implemented at the macro scale for techno-economic analysis of the Brayton CB with PtH extension, including the following:

8. Upscaling of the EFH solution and design study (Sec. 2.4.5): A *compact and modular EFH solution* with high power density to achieve a high outlet temperature while reducing system costs

9. Quantification of the tradeoff (Sec. 2.4.5.3): The *tradeoff between system costs and RTE* proves that the incorporation of additional high-temperature heat reduces the system costs along with the RTE.

These contributions verified the main hypothesis of this work that PtH offers significant cost leverage for the Brayton CB system when a compact EFH component is incorporated downstream of the heat pump compressor.

Chapter 2

Publications

This thesis builds upon the research work published in the following journals and conference contributions. The research work is specifically described in Secs. 2.1–2.4, starting with a preliminary study (Sec. 2.1) introducing the EFH concept and defining its requirements for the contribution on the micro scale (paper I) from Sec. 2.2. The subsequent sections present the contributions in ascending order from micro to macro scale (paper II) from Sec. 2.3 and (paper III) from Sec. 2.4, addressing the main hypothesis of this thesis that is illustrated together with the publications in Figure 2.1.

Preliminary studies: introduction of the induction air heater concept and definition of technical requirements:
Proceedings of UIE 2021: XIX International UIE Congress on Evolution and New Trends in Electrothermal Processes 1.-3.2021, Pilsen, Faculty Electrical Engineering, University of West Bohemia, 2021, pp. 45–46. https://doi.org/10.3390/app130423

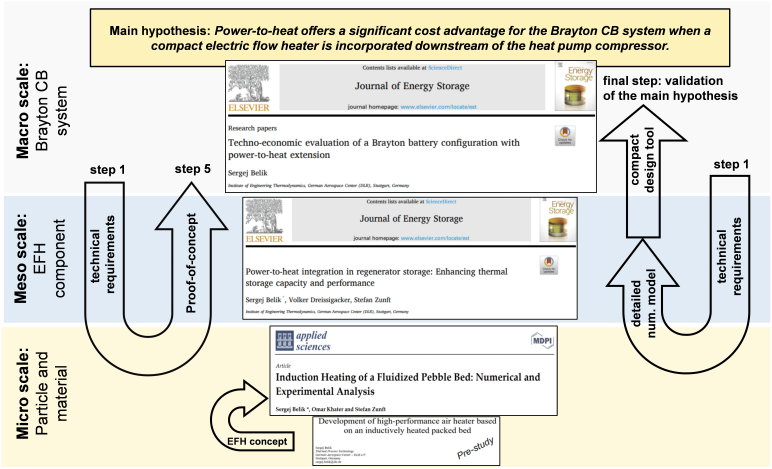

Fig. 2.1 Contributions addressing the main hypothesis applying the multi-scale approach from Figure 1.2.

This study was published in 2021 in the Proceedings of the XIX International UIE Congress in Pilsen. It presents an experimental concept study and preliminary results for the selected induction air heater concept. In contrast to this preliminary study, the subsequent journal contributions adopt a holistic multi-scale approach to form a consistent trilogy.

1. Paper I (micro scale): Material identification, numerical modeling, experimental validation and proof-of-concept
Belik, S.; Khater, O.; Zunft, S. Induction Heating of a Fluidized Pebble Bed: Numerical and Experimental Analysis. Appl. Sci. 2023, 13, 2311. https://doi.org/10.1016/j.est.2022.104570.

2. Paper II (meso scale): Development of a compact EFH design model

Belik, S., Dreissigacker, V., & Zunft, S. (2022). Power-to-heat integration in regenerator storage: Enhancing thermal storage capacity and performance. Journal of Energy Storage, 50, 104570. https://doi.org/10.1016/j.est.2022.104570.

3. Paper III (macro scale): Verification of the main hypothesis through techno-economic system analysis and evaluation

Sergej Belik. Techno-economic evaluation of a Brayton battery configuration with power-to-heat extension. Journal of Energy Storage, Volume 68, 2023, 107416, https://doi.org/10.1016/j.est.2023.107416.

Further contributions referenced in this thesis have been published as follows:

Belik, Sergej (2019) Power-to-Heat Integration in Solid Media Thermal Energy Storage: Increasing System Cost Efficiency and Flexibility. 13th International Renewable Energy Storage Conference, 12.-14. Mar. 2019, Düsseldorf, Germany.

Dreißigacker, Volker, and Sergej Belik. (2019). "System Configurations and Operational Concepts for Highly Efficient Utilization of Power-to-Heat in A-CAES" *Applied Sciences* 9, no. 7: 1317. https://doi.org/10.3390/app9071317.

Belik, Sergej (2020): Power-to-Heat integration in Brayton Battery: Increasing System Cost Efficiency and Flexibility. IWCB 2020, 14.-16. Sep. 2020, Stuttgart, Germany.

Belik, Sergej (2021): Techno-economic evaluation of a Brayton Battery configuration with Power-to-Heat extension. 15th International Conference on Energy Storage (ENERSTOCK 2021), June 9-11, 2021, virtual conference, (originally scheduled in Ljubljana, Slovenia).

Belik, Sergej (2022): Power-to-Heat integration in a two-stage Brayton Battery: Increasing System Cost Efficiency and Flexibility. 3rd International Workshop on Carnot Batteries, 27.-28. Sep. 2022, Stuttgart, Germany.

Belik, Sergej und Dreißigacker, Volker (2022) Entwicklung eines neuartigen Induktionsheizers für CO_2-neutrale Industrieprozesse. 8. Dialogplattform Power to Heat 2022, 15. Dez. 2022, Berlin.

Belik, Sergej (2023): Brayton Carnot battery configuration with extended induction air heater: A techno-economic assessment. Helmholtz Energy Conference 2023. 12-13 June. 2023, Koblenz, Germany.

Belik, Sergej (2020): WO2020239288A1 and EP3824228A1. Heat accumulator apparatus and method for storing and/or transferring heat, March, 24th 2020 (Priority claimed from DE102019207967A1).

2.1 Preliminary studies: Introduction of the induction air heater concept and definition of technical requirements

2.1.1 Technical requirements

According to the multi-scale approach introduced in Section 1.3, the initial step defines the technical requirements for selecting the EFH concept solution while providing further insights into the multi-scale investigations. The definition of the technical requirements is based on the outcomes from idealized simulation studies at the macro scale for the Brayton CB [35] and A-CAES [33]. Both studies have shown that elevating the maximum system temperature through integrating additional PtH within the heat pump cycle increases the energy density of the system and reduces the required component size, offering the potential for cost reduction. To this end, three key technical requirements for the EFH were identified, as presented in Figure 2.2:

1. High outlet temperature $T_{\mathrm{EFH,out}} > 550$ °C
2. Maximum volumetric power density p_{vol}
3. Maximum power-to-heat conversion efficiency η_{PtH}

The system requires high temperatures beyond the feasible outlet temperature of the heat pump compressor to achieve a maximum energy density for a compact storage system. Benato [35] proposed 550 °C for this compressor limitation to avoid high R&D efforts with associated high equipment costs. The heat pump compressor is the most expensive Brayton CB component. Hence, limiting its temperature capability is a reasonable way to effectively minimize system costs. Consequently, the EFH outlet temperature must exceed 550 °C.

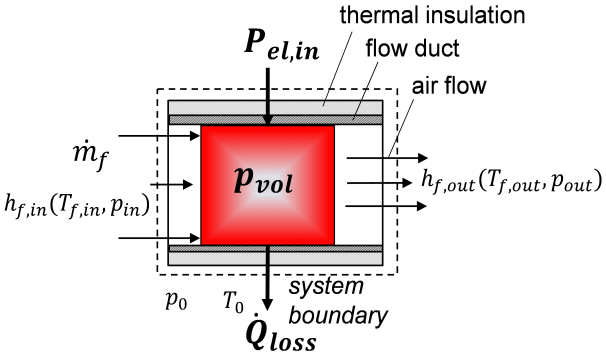

Fig. 2.2 General conceptual configuration and heat balance of the EFH component.

It is crucial to maximize the volumetric power density p_{vol} of the EFH to minimize the equipment cost of the additional EFH component while ensuring a high cost efficiency for the Brayton CB system. The definition of this parameter is based on Joule heating, also known as resistive or ohmic heating, directly related to Ohm's Law, representing the electric power fully converted into heat per unit volume of the electrically conducting body. The volumetric power density p_{vol} is expressed using Joule's first law in differential form with the electrical conductivity σ and the electric field strength E.

$$p_{\mathrm{vol}} = \frac{dP_{\mathrm{el}}}{dV} = \sigma E^2 \tag{2.1}$$

For an efficient generation of high-temperature heat by the EFH and to ensure a high RTE for the Brayton CB system, the EFH component should have the maximum possible PtH efficiency η_{PtH}, defined as the

ratio of delivered high temperature heat $\dot{Q}_{\mathrm{th,out}}$ to the supplied electric power $P_{\mathrm{el,in}}$:

$$\eta_{\mathrm{PtH}} = \frac{\dot{Q}_{\mathrm{th,out}}}{P_{\mathrm{el,in}}} = \frac{\dot{m}_{\mathrm{f,air}} \cdot (h_{\mathrm{f,out}} - h_{\mathrm{f,in}})}{P_{\mathrm{el,in}}} \tag{2.2}$$

where $\dot{m}_{\mathrm{f,air}}$ represents the mass flow rate of the WF (here: air), and h gives the enthalpy obtained at the heater inlet and outlet, a function of temperature and pressure.

2.1.2 Induction air heater concept

Two PtH technologies stand out for utilization in EFH to meet the introduced requirements: resistive and inductive heating. Both technologies operate on the principle of Joule heating and have been established for decades in various heat treatment applications since they effectively provide high-temperature process heat [37] with a high power density. Commercially-available utility-scale EFHs currently use resistive heating elements; however, they have limitations, restricting outlet temperatures to 600–700 °C due to the constrained heat transfer area of the employed tubular metallic heating elements [38, 39].

Induction heating is the process of heating an electrically conductive material by generating an alternating magnetic field with an induction coil based on electromagnetic induction to induce eddy currents into the heating material by interacting with the alternating magnetic field. The induced eddy currents generate heat based on the principle of Joule's first law, as expressed by Eq. (2.1), inside the heating material. Therefore, it can provide high-temperature, efficient, and versatile heat for various industrial applications, including soldering, surface hardening, brazing, heat treatment, and metal melting [40, 41].

2.1 Preliminary studies: Introduction of the induction air heater concept and definition of technical requirements

Previous conceptual studies on induction heating for air heating purposes have revealed significant potential for tubular heating elements [42, 43] and for the packed bed configuration [44, 45], illustrated in Figure 2.3. Compared to tubular heating elements, the pebble bed configuration offers a 50% larger specific heat transfer area and enables turbulent fluid flow, resulting in more efficient convective heat transfer to the air. Moreover, the contactless electric power transmission enables high and uniformly distributed heat generation inside the granular bed as each sphere induces similar eddy currents. This beneficial characteristic ensures a homogeneous heat generation without the limitations imposed by electrical contacts. With these conceptual advantages, the efficient generation and transfer of high-temperature heat can be achieved, enabling gas outlet temperatures above 1000 °C. Hence, the EFH concept has been selected to generate and transfer high-temperature heat for the Brayton CB application.

Figure 2.3 presents a schematic arrangement and the experimental setup of the conceptual configuration comprising an insulated pebble bed inside the induction heating coil. The insulation has a dual purpose. Firstly, it prevents a direct short-circuit between the induction coil and the pebble bed, while secondly, it minimizes heat losses from the hot bed to the ambient, aided by the presence of the insulated Al_2O_3 ceramic tube.

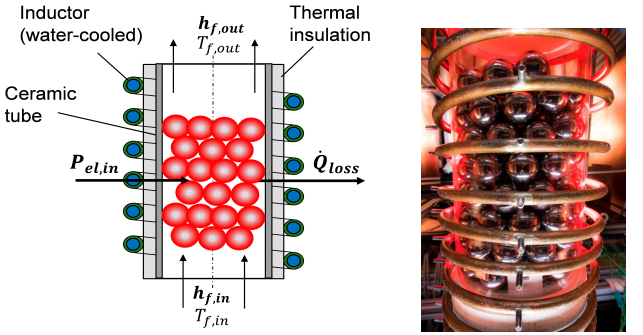

Fig. 2.3 Conceptual arrangement (left) and experimental setup (right) of the inductively heated pebble bed concept.

Overall, induction heating of a pebble bed can provide a high-temperature and energy-efficient heat source with a high power density. However, further research is needed to fully understand the electrothermal process and prove this EFH concept's application in a Brayton CB. The following contribution addresses these challenges and presents a suitable material solution specifically identified for high-temperature applications to advance this EFH concept's applicability in a Brayton CB.

2.2 Paper I (micro scale): Material identification, numerical modeling, experimental validation, and proof-of-concept

Sergej Belik, Omar Khater and Stefan Zunft

The following research paper was published in
Applied Sciences
Volume 13, No. 4, February 2023, 13042311
https://doi.org/10.1016/j.est.2022.104570

Contribution roles
Sergej Belik:
Research work - Conceptualization, methodology and model development, software, investigation and validation, formal analysis and data curation
Writing - Conceptualization, original draft preparation, reviewing, editing and visualization

Omar Khater:
Research work - Software and modeling, experimental investigation
Writing - Reviewing and editing

Stefan Zunft:
Reviewing, editing and supervision

applied sciences

MDPI

Article

Induction Heating of a Fluidized Pebble Bed: Numerical and Experimental Analysis

Sergej Belik *, Omar Khater and Stefan Zunft

Institute of Engineering Thermodynamics, German Aerospace Center (DLR), 70569 Stuttgart, Germany; okhater@student.ethz.ch (O.K.); stefan.zunft@dlr.de (S.Z.)
* Correspondence: sergej.belik@dlr.de

Abstract: The development of energy-efficient Power-to-Heat (PtH) technologies with high power density on a utility scale is a key element in the future of flexible energy systems. Although existing solutions for electric flow heaters (EFH) based on resistance heating have a high efficiency, the process outlet temperature and power output are limited by the lifetime of the contact heating elements. Inductively heated packed bed heaters can achieve higher gas outlet temperatures with a higher power density, which is essential for an efficient process. This paper focuses on the modeling, experimental validation and numerical analysis of inductively heated pebble bed gas heater. Foremost, a model that is based on a 3D finite volume method approach is introduced. After that, an experimental setup for different sphere arrangements is used to obtain results for concept verification and model validation. With the model validated, the design space for the PtH concept is investigated by varying the heat transfer area and material properties of the pebble bed. Design solutions with high energy efficiency above 90% and power density over 5.5 MW/m^3 are presented for magnetic as well as non-magnetic materials at laboratory and utility scale.

Keywords: power-to-heat; electric flow heater; induction gas heater; packed bed; numerical analysis

Citation: Belik, S.; Khater, O.; Zunft, S. Induction Heating of a Fluidized Pebble Bed: Numerical and Experimental Analysis. *Appl. Sci.* **2023**, *13*, 2311. https://doi.org/10.3390/app13042311

Academic Editor(s):

Received: 4 December 2022
Revised: 2 February 2023
Accepted: 2 February 2023
Published: date: 10 February 2023

1. Introduction

The development of Power-to-Heat (PtH) technologies with high power density and high efficiency on a utility scale is a key element for coupling the electricity and the heat sector [1,2]. There are currently two candidates for PtH technologies worth considering for the electric flow heater (EFH) with high power density, efficiency and temperature: resistance heating and induction heating. Both technologies are widely used for high-temperature industrial material treatment (hardening, forging and melting of metal) [3–5], where megawatt scale process heat is required. For the industrial application of the EFH, however, resistance heating has become generally established, as this technology has lower capital costs and higher efficiency compared to the induction heating technology [3].

1.1. Applications of Electric Flow Heaters

Various electric flow heaters are used industrially at different power levels. On a megawatt scale, the most common type is the flanged immersion heater. This configuration offers a large heat transfer area and is mostly used in plant engineering for drying and air-conditioning with gaseous media [6]. To this end, the gaseous heat transfer fluid (HTF), which is typically air, flows in direct contact along the tubular heating elements providing high-temperature process heat. The heating element usually consists of a Ni-Cr resistance wire, which is embedded in a MgO metallic jacket tube. Low cost solutions for resistance wires reach operating temperatures up to 1200 °C [6]. However, the MgO layer limits the heat transfer to the jacket tube. As a result, the maximum achievable gas

temperatures are in the range of 600–700 °C [6,7]. Despite the large heating area, the poor heat transfer properties of the HTF and the limited jacket temperatures limit the heating application to temperatures lower than 700 °C on a utility scale.

EFH based on induction heating has the potential to achieve process temperatures above 700 °C for industrial scale applications due to the typically high induced power rating of more than 1 MW_{el} per m^2 [8]. However, its equipment costs cannot compete with the costs of fossil gas fired heater systems. Therefore, for high process temperatures above 700 °C, natural gas heaters are preferred.

Additionally, the induction fluid heater can be used for power plant applications in so called Carnot batteries (CB). In these batteries, electric power is converted to high-temperature (HT) heat that is first stored in a thermal energy storage (TES) system and then converted back to electricity in a thermal power cycle as needed. The EFH is mostly integrated into the charging cycle of the CB to raise the maximum temperature and hence the energy density of the system [9]. As a result, component size and thus the equipment cost are reduced [10].

A promising application of EFHs is the Brayton battery [10–12], which is a subcategory of CBs. In a Brayton battery, the HT heat from the EFH is stored in a sensible TES while charging and converted back to electricity using the Brayton gas turbine cycle while discharging. The EFH is integrated into the charging heat pump cycle downstream of the air compressor to increase the inlet temperature of the sensible TES up to 1050 °C [10] and beyond [12]. Benato [10] first showed that additional HT heat from EFHs increases the energy density of the system by 105% and reduces its costs by 35%. However, the author omitted details of PtH technology and of the EFH concept that enables such high process temperatures to be achieved. In addition to Benato's work, Belik [12] presented an increase in energy density of 70% accompanied by a cost reduction of 23% applying a 17 MW EFH component. To fill the research gap of the missing EFH solution, the author proposed an induction air heater comprising an inductively heated pebble bed (PB) to generate HT process heat with a conversion efficiency of 85% and at temperatures above 1000 °C. The purpose of this work is to verify this PtH concept for the application in a Brayton battery and to provide a validated design tool along with suitable materials for energy-efficient HT operation.

1.2. Conceptual Arrangement of the Induction Gas Hater

The concept of such an inductively heated pebble bed (PB) gas heater is illustrated in Figure 1. It comprises a PB located inside of an insulated induction heating coil. On the one hand, the insulation and the ceramic tube prevent a direct short circuit between the induction coil and the PB. On the other hand, they minimize the heat loss from the hot packed bed to the ambient. In addition to this loss, Figure 1 shows ohmic losses of the induction coil, which are removed as waste heat by the water-cooling system. Furthermore, the illustrated heat balance indicates the volumetric heat $\dot{q}_{ind}$ induced inside the PB which is further transferred as HT heat $\dot{Q}_{th}$ to the upflowing air stream. This PtH concept enables a high and uniformly distributed power density within the granular bed, as eddy currents are induced in each sphere and heat them up according to the Joule effect. In addition, the packed bed provides a high specific heat transfer area that is often accompanied with a turbulent fluid flow which leads to an efficient heat transfer to the air flow. Both these conceptual advantages allow the efficient generation and transport of HT heat to achieve gas outlet temperatures up to 1050 °C [10] required for an application of the induction gas heater concept in a Brayton battery.

Few authors have studied induction heating concepts for heating applications with different HTFs. Curran et al. [8] were the first to present a tubular PtH concept of an induction heater to heat an oil flow. The laboratory setup uses a mild steel tube that is shrunk on to a stainless liner to heat the oil stream by 30 °C to temperatures far below 70 °C. The tubular concept achieves a process efficiency above 80% with an input power of 888 W. Another tubular concept in a similar power range was proposed by Unver et al.

[13] to heat up an air flow to 50–60 °C for the purpose of drying fruits and vegetables. The authors studied two induction air heater prototypes These prototypes respectively achieved efficiencies of 77% and 87%, using insulated carbon steel tubes. In addition, the authors observed the significant influence of the flow rate on efficiency, which increases by approximately 17% for a doubling in the flow rate. In another work, Unver [14] modified the tubular concept using five additional carbon steel disks, which are arranged perpendicular to the air flow. This measure resulted in a decline in efficiency from 29% to 16% due to the presence of the disks. Unver's tubular heater concepts aim to generate heat far below the Curie point of steel (768 °C) where carbon steel tubes with a small specific heat transfer area are sufficient to ensure high efficiency. The application in a Brayton battery, however, requires outlet temperatures far above the Curie point of steel, where a large specific heat transfer area is required to ensure a small temperature difference between solid and fluid.

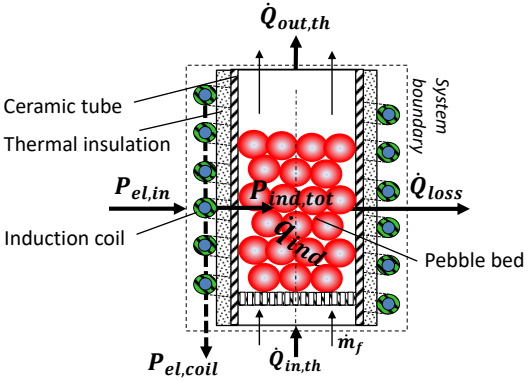

Figure 1. Conceptual arrangement under investigation and heat balance of the inductively heated pebble bed concept.

In contrast to the tubular concepts, the inductively heated PB concept from Figure 1 offers a significantly higher specific heat transfer area. Therefore, various scientific studies used the inductively heated PB as a volumetric heat source to predict heat transfer rates for various HTFs [15–18]. Baumeister et al. [15] and Eichorn et al. [16] reported linear temperature distribution for packed beds with induction heating. Xu et al. [17] used induction heating to study flow boiling heat transfer effects of inductively heated packed bed. Leininger et al. [18] used an induction heating coil to generate heat inside the spheres in an effort to simulate conditions which are present in a fluidized nuclear reactor. However, these studies determined the electrically generated heat inside the randomly-packed bed exclusively through experiments either by means of an oscilloscope measurement at coil terminals or by the measurement from the power converter. In contrast, Duquenne et al. [19,20] introduced a simplified modeling approach for the calculation of the electrically generated heat using the analogy between a regular pile of spheres and a cylinder. The authors used the electromagnetic solution applied in [21] for the cylinder in an alternating magnet field to calculate the heat generation of a rod bundle. This solution corresponds to that of the well-ordered PB if the electrical resistance and the mass of both systems are equivalent [20]. Although this modeling approach gives an accurate and time-efficient prediction of the equivalent bed resistance, it is only valid for particle diameters below 5 mm [20]. Altogether, with the exception of reference [20], all of the mentioned works determined the induced heat source inside the PB by means of electrical measurements.

1.3. Contributions

Although many induction heating studies have been conducted, whether for drying with air using the tubular heater concept or for heat transfer studies using the packed bed, the concept of the inductively heated PB for heating air to temperatures above the Curie point of steel has not been addressed. Moreover, the heat generation and heat transfer through the packed bed has been determined only experimentally. However, the prediction of the power density and process efficiency requires detailed modeling of the PtH process. Therefore, the objective of this paper is to present a model which calculates the induced heat sources and the temperature distribution resulting from the induction heating of a fluidized monodisperse PB.

This paper contributes to the field of high-temperature (HT) PtH solutions. We propose and investigate a novel PtH concept that has the potential to generate and to transfer HT heat to the HTF under conditions beyond the Curie point of steel. To this end, this work addresses the modeling, concept verification, experimental model validation, and finally the numerical analysis of the inductively heated pebble bed PtH concept. Foremost, we introduce a model that is based on a 3D finite volume method. For the verification of the novel PtH concept and for model validation we use a HT resistant experimental setup consisting of various PB arrangements. The experimental study presented shows an overall high process efficiency and high power density for fully packed bed arrangements even at high temperatures. The conducted numerical studies support these findings and provide recommendations for energy-efficient design solutions with maximum power density on both laboratory and utility scale. Finally, this study identifies suitable material solutions for an energy-efficient HT operation in a Brayton battery.

2. Numerical Model

The objective of the numerical model is to provide an approximation for the spatial distribution of induced heat sources inside the pebble bed (PB) and for the convective heat transport to the gaseous HTF for different particle sizes and arrangements.

2.1. Particle Model: Electromagnetic Field Solution

The electromagnetic analysis is described by Maxwell's equations evaluated in a frequency domain. We examine the case of a single sphere plunged into a given uniform harmonic magnetic field $\boldsymbol{B}$ oriented parallel to the inductor axis, adopting spherical coordinates (r, φ, θ), neglecting displacement currents [3] and assuming linear constitutive relations. Maxwell's equations are thus written as

$$rot\, \boldsymbol{H} = \sigma \boldsymbol{E} \qquad \text{with } div\, \boldsymbol{B} = 0 \tag{1}$$

$$rot\, \boldsymbol{E} = -j\omega\mu\mu_0 \boldsymbol{H} \text{ with } lapl\, \boldsymbol{E} = 0 \tag{2}$$

The solution is analogous to Lupi's [3] and Poritsky's approach [22] with the implementation of Bessel functions to Equation (2), assuming that the amplitude of the field strength H_0 outside the sphere is deduced from the inductor length l_i, its windings N_i, the current I_i and the applied factor 0.4π [22]

$$H_0 = \frac{I_i\, N_i\, 0.4\pi}{l_i\, K_i} \tag{3}$$

considering Nagaoka's correction factor for inductors with finite length-to-diameter ratio [23].

$$K_i = 1 + 0.44\, d_i/l_i \tag{4}$$

The electric field $\boldsymbol{E}$ is then calculated in circumferential direction using the unit vector $\boldsymbol{i_\varphi}$ from Equation (5) inside the sphere

$$\boldsymbol{E_\varphi} = -C \sin\theta\, r\, (\psi + 1)\boldsymbol{i_\varphi} \tag{5}$$

where C is a constant finally given by Equation (11), which has to be determined by the initial and boundary conditions. In this case, the boundary conditions are specified as continuous tangential components of $\boldsymbol{H}$ and $\boldsymbol{E}$ at the boundary of the sphere. This returns a value for ψ as a function of the sphere radius r and of the damping coefficient k from Equation (9)

$$\psi = \frac{(2\mu-1)-F(k\cdot r)}{(\mu+1)+F(k\cdot r)} \quad \forall\, \psi \in \mathbb{C} \tag{6}$$

with μ being the relative magnetic permeability and $F(k\cdot r)$ given by the function

$$F(k\cdot r) = \frac{k\cdot r\, S_1^{'}(k\cdot r)}{S_1(k\cdot r)} \tag{7}$$

The function $S_1(k\cdot r)$ is related to the J Bessel function using the following equation

$$S_1(k\cdot r) = r^{-1/2} J_{1.5}(k\cdot r) \tag{8}$$

The constant k is the damping coefficient of the electromagnetic wave [3], which describes the skin effect in an electrically conducting body:

$$k = \delta^{-1} + j\delta^{-1} \tag{9}$$

According to this effect, the current density decreases from the surface of the sphere toward its center. Consequently, the induced power is concentrated in the surface layer which is called the skin depth and calculated by Equation (10)

$$\delta = \sqrt{\frac{1}{\pi\, f\, \sigma\, \mu\, \mu_0}} \tag{10}$$

with f being the frequency and σ the electrical conductivity.

For a harmonic field solution with a uniform magnetic field, the value of the integration constant C is given in SI-units as

$$C = j\pi f \mu_0 H_o \tag{11}$$

with the magnetic field constant $\mu_0 = 4\pi 10^{-7} \frac{N}{A^2}$.

Since the distribution of the electric field in circumferential direction $\boldsymbol{E_\varphi}$ is determined inside the sphere, one can calculate energy dissipation per unit volume by the Joule effect:

$$p_{ind} = \frac{1}{2}\sigma \left\| \boldsymbol{E_\varphi^2} \right\| \tag{12}$$

As a result, the total electric power generated inside n spheres is calculated by integrating over the sphere volume:

$$P_{ind,tot} = \sum\nolimits_{i=1}^{n} \int_V p_{ind}\, dV \tag{13}$$

Equation (13) reflects the core assumption of this model, which was also employed by Duquenne et al. [12]. It indicates that each sphere is electrically insulated from other spheres. In addition, the bulk of power induced inside a sphere comes only from the interaction with the external magnetic field and not from neighboring spheres. Therefore, each sphere is treated as electromagnetically independent.

2.2. Two-Phase Electrothermal Model: Coupled Electromagnetic and Thermal Analysis

The prediction of the induced heat sources and of the resulting temperature field requires a multi-physical and iterative process simulation. Figure 2 illustrates the first step of the geometry modeling of the monodispersed packed bed that is further divided into several subdomains for meshing. The specified subdomains are presented together with the mesh in the following Section using Figure 3 and Figure 4. Finally, the coupled electromagnetic and thermal solution procedure is introduced in Section 2.2.2.

2.2.1. Geometry Modeling and Meshing

DEM software [24] was used to obtain the arrangement of the particles in the randomly-packed monodispersed bed. Table 1 summarizes the input parameters for the DEM calculations. In this simulation, the particles randomly fall under the action of gravity from the upper inlet to the grating of the heating zone, as illustrated in Figure 2. Each particle position was determined for every time step (5×10^{-7} s) using linear spring models. Specifically, the hysteretic linear spring model and linear spring coulomb limit model were applied to model the normal force and the tangential force, respectively [24]. In addition, the linear spring rolling limit is used as rolling resistance model neglecting adhesive force. This simulation procedure ends after reaching convergence at 1×10^{-9} Joule for the pebble bed's kinetic energy. The obtained sphere center coordinates O_{center} were then extracted and passed to the ANSYS SpaceClaim geometry modeler to first generate the geometry using a custom script. The geometry was then transferred to the FLUENT solver for thermal initialization and further simulation work, as shown in Figure 5.

Table 1. Input parameter used for the DEM model.

Parameter	Magnitude
particle diameter d	case 1: 30 mm; case 2: 25 mm; case 3: 20 mm
particle number n	case 1: 61; case 2: 91; case 3: 160
time step t	5×10^{-7} s
Young modulus	210×10^{9} Pa
Poisson's ratio	0.30
restitution coefficient	0.20

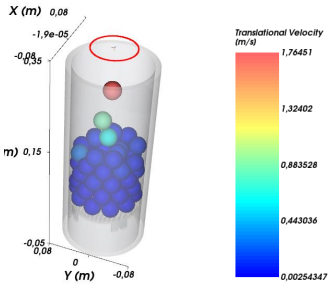

Figure 2. Simulation procedure of the filling process with d = 30 mm spherical particles into the Al_2O_3 container using Rocky multibody DEM software [24].

The resulting three-dimensional domain comprised of cylindrical and spherical subdomains. The hollow cylindrical subdomains represent the insulation and the outer ceramic tube whereas the spherical subdomains represent the solid spheres as shown in Figure 3. The application of Equations (5)–(12) for the spherical subdomain removes the

need to model the induction coil thus eliminates the computations associated with the solution of the Maxwell Equations (1) and (2) over the entire simulation domain.

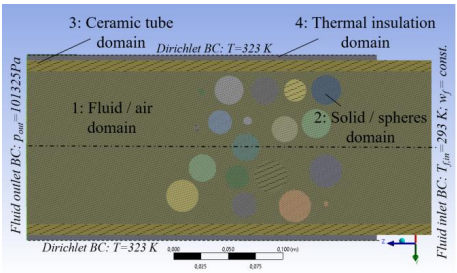

Figure 3. Cross-section of the computational domain for case 1: pebble bed with d = 30 mm; subdomains: 1-fluid; 2-solid; 3-tube; 4-insulation.

The induced heat sources in each sphere (Joule effect) was calculated using Equation (12) as the volumetric power input to each cell inside every spherical subdomain. The calculation of induced volumetric power input was based on the coordinates of every cell centroid in the mesh. Thus, the accuracy of the solution for Equation (12) and for the total electric power input by using the volume integral from Equation (13) depends on the mesh resolution. Therefore, a grid refinement study was conducted on the one hand to ensure a convergence of the solution for the induced power and on the other hand to obtain a minimum number of mesh elements necessary for a time-efficient and accurate solution process. The results from the grid refinement study, presented in Appendix A, show convergence attained for more than 55 Mio. elements. We applied 57 Mio. mesh elements using 30 inflation layers for time-efficient numerical calculation process of the simulation study from Section 4.2.

The results for the grid study further indicate that to obtain a sufficiently accurate solution for the distribution of heat sources in the surface layer, the numerical mesh size needs to be at a significantly smaller order of magnitude than the penetration depth δ in both the radial and latitudinal directions. Therefore, 15 layers starting from a height of 10^{-5} m were used in the surface region of each sphere. In a similar fashion, the same number of layers was added to the sphere walls to account for the boundary layers of the HTF flow. These inflation layers are shown on the mesh in Figure 4. Outside of these layered regions, the mesh is unstructured. Near the spheres, the unstructured mesh is refined to accurately resolve volumes in between spheres.

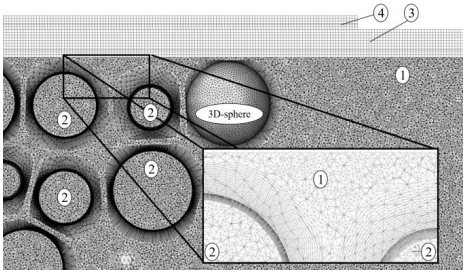

Figure 4. Cross-section of case 1 mesh (d = 30 mm) with 15 layers for the sphere subdomain and for its boundary layer inside the fluid subdomain.

2.2.2. Coupled Electromagnetic and Thermal Solution

The solution for electromagnetic field was calculated based on the harmonic analysis described by Equations (5)–(12) and coupled with the temperature field solution according to Figure 5. The solution for the temperature field of the solid and fluid phase was obtained numerically using a commercially available fluid dynamics package FLUENT 21.1. The calculation for the solid phase relies on steady state condition of the heat Equation (14) formulated in spherical coordinate system and extended by the source term from Equation (12). This expression was implemented into the solving process as a custom volumetric heat source using a user defined function. The volumetric power density p_{ind} is fully converted into heat and replaces the right-hand side of Equation (14) as the Joule heat volumetric power density $\dot{q}_{ind}$:

$$\frac{1}{r^2}\frac{\partial}{\partial r}\left(\lambda_s r^2 \frac{\partial T_s}{\partial r}\right) + \frac{1}{r^2 \sin^2\theta}\frac{\partial}{\partial \varphi}\left(\lambda_s \frac{\partial T_s}{\partial \varphi}\right) + \frac{1}{r^2 \sin\theta}\frac{\partial}{\partial \theta}\left(\sin\theta\, \lambda_s \frac{\partial T_s}{\partial \theta}\right) = p_{ind} = \dot{q}_{ind} \quad (14)$$

The fluid phase is calculated by solving the steady state incompressible Navier Stokes Equations using a pressure-based solver. Turbulence is modeled using the κ-ω-turbulence model. Gravity effects are disregarded for the fluid phase, since the conceptual investigation is carried out using air flow with high Reynolds numbers. Thermal properties for dry air are taken from the FLUENT material database considering a temperature dependence for the specific heat capacity and for the density. But constant values for viscosity (1.7894×10^{-5} kg m^{-1} s^{-1}) and thermal conductivity (0.0242 W m^{-1} K^{-1}) are applied. In addition, radiation is neglected since the investigation is conducted at temperatures significantly below the Curie point of carbon steel (768 °C).

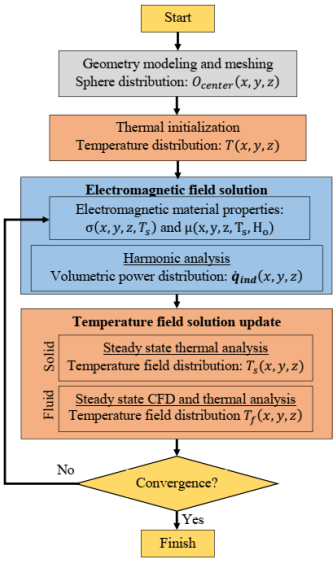

Figure 5. Coupled electromagnetic and thermal analysis with feedback of the temperature field for update of electromagnetic material properties.

To obtain sufficiently accurate simulation results, temperature dependences of the solid material are incorporated into the electromagnetic solver. The temperature dependency of the electrical conductivity σ and the magnetic permeability μ were considered via empirical models obtained from [3] and [25]. In addition, magnetic field dependence of μ was considered based on the external field H_o [5]. Finally, the total induced power density given by Equation (13) and the averaged fluid outlet temperature were set as convergence criteria for the solution process. Thus, the simulation finishes after reaching convergence at 10^{-5}.

The boundary conditions (BCs) are illustrated in Figure 3. The BC for the inlet is an isothermal mass flow at a constant ambient temperature of 293 K. The wall temperature of the outer domain wall directly borders the water-cooled induction coil. Therefore, the wall temperature is set to be isothermal at the 323 K as measured in the setup from Figure 6. Finally, the outlet boundary condition is a simple pressure outflow.

3. Experimental Setup

The objective of the experimental study is on the one hand to verify the performance of the proposed PtH concept for the application in a Brayton battery. On the other hand, to provide the data for the validation of the introduced electrothermal model. The concept verification, model validation and investigation is accompanied with numerical parameter studies presented in Chapter 4.

A testing facility was designed and setup to investigate the PtH concept of inductively heated packed bed in a vertical fluidized column. The experimental test rig consists of a middle-frequency converter, a transformer, an induction heating coil and a flow system for circulating air through the test section. A schematic of the testing facility and the measuring points is shown in Figure 7. The test section assembly is depicted in Figure 6.

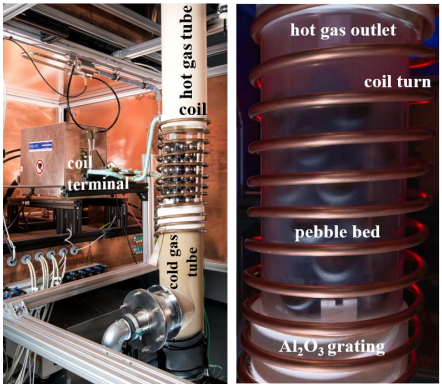

Figure 6. Experimental setup without exterior insulation layers and a glass tube instead of used Al_2O_3 ceramic tube between induction coil and pebble bed.

The experiment makes contradictory demands on the materials to prevent parasitic heating of the surrounding components. Therefore, only ceramic insulators made of Al_2O_3 were used inside and outside the test section, see Figure 6. Only the spheres in the test section were made of electrically conductive material to promote heating. Different configurations of sphere diameter and total number of spheres were tested in this setup. The geometries and materials used for individual components of the test section are summa-

rized in Table 2. To prevent an electric current between spheres and to address the assumption made for Equation (13), the spheres were additionally coated in an electrically insulating and HT resistant coating.

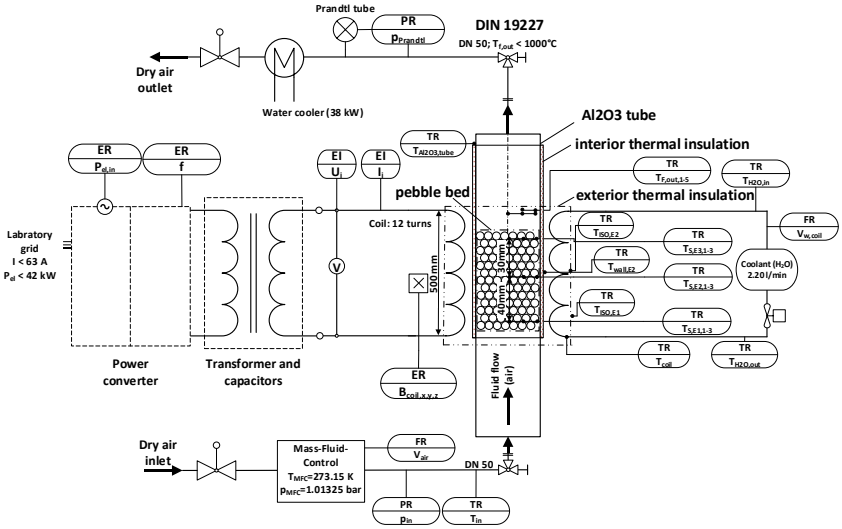

Figure 7. P&ID flow chart for the experimental test rig based on DIN 19277.

Table 2. Geometries and materials used for components of the test section.

Parameter	Inductor	Insulation	Ceramic tube	Pebble bed
height [m]	0.50	0.60	0.470	0.07–0.10
outer / inner diameter [m]	0.190 / 0.170	0.170 / 0.160	0.160 / 0.136	d = 0.02 / 0.025 /0.03 spheres
thickness [m]	0.010	0.005	0.012	≙ outer diam.
number [-]	12 turns	2 layers	1 piece	160 / 91 / 61pc.
heat transfer area [m^2]	-	0.32	0.20	0.201 / 0.1787 / 0.1725
material	Cu: 80% IACS	Al. silica felt 140Z [26]	Al_2O_3 C799 [27]	UNS G10060 [25,28,29]

This experiment is subject to losses which can be categorized into leakage losses, thermal losses, and electrical losses. To minimize leakage, a HT gasket [30] was used to fill in axial gaps in the construction. Additionally, the facility was designed to benefit from additional sealing pressure when heated through thermal expansion of the mid-section in the vertical direction.

Thermal losses were minimized by adding two layers of insulation material [26] between the tube walls and the coil as well as between the coil and the environment. Moreover, the temperature increase of the cooling water inside the inductor coil was measured with thermocouples at the inlet and outlet.

Finally, the power loss to the coil was evaluated via direct voltage and current measurement at the coil terminals shown in Figure 6. The frequency was returned by the power converter, which is an input parameter for the electromagnetic simulation.

Five thermocouples were installed at the outlet of the test section. All the other thermocouples inside the packed bed structure were located according to Figure 7. These were spread out in the radial and vertical directions to capture the distribution of temperature as it varies in the pebble bed. Furthermore, three thermocouples were placed at the outer wall of the facility to determine heat loss to the environment.

This measurement is introduced in Table 3, where uncertainties of the measuring instruments are additionally reported. The highest measurement uncertainties were caused by the current measurement of the Rogowski coil (±2.5%) and from the power measurement at the converter (±2.0%). The output error for the measured key performance indicators (KPIs) in Figures 8 and 9 was estimated using the common Gaussian error propagation method.

Table 3. Measurement devices used for the laboratory setup from Figure 7.

Sensor	Measurement	Range	Accuracy
Pt 100 class.1/3 B4 ladder	Temperature of cooling water	−50... +300 °C	±0.27 °C for 0–100 °C
Thermocouple type K, class.1	Temperature Solid	−40...+1000 °C	±1.5 °C or 0.4% m. v..
Multipoint Thermocouple type K, Class 1 Ø0,5 *mm*	Temperature air	−40...+1000 °C	±1.5 °C or 0.4% m. v.
Flow sensor IFM SM6050	Volume flow rate for water	0–25 l/min.	± (0.8% m. v. +0.5% m. e. v.)
Oscilloscope RTH1004	Voltage U_i and Current output	0…300 V, f ≤ 60 MHz	
Rogowski coil MA200 Miniflex	Current I_i	± 2.0% (f ≤ 1 MHz)	± (2.5% m. v. +0.7 A)
MF converter	Power input and frequency	0.5–40 kW	±2.0%
BronkhorstF-206BI-PGF-99-V	Volume flow rate for air $\dot{V}$	0–350 Nm^3/h	±0.5% m. v. +0.1%
Pitot Tube	Flow velocity	0–10 m/s	±3.0% reading

4. Results and Discussion

In the following sections, experimental and simulation studies based on the laboratory setup and the model from Chapter 2 are conducted. The following both sections present the obtained experimental data and compare those with simulation results for validation purpose. Using the validated model, three parameter studies are conducted investigating key performance indicators (KPIs) of the PtH concept which are the volumetric power density, the heat flux density and the PtH efficiency. In the first study, geometry parameters are varied for the used carbon steel to identify energy-efficient designs with high power density in laboratory scale. The second study discusses the introduced KPIs using dimensionless parameters independently from the setup. This discussion reveals maxima for energy efficiency and power density. The final study aims at the identification of HT resistant and efficient materials for the application in Brayton battery below and far beyond the Curie point of steel.

4.1. Experimental Results for PtH Efficiency and Heat Flux Density

To verify the proposed PtH concept and to provide experimental data for the model validation, the experiments have been conducted with a constant input power of $P_{el,PC} = 5.3\ kW$ at the power converter and an air flow rate that is regulated from $\dot{V}_f = 25\ Nm^3h^{-1}$ to $\dot{V}_f = 150\ Nm^3h^{-1}$ (at reference conditions: $T_N = 273.15\ K$ and $p_N = 101325\ Pa$). A correction factor proposed by Hänchen et al., of 0.85 is used for the flow rate to address the near-wall channeling effect, indicating that 15% of the flow rate does not thermally interact with the pebble bed [31]. In addition, Table 2 gives an overview of the geometry variation and the materials used for the test section.

The experimental investigation and verification of the inductively heated pebble bed concept is conducted at steady state conditions. The concept evaluation focuses on the energetic efficiency η_{PtH} and heat flux density $\dot{q}_{tot}$. The definition of the PtH efficiency is based on First Law considerations taking into account electrical and thermal power input and heat output introduced in Figure 1

$$\eta_{PtH} = \frac{\dot{Q}_{th,out}}{P_{el,PC}\,\eta_{PC}} = \frac{\dot{Q}_{th,out}}{P_{el,in}} = \frac{\dot{m}_f\left(h_{f,out}\left(T_{f,out}\right) - h_{f,in}\left(T_{f,in}\right)\right)}{P_{el,coil} + P_{ind,tot}} \tag{15}$$

where $\dot{m}_f$ is the mass flow rate of the air flow and h_f the temperature dependent enthalpy at the inlet and the outlet of the heater. The electrical power $P_{el,in}$ at the inductor terminals is measured to be approximately constant at 5 kW during all experiments. The heat flux density $\dot{q}_{tot}$ is given in W/cm^2

$$\dot{q}_{tot} = \frac{\dot{Q}_{th,out}}{A_{HTF}} = \frac{\dot{m}_f\left(h_{f,out}\left(T_{f,out}\right) - h_{f,in}\left(T_{f,in}\right)\right)}{n\,\pi\,d^2} \tag{16}$$

which is the thermal output related to the heat transfer area A_{HTF} that is in direct contact to the total number of spheres n.

The Reynolds number $R_e = d\,w_f\nu_f^{-1}$ containing the particle diameter d, flow velocity w_f and kinematic viscosity ν_f is an appropriate parameter since it contains information about the geometry and the flow conditions, which both influence the heater performance. The key performance indicators $\dot{q}_{tot}$ and η_{PtH} presented in Figure 8 increase with growing Reynolds numbers and with larger sphere diameters. The main reason for this increase is the improved convectional heat transfer to the air due to the higher Reynolds and thus higher Nusselt numbers.

The investigation of the particle diameter shows an improvement of heat flux density and PtH efficiency for larger particle diameters. Results for the PtH efficiency from [12] support this finding demonstrating a higher electrical resistance of the pebble bed and thus a higher efficiency for growing particle size (1.8 mm $< d <$ 7.65 mm). Larger spheres have a higher electrical resistance to the induced eddy currents due to the larger circumference of the equator. According to Joule's law, a higher resistance results in a higher electrical power induced inside the sphere. The discussion from Section 4.4 further explains the relationship between particle size and efficiency, accounting for the effects of temperature dependence.

Altogether, the achieved efficiency above 80% at a high heat flux density shows the potential of this PtH concept and proves the applicability for gas heating applications. In particular, high *Re* numbers above 8000 are favorable for the energy-efficient operation of this PtH concept at high power density.

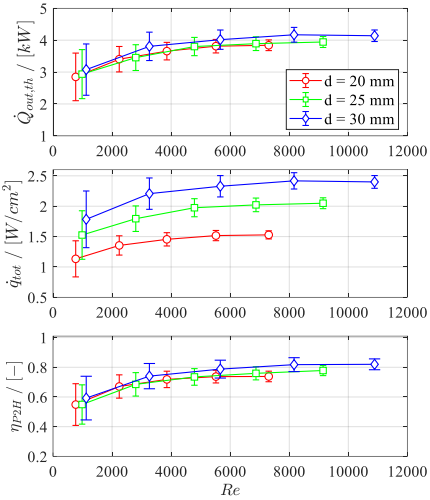

Figure 8. Experimental results for thermal output, the associated heat flux density and the PtH efficiency of the laboratory induction heater at flow rates $\dot{V}_f = 0.85 * [25,56,87,118,150]\ Nm^3h^{-1}$.

4.2. Numerical Results and Validation

For the simulation study, the particle diameter d and the flow velocity w_f were varied analogously to the experimental investigation from previous section. These parameters are summarized in Table 4 together with measured values for frequency f and inductor's peak current I_i. Both values are influenced by the system's inductance that varies with changing packed bed geometry and its temperature dependent material properties σ and μ. Therefore, these electrical inputs were also reported for calculating the electromagnetic field solution.

Table 4. Input parameter for simulation study: frequency and electric current measured at coil terminals for the electromagnetic field solution, and inlet velocity boundary condition for coupled thermal analysis.

	Air Inlet Velocity w_f	**0.62 m/s**	**1.27 m/s**	**1.87 m/s**	**1.46 m/s**	**3.05 m/s**
I_i [A]	d = 20 mm	347.89	328.05	323.14	323.16	311.62
	d = 25 mm	341.54	331.33	331.32	326.21	322.85
	d = 30 mm	341.05	333.98	328.74	327.04	323.53
f [kHz]	d = 20 mm	20.68	21.23	21.36	21.38	21.56
	d = 25 mm	20.84	21.30	21.41	21.57	21.57
	d = 30 mm	21.16	21.65	21.97	22.01	22.10

Figure 9 shows the comparison of simulation and experimental results for the total induced power and the outlet temperature. The curve characteristics of both comparison criteria show a matching progression with respect to the Reynolds number. The characteristic of $P_{ind,tot}$ shows a maximum at moderate *Re* numbers. This maximum is caused by temperature dependent electrical material properties μ and σ, which vary with flow conditions inside the pebble bed. Accordingly, low *Re* numbers result in high solid tem-

peratures near the Curie point at 768 °C and high *Re* numbers lead to an improved convective heat transport along with a decrease in solids temperature to 200 °C. In this temperature range, there is a significant variation in the electrical material properties as illustrated in Figure 10 influencing the heat generation inside the solid. This figure shows a maximum of the function μ/σ, which causes the maximum in the induced power of Figure 9. The discussion in the following section points this effect further out.

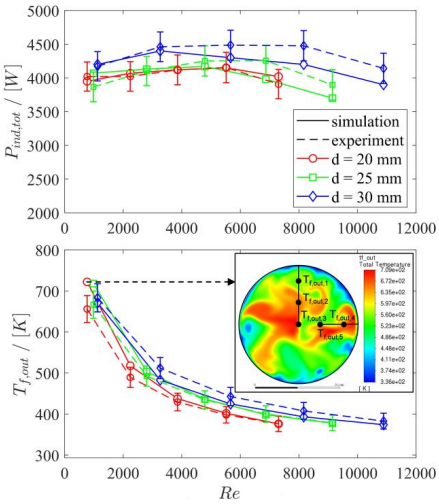

Figure 9. Comparison of simulation and experimental results of the total induced power $P_{ind,tot}$ and the HTF outlet temperature $T_{f,out}$ with one cross-sectional temperature profile solution for d = 30 mm, w_f = 0.62 m/s

The quantitative comparison between experimental and simulation results in Figure 9 shows a good agreement for the induced power $P_{ind,tot}$ of the pebble bed and the resulting averaged outlet temperature $T_{f,out}$. The maximum deviation is below 15% for Reynolds numbers above 2000. For smaller Re numbers, however, the solid temperature approaches the Curie point at $T_C = 768°C$ of the used carbon steel where the magnetic permeability μ changes non-linearly as illustrated in Figure 10. The uncertainty of this $\mu(T_S)$ function is the major reason for resulting deviations in the electromagnetic field solution and consequently in the obtained temperature field solution. Moreover, the assumption of a homogenous external magnetic field as well as negligible radiation effects at high solid temperatures are additional causes for the deviations from the experimental data. Despite these causes and the small dimensions of the test rig, a satisfactory agreement is obtained between the calculated and the measured data, hence the introduced modeling approach can be treated as a solid basis for the following numerical studies.

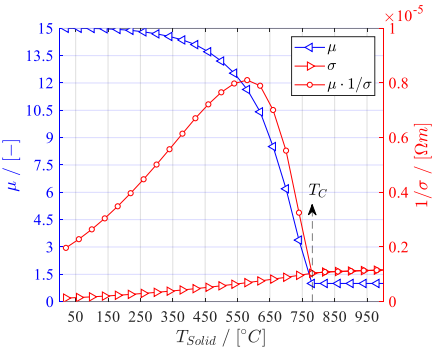

Figure 10. Relative magnetic permeability μ and electrical resistivity $1/\sigma$ as a function of solid temperature T_{Solid} for used steel UNS G10060 [5,25,29].

4.3. Idealized Parameter Study for $\mu(T_S)$

With the validated model, the design space for the inductively heated pebble bed concept can be explored using only the electromagnetic model deduced in Section 2.1 by neglecting thermal losses by convection and radiation (η_{th} = 1). The objective is to identify energy-efficient designs with high volumetric power density for the inductively heated pebble bed concept. In contrast to Section 4.1, this study is idealized, which means that it discusses the maximum achievable heat flux density with the associated PtH efficiency.

The maximum PtH efficiency is obtained when thermal losses to the ambient are neglected and consequently the entire induced heat inside the PB is transferred to the air flow ($\dot{Q}_{th,out} = P_{ind,tot}$):

$$\eta_{PtH,max} = \eta_{ind}\eta_{th,max} = \eta_{ind} = \frac{P_{ind,tot}}{P_{el,coil} + P_{ind,tot}} \tag{17}$$

The formulation for $P_{el,coil}$ is obtained from Kennedy et al. [21]. Under the assumption $\eta_{th,max} = 1$, Equation (16) becomes

$$\dot{q}_{tot,max} = \frac{P_{ind,tot}}{A_{HTF}} \tag{18}$$

Instead of using quantities given in Equation (16), a simple procedure to implement the formulation for $P_{ind,tot}$ has been found without loss of accuracy. This formulation applies scalar quantities for the power density in the bulk $\dot{q}_{ind,PB}$ together with the volume of the pebble bed V_{PB} and is expressed as:

$$P_{ind,tot} = \dot{q}_{ind,PB} V_{PB} \tag{19}$$

The volumetric power density is given using Equations (3) and (6) as:

$$\dot{q}_{ind,PB} = 0.75 H_o^2 \omega \mu_0 F \tag{20}$$

where ω is the angular frequency given by $\omega = 2\pi f$ and F is the power transmission factor characterizing the effectiveness of energy dissipation in the spheres by using the imaginary part of the ψ function from Equation (6):

$$F = -\mathrm{Im}\{\psi\} \tag{21}$$

Finally, the volume of the pebble bed is expressed as:

$$V_{PB} = \frac{\pi}{4} D_{PB}^2 H_{PB} (1 - \varepsilon) \tag{22}$$

using the void fraction ε, the outer diameter D_{PB} and the height of the pebble bed H_{PB}, which are both specified in Table 2. For the void fraction the common value of $\varepsilon = 0.40$ is applied for further calculations.

To investigate the performance of the PtH concept in relation to changing geometry and material properties of the used ferromagnetic steel, the heat transfer area A_{HTF} and the solid temperature T_{Solid} have been chosen as variables for the first parameter study. The heat transfer area $A_{HTF} = n_{max}\,\pi\,d^2$ includes both, the number of spheres and their diameter d as geometric parameters, whereby the maximum number of spheres n_{max} is predetermined to fill the entire bed height H_{PB}. The solid temperature is a suitable variable parameter for the material since both, electrical material properties σ and μ are functions of temperature which have been already shown in Figure 10.

Figure 11 shows results for the PtH efficiency $\eta_{PtH,max}$ and for the power transmission factor F from Equation (21) as functions of bed temperature and HTF area. The temperature dependence of the electrical material properties during heating has a significant influence on the factor F, which expresses the power density given by Equation (20). The power density $\dot{q}_{ind}$, in turn, dictates the PtH efficiency according to Equation (17). This is the reason for the strong relationship between F and $\eta_{PtH,max}$ from Figure 11 for the influencing variables T_{Solid} and d. The influence of the temperature reveals maxima at 580 °C for diameters larger than 10 mm. These maxima are typical for ferromagnetic steel due to opposing temperature curves for σ and μ from Figure 10 where the abrupt drop in magnetic permeability prevails near the Curie temperature. This dominating effect at $T_{Solid} > 580°C$ results in a rapid fall of $F$and consequently of the PtH efficiency. The comparison of the analyzed diameters and HTF areas show lowest efficiencies for particles with $d = 5mm$. The chosen frequency of 22 kHz is insufficient to heat them up efficiently at those small diameters. The highest efficiency results are achieved for 20 mm particles due to highest F values and the high power $P_{ind,tot}$ induced in the large number of spheres.

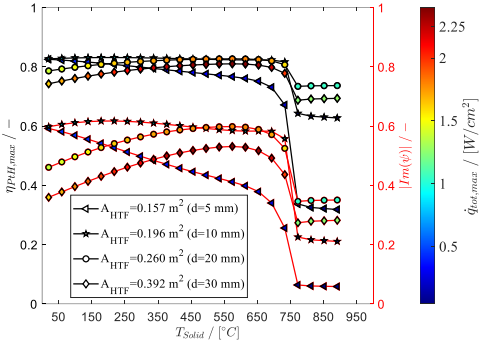

Figure 11. Parameter study results for $H_{PB} = 0.10$, various sphere diameters and temperature dependent material properties for UNS G10060 from Figure 8 at constant electrical inputs: Ii = 333 A and f = 22 kHz.

In contrary to the study from Figure 11, for the analysis in Figure 12 the bed height H_{PB} is varied for constant bed temperature, which is set to 580 °C where previously the highest efficiency is obtained. The PtH efficiency is presented in Figure 12 with respect to HTF area. Moreover, the influence of the ratio between the bed height and the coil length is here presented using the color bar. The PtH efficiency increases for all sphere diameters because the number of spheres increases as well with a higher bed and so does the induced

power according to Equation (13). Therefore, induction heating of a fully packed bed results in maximum efficiency, in particular, when ferromagnetic steel is used at bed temperatures close to 580 °C.

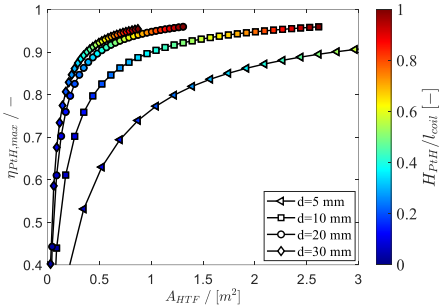

Figure 12. Results for various sphere diameters and bed heights for UNS G10060 at T_S = 580 °C and at const. electrical inputs: I_i = 333 A and f = 22kHz.

4.4. Idealized Parameter Study for $\mu = const$

The next parameter study aims at the identification of optimal design solutions for the PtH efficiency and volumetric power density. In contrast to the previous investigation from Section 4.3, the magnetic permeability μ is independent from bed temperature and is varied from paramagnetic property at $\mu = 1$ to the ferromagnetic property at $\mu = 50$. In addition, the penetration depth δ from Equation (10) is used as variable parameter that imply the frequency and the ideally considered temperature independent material properties σ and μ. This technological parameter is varied from 1 m to 10^{-4} m and is set in relation to the sphere diameter $x_\delta = \delta/d$ to consider on the one hand the varied geometry of the fully packed bed and on the other hand to obtain a dimensionless technological parameter referred to as the relative skin depth x_δ.

In contrast to the results presented in Figure 12, the maximum PtH efficiency and volumetric power density $\dot{q}_{ind,PB}$ from Figure 13 are related to the ratio δ/d for different μ values. For the non-magnetic material with $\mu = 1$ maxima for $\dot{q}_{ind,PB}$ and $\eta_{PtH,max}$ occur at $x_\delta = 0.20$. These both KPIs first increase reaching $x_\delta = 0.20$ due to the pronounced skin effect at low skin depth. After this optimum value, the drop results from the dominating decrease of the material utilization caused by large sphere diameters. This effect has been discussed by many authors for inductively heated cylinders and plates. In contrast to this investigation, they use the reciprocal quantity $m = x_\delta^{-1}$, which is for cylinders at $m_{opt,\mu=1} = 3.5$ [3] and for plates at $m_{opt,\mu=1} = 1.75$ [4]. For a ferromagnetic material with $\mu > 1$ the maxima in Figure 13 increase for both KPIs as they shift from $x_{\delta,opt,\mu=1} = 0.20$ to $x_\delta = 0$. Altogether, the optimal values $x_{\delta,opt}$ are decisive for a high power density and a high efficiency. This means that materials at high-temperature operation beyond their Curie point as well as non-magnetic materials have the potential to achieve high efficiencies by, for instance, adapting the frequency to $x_{\delta,opt}$.

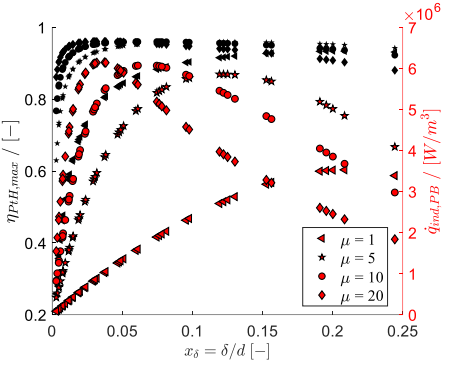

Figure 13. Results for PtH efficiency and volumetric power density with respect to the varied diameter d = [0.005:0.05] m and δ = [1:10⁻⁴] m.

4.5. Identification of Efficient High-Temperature Materials

The final parameter study aims to identify suitable material solutions, which ensure high efficiencies and power densities under high-temperature operation beyond T_C. Such process temperatures are required for industrial high-temperature applications using EFH and for power plant processes with PtH extension. For the second use case, air outlet temperatures up to 1050 °C are needed, for instance, to reduce the capital expenditures of a Brayton battery system [10, 12].

The approach is similar to the one from Section 4.4. The magnetic permeability μ is again independent from bed temperature and is varied from non-magnetic property at $\mu = 1$ to consider the mentioned applications at $T_{solid} > T_C$ to the strong ferromagnetic property at $\mu = 10^2$ for low temperature applications at $T_{solid} < T_C$. In addition, the electrical conductivity, which is temperature independent in this analysis, is varied in a wide range from 10^2 $\Omega^{-1}m^{-1}$ to 10^8 $\Omega^{-1}m^{-1}$ to consider electrical semiconductors and conductors as well. For practical reasons, the frequency is maintained constant throughout the process. For industrial applications the frequency is usually below 10 kHz to minimize ohmic losses in the power converter. Therefore, we assume f =5 kHz and an electrical current of 800 A. Furthermore, geometrical conditions for such an application in the Brayton battery on the megawatt scale are summarized in Table 5.

Table 5. Geometry parameter for application on the megawatt scale.

Parameter	Magnitude
Particle diameter	d = 0.12 m
Number of particles	n = 4688
Outer packed bed diameter	D_{PB} = 1.5 m
Packed bed height	H_{PB} = 4.0 m
Inductor and wire diameter	D_i = 1.875 m; s_i = 2.5 cm
Inductor length	l_i = 5.0 m
Number of inductor turns	N_i = 144

Figure 14 illustrates results for the PtH efficiency as contour lines in relation to both varied material properties where the optimal values for $x_{\delta,opt}$ from Section 4.4 are additionally illustrated. Contour lines for specific PtH efficiency show the optimal range for both material properties in terms of energy efficiency. Hence, to achieve a high efficiency

of $\eta_{PtH,max} > 0.95$ for low temperature applications ($T_{Solid} < T_C$) the magnetic permeability might be in the range $10 < \mu < 100$ for ferromagnetic conductors with an electrical conductivity in the range $2.0 \cdot 10^6 < \sigma < 15.0 \cdot 10^6\ \Omega^{-1}m^{-1}$ for steel. For high-temperature applications at $T_{Solid} > T_C$, this contour plot reveals the required electrical conductivity for non-magnetic materials at $\mu = 1$ in between $40{,}000 < \sigma < 190{,}000\ \Omega^{-1}m^{-1}$. A similar contour plot of the induced volumetric power density from Figure 15 additionally reveals values above 5.5 MW/m³ for $\dot{q}_{ind,PB}$ in a similar σ range at $\mu = 1$. Since the electrical conductivity of steel is normally higher ($\sigma_{CS} > 1.0 \cdot 10^6\ \Omega^{-1}m^{-1}$ for carbon steel), semi-conductive materials are required that are correspondingly high-temperature resistant. Considering these both criteria, electrically conductive ceramics are suitable material options within the identified σ-range. In particular, silicon-infiltrated silicon carbide (SiSiC) has a suitable electrical conductivity between $1000\ \Omega^{-1}m^{-1}$ and $50{,}000\ \Omega^{-1}m^{-1}$ at T_{Solid}=1000 K. Therefore, this carbide ceramic solution is proposed for the application of inductively heated PB gas heater in high-temperature industrial processes and particularly as PtH extension in the Brayton battery.

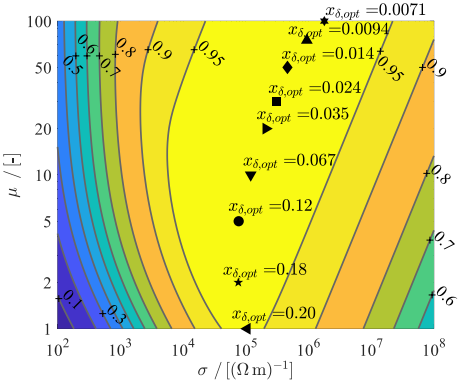

Figure 14. Material properties study: contour lines for PtH efficiency $\eta_{PtH,max}$ using geometrical parameters from Table 5; I_i = 800 A and f = 5 kHz.

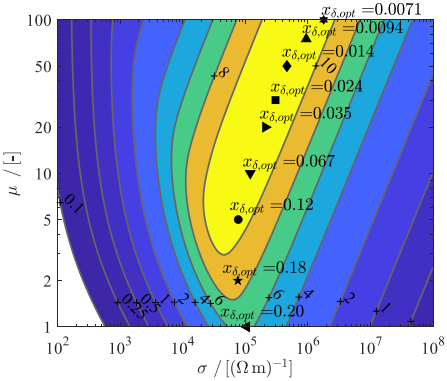

Figure 15. Contour lines for induced power density $\dot{q}_{ind,PB}$ in MW/m³ using parameters from Table 5 at I_i = 800 A and f = 5 kHz.

5. Conclusions

The purpose of this article is to verify a novel Power-to-Heat (PtH) concept for the induction gas heater and to provide a validated design tool along with deduced material solutions for an energy-efficient operation at high temperatures beyond the state of the art solutions with 700 °C. To this end, an experimental study with associated simulations based on a finite volume method modeling approach is conducted for the inductively heated and fluidized pebble bed (PB) concept. A coupled electromagnetic and thermal model is implemented and validated using data from the experimental study. Acceptable deviations less than 15% occur for the air outlet temperature at Reynolds numbers larger than 2000 due to the assumptions of a homogenous external magnetic field and due to the neglected radiation effects. Therefore, the introduced modeling approach can be applied as a solid basis for the identification of inductively heated PB gas heater design solutions with high efficiency and power density.

Parameter studies are conducted based on the validated model to identify energy-efficient designs with high power density for high-temperature application below and far beyond the Curie point of carbon steel at $T_C = 768°C$. Key performance indicators such as volumetric power density, PtH efficiency and heat flux density have been chosen to evaluate the performance of the PtH concept. In case of $T_{Solid} < T_C$, results for the PtH efficiency and power density reveal that the optimal operation range for the ferromagnetic steel UNS G10060 PB is around 580 °C using a fully packed bed design with small particles ranging from 10 mm to 30 mm. Such design solutions enable PtH efficiencies above 90% at heat flux densities over 2.0 W/cm². For high-temperature applications with $T_{Solid} > T_C$, where only non-magnetic materials can be used, an exemplary Brayton battery use case is considered. In that case, efficiencies above 95% and power densities higher than 5.5 MW/m³ are found for the first time in the electrical conductivity range of 40,000 $\Omega^{-1}m^{-1}$ and 190,000 $\Omega^{-1}m^{-1}$. Silicon-infiltrated silicon carbide (SiSiC) offers candidates in this range. Therefore, the semiconducting SiSiC is proposed as a suitable material solution for the application beyond the Curie point of steel.

Altogether, this investigation has led to a greater process understanding of the novel PtH concept and has verified its applicability demonstrating high efficiencies along with high power densities for temperatures below the Curie point of carbon steel. However, for temperatures above this Curie point only theoretical outcomes have been discussed, thus experimental proof of the concept under the working conditions of a Brayton battery is pending. Therefore, further work aims at testing the induction air heater inside a pressure vessel at temperatures far beyond the Curie point of steel.

Author Contributions: Conceptualization, S.B.; methodology, S.B.; software, S.B. and O.K.; experiments, O.K.; validation, S.B.; formal analysis, S.B.; investigation, S.B.; resources, S.B.; data curation, S.B.; writing—original draft preparation, S.B.; writing—review and editing, S.B., O.K. and S.Z.; visualization, S.B.; supervision, S.Z.; project administration, S.Z.; funding acquisition, S.Z.
All authors have read and agreed to the published version of the manuscript.

Funding: This research received no external funding.

Conflicts of Interest: The authors declare no conflict of interest.

Nomenclature

A_{HTF}	area provided by the pebble bed for heat transfer (m²)
B	magnetic flux density (T or kg s^{-2}A^{-1})
c_p	specific heat capacity (J kg^{-1} K^{-1})
d	sphere diameter (m)
D_{PB}	bed diameter (m)
E	electric field strength (V m^{-1})
f	frequency (Hz)
F	power transmission factor of a sphere (-)
H	magnetic field strength (A m^{-1})
H_{PB}	bed height (m)
I_i	inductor's peak current (A)
k	damping coefficient (m^{-1})
K	Nagaoka's correction factor (-)
l	length (m)
$\dot{m}_f$	mass flow rate (kg s^{-1})
n	number of spheres (-)
N_i	number of inductor turns (-)
$P_{el,in}$	electric power input at coil terminals (W)
p_{ind}	specific electric power per unit volume (W m^{-3})
$P_{ind,tot}$	total electrically induced power input (W)
$\dot{q}_{ind}$	Joule heat power density (W m^{-3})
$\dot{q}_{tot}$	total heat flux density to HTF (W cm^{-2})
r	sphere radius (m)
R_e	Reynolds number (-)
T	temperature (°C)
t	time scale (s)
V	volume (m^3)
$\dot{V}_f$	volume flow rate (m^3 s^{-1})
w_f	free flow velocity (m s^{-1})
x_δ	relative skin depth $x_\delta = \delta/d$ (-)
$\overline{x}$	averaged quantity x
$\boldsymbol{X}$	vector quantity X
Greek symbols	
δ	skin depth (m)
ε	void fraction (-)
η	energetic efficiency $\eta_{PtH} = \dot{Q}_{th,out}/P_{el,in}$
λ	thermal conductivity (W m^{-1} K^{-1})
μ_0	magnetic field constant $4\pi 10^{-7}$(N A^{-2})
μ	relative magnetic permeability (-)
ρ	density (kg m^{-3})
σ	electrical conductivity (Ω^{-1}m^{-1})
ω	angular frequency (Hz)
Subscripts and Superscripts	
C	Curie point / Curie temperature
EFH	electric flow heater / electric fluid heater
HT	high-temperature
HTF	heat transfer fluid
PB	pebble bed
PtH	power-to-heat
SiSiC	silicon-infiltrated silicon carbide
TES	thermal energy storage
s/f	solid/fluid phase
i	Inductor / induction coil

Appendix A

The solution of Equation (12) requires the spatial distribution of the electric field $\boldsymbol{E_\phi}$ as given by Equation (5). The integration of these equations bases on the assumption that the electric field distribution is constant throughout every cell in the mesh of the steel spheres. As an approximation, this constant value is taken at the centroid of every cell. Consequently, to accurately represent the induced heat flux, the cells need to be sufficiently small as compared to the spatial gradient of the electric field.

To evaluate the numerical scheme, a grid refinement study is conducted by increasing the number of layers added at the internal surface of the spheres. The case of 30 mm spheres and the highest flow inlet velocity of 3.05 m/s is chosen as it represents the highest energy dynamics. This translates to the highest Reynolds number, which implies the smallest thermal boundary layer thickness. Similarly, since the skin depth δ is constant, the largest sphere has the smallest energy input depth as compared to its diameter. Therefore, this case represents the worst-case scenario for mesh density requirements at the interface between the spheres and the flow for both the internal heat generation and the external heat transfer. The volumetric power density and the total power is plotted as a function of mesh elements in Figure A1. As shown in the figure, for increasing number of mesh layers, the total induced heat input to the system converges with a relative error of less than 0.5% at above 57 Mio. elements, which corresponds to 30 inflation layers.

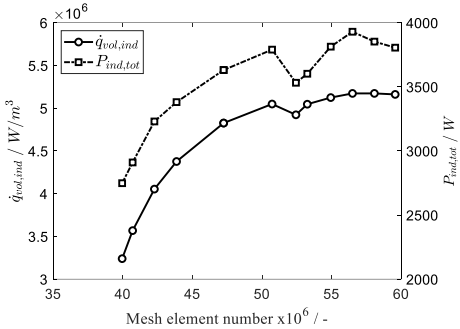

Figure A1. Grid refinement study presented for case 1 with 30 mm particle diameter and 3.05 m/s air velocity at the inlet.

References

1. Böttger, D.; Götz, M.; Lehr, N.; Kondziella, H.; Bruckner, T. Potential of the power-to-heat technology in district heating grids in Germany. *Energy Procedia* **2014**, *46*, 246–253. https://doi.org/10.1016/j.egypro.2014.01.179.
2. Välilä, K.; Laing-Nepustil, D.; Nepustil, U. Power-to-Heat—Wo könnte es hingehen? *Z. Energ.* **2020**, *44*, 247–259. https://doi.org/10.1007/s12398-020-00288-4.
3. Sergio, L. Fundamentals of Electroheat. In *Electrical Technologies for Process Heating*; Springer: Cham, Switzerland, 2017.
4. Lucía, O.; Maussion, P.; Dede, E.J.; Burdío, J.M. Induction heating technology and its applications: Past developments, current technology, and future challenges. *IEEE Trans. Ind. Electron.* **2014**, *61*, 2509–2520.
5. Lupi, S.; Michele, F.; Aleksandr, A. *Induction and Direct Resistance Heating*; Springer: Cham, Switzerland, 2015.
6. Ohmex, Electrical Process Flow Heaters Datasheet. 2021. Available online: https://www.ohmex.de/en/wp-content/uploads/sites/3/2020/03/electric-process-heater_STR_2020-03.pdf (accessed on 25 April 2022).
7. Schniewindt, Flow Heaters. 2021. Available online: https://www.schniewindt.de/en/csn-flow-heaters/ (accessed on 25 April 2022).
8. Curran, J.S.; Featherstone, A.M. Electric-induction fluid heaters. *Power Eng. J.* **1988**, *2*, 157–160.
9. Vecchi, A.; Knobloch, K.; Liang, T.; Kildahl, H.; Sciacovelli, A.; Engelbrecht, K.; Li, Y.; Ding, Y. Carnot Battery development: A review on system performance, applications and commercial state-of-the-art. *J. Energy Storage* **2022**, *55*, 105782.
10. Benato, A. Performance and cost evaluation of an innovative pumped thermal electricity storage power system. *Energy* **2017**, *138*, 419–436. https://doi.org/10.1016/j.energy.2017.07.066.

11. Chen, L.X.; Hu, P.; Zhao, P.P.; Xie, M.N.; Wang, F.X. Thermodynamic analysis of a high-temperature pumped thermal electricity storage (HT-PTES) integrated with a parallel organic Rankine cycle (ORC). *Energy Convers. Manag.* **2018**, *177*, 150–160.
12. Sergej, B. Techno-economic evaluation of a Brayton Battery configuration with Power-to-Heat extension. *J. Energy Storage* **2023**, *62*, 104570.
13. Unver, U.; Yuksel, A.; Kelesoglu, A.; Yuksel, F.; Unver, H.M. Analysis of a novel high performance induction air heater. *Therm. Sci.* **2018**, *22* (Suppl. 3), 843–853.
14. Unver, U. Efficiency analysis of induction air heater and investigation of distribution of energy losses. *Teh. Vjesn.* **2016**, *23*, 1259–1267. https://doi.org/10.17559/TV-20151122224719.
15. Baumeister, E.B.; Bennett, C.O. Fluid-particle heat transfer in packed beds. *AIChE J.* **1958**, *4*, 69–74.
16. Eichorn, J.A.C.O.B.; Robert, R.W. Particle to Fluid Heat Transfer in Fixed and Fluidized Beds. *Chem. Eng. Progr. Symp. Ser. 48, No 4, 11,* **1952**.
17. Xu, G.; Sun, Z.; Meng, X.; Zhang, X. Flow boiling heat transfer in volumetrically heated packed bed. *Ann. Nucl. Energy* **2014**, *73*, 330–338.
18. Leininger, S.; Kulenovic, R.; Rahman, S.; Repetto, G.; Laurien, E. Experimental investigation on reflooding of debris beds. *Ann. Nucl. Energy* **2014**, *74*, 42–49.
19. Duquenne, P.; Deltour, A.; Lacoste, G. Application of inductive heating to granular media: Temperature distribution in granula bed. *Int. J. Heat Mass Transf.* **1993**, *36*, 2473–2477. https://doi.org/10.1016/S0017-9310(05)80130-9.
20. Duquenne, P.; Deltour, A.; Lacoste, G. Application of inductive heating to granular media: Modelling of electrical phenomena. *Can. J. Chem. Eng.* **1994**, *72*, 975–981.
21. Kennedy, M.W.; Akhtar, S.; Bakken, J.A.; Aune, R.E. Review of classical design methods as applied to aluminum billet heating with induction coils. In Proceedings of the EPD Congress 2011-TMS 2011 Annual Meeting and Exhibition, San Diego, CA, USA, 27 February–3 March, 2011; pp. 707–722.
22. Poritsky, H. Conducting sphere in alternating magnetic fields. *Trans. Am. Inst. Electr. Eng. Part I: Commun. Electron.* **1960**, *78*, 937–942.
23. Nagaoka, H. The inductance coefficients of solenoids. *J. Coll. Sci. Imp. Univ. Tokyo Jpn.* 1909, *27*, 1–33.
24. *Rocky 4.4 DEM Technical Manual*; 2020.
25. *High-Temperature Property Data: Ferrous Alloys*; Rothman, M., Ed.; ASM International: 1988; United States
26. Silca Refractory Solutions. "Thermal Insulation, Non-Ferrous Meatal Casting & Fire Protection" Catalogue 2018. Available online: https://www.silca-online.de/fileadmin/2.pdf/04.produktdatenblaetter-ht-en/PDB-SILCAFELT_EN.pdf (accessed on 15 July 2022).
27. BCE Special Ceramics. "Comparison Table for Technical Ceramics" 2021. Available online: https://www.bce-special-ceramics.com/comparison/bce-material-table.htm (accessed on 15 July 2022).
28. Lucks, C.; Deem, H. *Thermal Properties of 13 Metals*; Special Technical Publication No. 227; ASTM: 1958.
29. *Engineering Properties of Steel*; Harvey, P., Ed.; ASM: 1982; United States
30. Frenzelit GmbH. "Novamica®—Phlogopite Mica Gaskets. Available online: https://www.frenzelit.com/fileadmin/produkte/dichtungen/novamica/de_en/Brochure_novamica_en.pdf (accessed on 16 July 2022).
31. Hänchen, M.; Brückner, S.; Steinfeld, A. High-temperature thermal storage using a packed bed of rocks–heat transfer analysis and experimental validation. *Appl. Therm. Eng.* **2011**, *31*, 1798–1806. https://doi.org/10.1016/j.applthermaleng.2010.10.034.

2.3 Paper II (meso scale): Development of a compact EFH design model

Sergej Belik, Volker Dreissigacker and Stefan Zunft

The following research paper was published in
Journal of Energy Storage
Volume 50, June 2022, 104570
https://doi.org/10.1016/j.est.2022.104570

Contribution roles
Sergej Belik:
Research work - Conceptualization, methodology, software and model development, investigation, formal analysis and data curation
Writing - Conceptualization, original draft preparation, review, editing and visualization

Volker Dreissigacker:
Research work - Investigation
Writing - Reviewing and editing

Stefan Zunft:
Reviewing, editing and supervision

Journal of Energy Storage 50 (2022) 104570

Contents lists available at ScienceDirect

Journal of Energy Storage

journal homepage: www.elsevier.com/locate/est

Power-to-heat integration in regenerator storage: Enhancing thermal storage capacity and performance

Sergej Belik *, Volker Dreissigacker, Stefan Zunft

Institute of Engineering Thermodynamics, German Aerospace Center (DLR), Stuttgart, Germany

ARTICLE INFO

Keywords:
Power-to-heat
Electric flow heater
Regenerator storage
Electrothermal energy storage
Storage power plant
Thermodynamic analysis

ABSTRACT

Electrically heated regenerator storage is an energy- and cost-efficient solution for converting excess electricity and storing it as high-temperature heat. We introduce a transient model to describe the thermodynamic behavior of this hybrid storage system with the fewest number of dimensionless parameters. These characteristic parameters are used to derive key performance indicators for the thermodynamic assessment of the power-to-heat integration in regenerator storage. The results obtained from simulation studies indicate the energy-efficient location of electric heating elements inside the storage tank and provide designs with significantly improved thermal storage capacity and performance. These benefits from power-to-heat extension are particularly evident in the increased cost efficiency and operational flexibility.

1. Introduction

Electrically heated regenerator storage has recently received significant attention for applications in storage power plants [1,2], electrothermal energy storage [3] and Brayton based pumped thermal electricity storage [4] due to the feasibility of converting excess electricity into heat and storing it cost effectively at various temperature levels [5]. This heat is then reconverted by a power cycle to produce electricity on demand [6,7]. As illustrated in Fig. 1, such a storage system connects a power unit, which is an electric flow heater (EFH), with a solid media thermal energy storage (STES) unit.

1.1. Power-to-heat unit: electric flow heater

High temperature EFHs are currently used industrially in various types and power levels [8,9]. In the megawatt scale, the most common type is the tubular EFH [9]. This type offers a large heat transfer area and is primarily used in plant engineering as well as in the chemical industry for drying and air-conditioning with gaseous media [10]. The gaseous heat transfer fluid (HTF), which is typically air, flows in direct contact along the tubular heating elements, providing high-temperature process heat at maximum gas temperatures in the range of 600 to 700 °C [9]. This power-to-heat technology provides high-temperature heat at low costs and is proposed by many authors to charge the STES unit in various storage applications [3–5].

1.2. Storage unit: solid media thermal energy storage

The STES is a counterflow regenerator thermal energy storage (TES) unit that has been proven in high-temperature applications for the steelmaking and glass industries [11]. The basic concept consists of a thermally insulated reservoir through which hot gas flows, transferring heat to the porous solid media in direct contact. After this charging period, the source of gas changes from hot to cold so that the stored thermal energy is recovered by the cold gas. A gaseous HTF, such as air, is used in combination with high-temperature inventory materials, including perforated bricks, rocks, slag and ceramics. For such low-cost materials, the maximum operating temperature ranges from 800 to 1200 °C [5,7,11].

Numerous theoretical research studies have addressed the modeling and thermodynamic analysis of the regenerator storage. In addition to the extensive work by Hausen [12] and Schumann [13], Schmidt and Willmott [14] provide a comprehensive collection of several modeling approaches and derived design techniques based on First Law considerations. Both contributions serve as a basis for various theoretical [11,15,16] and experimental works [11,17,18] that further investigate the STES unit. In addition to the mentioned contributions, Singh et al. [19] and Escene et al. [20] perform a comprehensive literature study on numerous publications investigating the conception, thermodynamic behavior and design of the STES component.

* Corresponding author.
E-mail address: Sergej.Belik@dlr.de (S. Belik).

https://doi.org/10.1016/j.est.2022.104570
Received 10 September 2021; Received in revised form 23 March 2022; Accepted 29 March 2022
Available online 19 April 2022

Nomenclature

a_v	surface area to volume ratio related to the solid phase (m^{-1})
a_w	surface area to volume ratio related to the wall (m^{-1})
c_p	specific heat capacity (J kg^{-1} K^{-1})
C_{TES}	ratio of STES storage capacity to the amount of energy delivered by STES
f_{mat}	material related factor, see Eqs. (8a) and (8b)
H	total length (m)
k_v	heat transfer coefficient related to the solid phase (W m^{-2} K^{-1})
m	storage mass (kg)
$\dot{m}_f$	mass flow rate (kg s^{-1})
P_{el}	electrical power input (W)
$\dot{Q}_{PtH}$	Joule heat induced by electric heating (W)
$\dot{q}_{PtH}$	Joule heat power density (W m^{-3})
$q_{EH-STES}^*$	averaged gravimetric energy density (J kg^{-1} K^{-1}), see Eq. (16)
St	Stanton number
t	time scale (s)
$\Delta T_{f,drop}$	relative outlet temperature drop during discharging (%)
$T_{f,in}$	normalized inlet temperature (–)
$\overline{T}_{f,out}^{'}$	normalized averaged outlet temperature
$T_{f,out,mix}^{'}$	normalized temperature at the mixing point for bypass operation
U_w	heat transfer coefficient related to the wall (W m^{-2} K^{-1})
V	volume (m^3)
w_f	free flow velocity (m s^{-1})
z	length scale (m)
z_{EFH}	dimensionless heating area, H_{EFH}/H

Greek symbols

ε	void fraction (–)
ζ	storage utilization ratio, see Eqs. (17a) and (17b)
η_{PtH}	electric heating efficiency, $\dot{Q}_{PtH}/P_{el}$
η_{ex}	exergetic efficiency
ϑ	temperature (K)
$\Delta\vartheta_{in}$	maximum inlet temperature difference between charging and discharging (K)
λ	thermal conductivity (W m^{-1} K^{-1})
ξ	coefficient of uniformity, see Eq. (19)
ρ	density (kg m^{-3})
τ	duration of charging period (s)
Γ	dimensionless loss number
Λ	reduced (dimensionless) length
Π	reduced (dimensionless) period duration
Φ	dimensionless heat source number
$\dot{X}_{EFH}$	dimensionless exergy rate, see Eq. (12)

Subscripts

EH-STE	electrically heated STES
EFH	electric flow heater
HTF	heat transfer fluid
PtH	power-to-heat
STES	solid media thermal energy storage
TES	thermal energy storage
in	inlet
out	outlet
s	solid phase
f	fluid phase (heat transfer fluid)
0	ambient

Superscripts

′	related to discharging period
$\overline{x}$	averaged quantity x
x^*	normalized quantity x

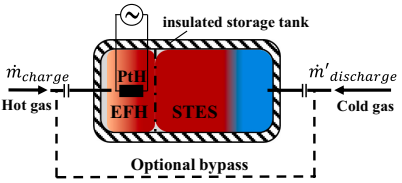

Fig. 1. Schematic representation of a solid media thermal energy storage system with an electric flow heater and optional discharging bypass.

1.3. Electrically heated solid media thermal energy storage: Scope and method

The object of our detailed investigation is a storage system referred to as an electrically heated STES (EH-STES) system. According to Fig. 1, this hybrid system comprises an EFH component connected to a STES component. The EFH is located either inside the thermal reservoir, as indicated in the Fig. 1 scheme, or outside. A gaseous HTF transports high-temperature heat from the EFH to the STES unit during the charging operation. The discharge principle is similar to that of the counterflow regenerator, except that the sensible heat of the EFH is used in addition to the recovered heat of the STES.

Few existing scientific publications have investigated EH-STES systems. Forsberg et al. [7] and Stack et al. [5] propose a concept referred to as FIRES, which consists of metallic heater wires contacted with a firebrick storage medium to heat it to temperatures above 1000 °C. During this charging process, the heater wires transfer the heat to the storage material via thermal radiation and thermal conduction. The discharging process is analogous to the regenerator storage. This investigation focuses on the discharging process using a one-dimensional approach to model the thermal energy storage. The heat source term is simply formulated by a constant heat flux boundary condition [7]. Zubair et al. [21] analyze a similar concept, focusing on the thermoeconomics of the storage system. The power-to-heat (PtH) source term is given by a constant electric power without detailed modeling of the heating component. Furthermore, Dreissigacker et al. [22] and Houssainy et al. [23] propose a storage system consisting of an EFH connected in series with a packed bed TES unit. This STES component is described by a simplified transient and one-dimensional model considering the thermal resistance within the packed bed. The EFH component, in contrast, is modeled by a stationary model that assumes an ideal conversion of electric to thermal power.

The presented literature survey shows that investigations of EH-STES systems have focused on detailed modeling of the STES unit. The electric heater, conversely, has been modeled in a simplified way based on stationary models so that statements about component size and transient heat transfer behavior in combination with a STES unit cannot be conducted. Therefore, the purpose of the present contribution is to introduce and apply a numerical model that describes the thermodynamic

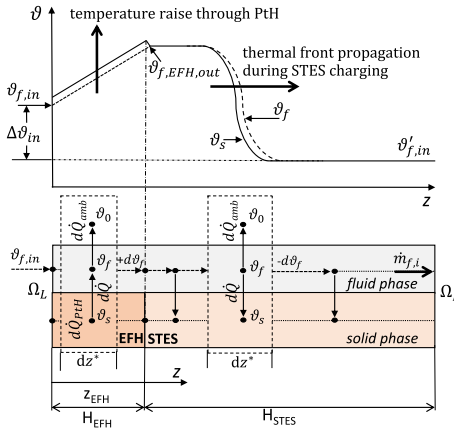

Fig. 2. Schematic illustration of temperature profiles during charging mode with associated discretization scheme of the two-phase region.

behavior of both components in one hybrid storage system.

To this end, we propose a compact and dimensionless model that describes the thermodynamic behavior of the EH-STES system with the fewest number of characteristic parameters. The first step is to simplify the one-dimensional model provided by Schumann [13] and develop it into a formulation with dimensionless parameters. These characteristic parameters are used in a second step to derive technical key performance indicators (KPIs) for assessing the PtH integration. Subsequently, a simulation study is conducted varying characteristic parameters to identify the most beneficial location for the electric heating elements in terms of energy density and corresponding thermodynamic efficiency. Another simulation study shows the impact of PtH integration on the thermal storage capacity and provides recommendations for energy-efficient design solutions with maximum storage utilization. The final study quantifies the improvement in storage performance based on power-related KPIs.

2. Model description

The objective of the numerical analysis is to develop the simplest possible but nontrivial model that enables the calculation of the thermodynamic behavior of the EFH and STES unit under cyclic conditions. Consequently, Schumann's simplified two-phase transient and one-dimensional model [13,16] is used as a basis for further modifications. This modeling approach only considers heat transport in the axial direction. It neglects heat conduction in this direction due to the low effective thermal conductivity for both the solid and fluid phases. Moreover, no heat generation is considered in this model.

In addition to these assumptions, the following simplifications are made:

- the accumulation term of the fluid phase is neglected due to its marginal thermal capacity.
- the solid and fluid thermophysical properties are temperature independent.
- the influence of the thermal resistance inside the solid media is neglected since the heat transfer resistance dominates with a small biot number (Bi <0.10).

As depicted in Fig. 2, modifications to this model include separating the solid phase into two regions, one for the TES inventory and another for the EFH heating area and its occurring heat generation. This heat is produced according to the principle of Joule heating and is considered with a source term in Eq. (1b), which is the heat balance equation of the solid phase. In the fluid phase, the term for thermal losses to the ambient is considered for both components. With these considerations, the temporally and spatially varying temperature field during thermal cyclic operation is calculated for both phases as well as for both components, the STES unit (Eq. notation 'a') and the EFH unit (Eq. notation 'b').

Solid phase of the STES unit:

$$\frac{d\vartheta_s}{dt} = \frac{k_v\, a_v}{(1-\varepsilon)\rho_{TES} c_{p,TES}} \left(\vartheta_f - \vartheta_s\right) \tag{1a}$$

with adiabatic boundary condition at $\Omega_R: -\lambda \frac{\partial \vartheta_{TES}}{\partial z} = 0$

Solid phase of the EFH unit:

$$\frac{d\vartheta_s}{dt} = \frac{\dot{Q}_{PtH}}{V_{EFH}(1-\varepsilon)\rho_{EFH} c_{p,EFH}} + \frac{k_v\, a_v}{(1-\varepsilon)\rho_{EFH} c_{p,EFH}} \left(\vartheta_f - \vartheta_s\right) \tag{1b}$$

with adiabatic boundary condition at $\Omega_L: -\lambda \frac{\partial \vartheta_{EFH}}{\partial z} = 0$

Fluid phase of the STES unit:

$$\frac{d\vartheta_f}{dz_{TES}} = \frac{k_v\, a_v}{w_f\, \varepsilon\, \rho_f\, c_{p,f}} \left(\vartheta_s - \vartheta_f\right) - \frac{U_w\, a_w}{w_f\, \varepsilon\, \rho_f\, c_{p,f}} \left(\vartheta_f - \vartheta_0\right) \tag{2a}$$

with adiabatic boundary condition at $\Omega_R: -\lambda \frac{\partial \vartheta_f}{\partial z} = 0$

Fluid phase of the EFH unit:

$$\frac{d\vartheta_f}{dz_{EFH}} = \frac{k_v\, a_v}{w_f\, \varepsilon\, \rho_f\, c_{p,f}} \left(\vartheta_s - \vartheta_f\right) - \frac{U_w\, a_w}{w_f\, \varepsilon\, \rho_f\, c_{p,f}} \left(\vartheta_f - \vartheta_0\right) \tag{2b}$$

with constant temperature boundary conditions for the inlet at $\Omega_L: T_f = \frac{\vartheta_{f,in}}{\Delta\vartheta_{in}}$where ϑ_s and ϑ_f represent the solid medium and the HTF temperatures of the EFH and the STES unit for the convective heat transfer. In addition to this heat transfer mechanism, heat losses to the ambient are described on the right-hand side of Eq. (2b) using the reference temperature ϑ_0. Moreover, $\dot{Q}_{PtH}$ represents the electrically produced heat inside the total volume V_{EFH} of the EFH body; k_v and U_w denote the heat transfer coefficients to the porous media and to the wall together with the related surface area to volume ratios a_v and a_w. Furthermore, w_f represents the HTF velocity and ε gives the void fraction. The specific heat capacity c_p and the density ρ are given for the solid and fluid media, respectively. For simplicity, the STES unit and EFH void fractions are assumed to be equal, as well as the surface area to volume ratio a_v.

Assuming a balanced and symmetric operation of the EH-STES system with an identical duration of charging and discharging periods ($\tau = \tau'$); identical mass flow rates ($\dot{m}_f = \dot{m}'_f$) and additional normalization in the time $dt = dt^* * \tau$, space $dz = dz^* * H$ and temperature $d\vartheta_{s,f} = dT_{s,f} * \Delta\vartheta_{in}$, Eqs. (1a), (1b) and Eqs. (2a), (2b) may be expressed in the normalized form with the referenced temperature $\Delta\vartheta_{in}$, which is also the maximum temperature difference between the HTF inlets during charging and discharging: $\Delta\vartheta_{in} = \vartheta_{f,\,in} - \vartheta'_{f,\,in}$.

Solid phase:

$$\frac{dT_{s,TES}}{dt^*} = \frac{St_{TES}}{1-\varepsilon} \frac{\left(\vartheta_{f,TES} - \vartheta_{s,TES}\right)}{\Delta\vartheta_{in}} \tag{3a}$$

$$\frac{dT_{s,EFH}}{dt^*} = \Phi\, St_{EFH} + \frac{St_{EFH}}{1-\varepsilon} \frac{\left(\vartheta_{f,EFH} - \vartheta_{s,EFH}\right)}{\Delta\vartheta_{in}} \tag{3b}$$

Fluid phase:

$$\frac{dT_{f,TES}}{dz^*_{TES}} = \Lambda_{TES} \frac{\left(\vartheta_{s,TES} - \vartheta_{f,TES}\right)}{\Delta\vartheta_{in}} - \Gamma_{TES} \frac{\left(\vartheta_{f,TES} - \vartheta_0\right)}{\Delta\vartheta_{in}} \tag{4a}$$

$$\frac{dT_{f,EFH}}{dz^*_{EFH}} = \Lambda_{EFH} \frac{\left(\vartheta_{s,EFH} - \vartheta_{f,TES}\right)}{\Delta\vartheta_{in}} - \Gamma_{EFH} \frac{\left(\vartheta_{f,EFH} - \vartheta_0\right)}{\Delta\vartheta_{in}} \tag{4b}$$

Eqs. (3a) through (4b) describe the thermodynamic behavior of the EH-STES system, which is characterized by four dimensionless parameters for the solid media TES and EFH materials. These parameters are defined below:

Reduced (dimensionless) length

$$\Lambda_{TES} = \frac{k_v\, a_v}{w_f\, \varepsilon\, \rho_f\, c_{p,f}} H_{TES} \tag{5a}$$

$$\Lambda_{EFH} = \frac{k_v\, a_v}{w_f\, \varepsilon\, \rho_f\, c_{p,f}} H_{EFH} \tag{5b}$$

The total reduced length Λ may be expressed as the sum of the reduced lengths of the individual components:

$$\Lambda = \Lambda_{TES} + \Lambda_{EFH} \tag{6}$$

Dimensionless loss number

$$\Gamma_{TES} = \frac{U_w a_w}{w_f \varepsilon\, \rho_f c_{p,f}} H_{TES} \tag{7a}$$

$$\Gamma_{EFH} = \frac{U_w a_w}{w_f \varepsilon\, \rho_f c_{p,f}} H_{EFH} \tag{7b}$$

The total dimensionless loss number Γ may be defined by $\Gamma = \Gamma_{TES} + \Gamma_{EFH}$ in analogy to the definition of the total reduced length Λ. Since STES for utility-scale applications have a small surface area to volume ratio a_v [12], thermal insulation losses are neglected for further investigation ($\Gamma = 0$).

Stanton number

$$St_{TES} = \frac{k_v\, a_v\, \tau}{\rho_{TES}\, c_{p,TES}} \tag{8a}$$

$$St_{EFH} = \frac{k_v a_v\, \tau}{\rho_{EFH}\, c_{p,EFH}} = St_{TES}{}^{*} f_{mat} \tag{8b}$$

Since both numbers differ by material properties, their relationship can be described by the material related factor:

$$f_{mat} = \frac{\rho_{TES}\, c_{p,TES}\, (1-\varepsilon)}{\rho_{EFH}\, c_{p,EFH}\, (1-\varepsilon)} \tag{9}$$

The Stanton number *St* could also be expressed by the reduced period duration Π, which is defined as the dimensionless time available for the thermal front to propagate through the thermal reservoir. Hausen [12] first introduced this parameter together with Λ.

$$St = \Pi(1-\varepsilon) \tag{10}$$

Dimensionless heat source number

$$\Phi = \frac{\dot{Q}_{PtH}}{V_{EFH}(1-\varepsilon)\, k_v\, a_v\, \Delta\vartheta_{in}} = \frac{\dot{q}_{PtH}}{k_v\, a_v\, \Delta\vartheta_{in}} \tag{11}$$

The dimensionless heat source number describes the ratio of the external heat source $\dot{Q}_{PtH}$ to the heat transferred to the HTF. Furthermore, Φ may be expressed by the Joule heat power density $\dot{q}_{PtH}$, which is defined as the electrical power P_{el} converted into heat with the efficiency η_{PtH} inside the solid volume $V_{s,EFH} = V_{EFH}\,(1-\varepsilon)$. According to Ohm's law, this value is also given by the current density J and the electrical resistivity $\rho_{el,PtH}$ of the PtH body:

$$\dot{q}_{PtH} = \frac{P_{el}\, \eta_{PtH}}{V_{EFH}\,(1-\varepsilon)} = |J|^2 \rho_{el,PtH} \tag{12}$$

3. Technical key performance indicators

The derived dimensionless technical parameters allow for a compact and universal technology assessment of the EH-STES system. To this end, the characteristic parameters *St*, Λ and Φ are used to derive the key performance indicators (KPIs), which quantify the influence of the PtH integration in terms of system performance and thermal storage capacity.

The capacity-related KPIs used in this study are the gravimetric energy density and the utilization ratio of the storage material. In addition to the technical assessment, both of these indicators serve as a basis for an economic assessment in terms of capital costs. The performance-related KPI is the coefficient of uniformity, which describes the uniformity of the outlet temperature during discharging. This indicator is essential as it directly evaluates the technology-specific drop in discharge power. This performance-related KPI may be used to calculate operational costs to evaluate the economics of the storage operation. The power-related and capacity-related KPIs are introduced in the following subsections together with the thermodynamic efficiency.

3.1. Thermodynamic efficiency of the storage system

The primary loss mechanism influencing the thermodynamic efficiency of solid media-based regenerators is the charging loss at the outlet of the cold end of the storage tank. This parameter depends on the regenerator length Λ, the heat source number Φ, the resulting temperatures at the cold-end outlet and the exergy loss due to irreversible heat transfer between solid and fluid media. Neglecting the heat losses to the ambient with $\Gamma = 0$, the round-trip efficiency of the EH-STES system may be expressed as:

$$\eta_{EH-STES} = \frac{\dot{m}'_f{}^{*} c_{p,f}{}^{*} \int_0^{t'^{*}=1} \left(T'_{f,out-} - T'_{f,in}\right) dt^{*}}{\dot{m}_f{}^{*} c_{p,f}{}^{*} \left(\int_0^{t^{*}=1} \left(T_{f,in-} T'_{f,in}\right) dt^{*} + \dot{X}_{EFH}{}^{*} \tau \right)} \tag{13}$$

The fraction from Eq. (13) can be reduced to a dimensionless expression since we assume a cyclic steady state of the STES operation with identical heat capacity rates during charging and discharging. The heat source of the EFH is considered with the dimensionless exergy rate $\dot{X}_{EFH}$, which equals the fluid temperature raise caused by the EFH:

$$\dot{X}_{EFH} = \Lambda_{EFH}\, \Phi\, (1-\varepsilon) = T_{f,EFH,out} - T_{f,in} \tag{14}$$

The conversion from electrical into thermal energy is assumed without electrical or thermal losses ($\Gamma_{EFH} = 0$), resulting in a maximum PtH efficiency $\eta_{PtH} = 1$. In contrast to this energetic analysis, the specification of the exergetic efficiency is of greater interest for an electrically driven device. Therefore, the exergetic efficiency of the EFH is defined on the basis of the reference temperature T_0:

$$\eta_{ex,EFH} = \frac{\dot{X}_{EFH,out} - \dot{X}_{in}}{\dot{X}_{EFH}} = 1 - \frac{T_0 \left(ln\left(\frac{T_{f,EFH,out}}{T_0}\right) - ln\left(\frac{T_{f,in}}{T_0}\right) \right)}{T_{f,EFH,out} - T_{f,in}} \tag{15}$$

3.2. Gravimetric energy density

The gravimetric energy density cannot be expressed solely based on characteristic parameters. Therefore, averaged heat capacity values for both the EFH and conventional STES materials are assumed with $f_{mat} = 0.6$. The gravimetric energy density is calculated by means of inlet and outlet temperatures for the discharging period and subsequently weighted based on the heating area z_{EFH} of the EFH:

$$z_{EFH} = \frac{\Lambda_{EFH}}{\Lambda_{EFH} + \Lambda_{TES}} = \frac{H_{EFH}}{H_{EFH} + H_{TES}} = \frac{H_{EFH}}{H} \tag{16}$$

Based on the previous temperature normalization, the averaged gravimetric energy density $q_{EH-STES}{}^{*}$ is given in J/kgK:

$$q^{*}_{TES} = \frac{\Pi_{TES}}{\Lambda_{TES}} c_{p,TES} \left(\overline{T}'_{f,STES,out} - T'_{f,in} \right) \tag{17a}$$

$$q^{*}_{EFH} = \frac{\Pi_{EFH}}{\Lambda_{EFH}} c_{p,EFH} \left(\overline{T}'_{f,EH-STES,out} - \overline{T}'_{f,STES,out} \right) \tag{17b}$$

$$q^*_{EH-STES} = q^*_{TES}(1 - z_{EFH}) + q^*_{EFH}\, z_{EFH} \tag{18}$$

where $\overline{T}^{'}_{f,STES,out}$ and $\overline{T}^{'}_{f,EH-STES,out}$ are the averaged outlet temperatures of the STES unit and of the EH-STES system.

3.3. Storage utilization ratio

The propagation of the thermal front in the axial direction depends on the Stanton number and on the reduced regenerator length as well as the heat source number. The resulting temperature profile of the solid phase in the axial direction is used to calculate the storage utilization ratio of the EH-STES system, which relates the utilized thermal storage capacity to a theoretical thermal storage capacity. The storage utilization ratio is given by the maximum temperature difference between the HTF inlets $\Delta T_{in} = T_{f,in} - T'_{f,in}$:

$$\zeta = \frac{Q_{util.}}{Q_{th.}} = \frac{\int_0^{z^*=1} \left(T_{EH-STES}(t^* = \tau z^*) - T^{'}_{EH-STES}(t^* = \tau^{'} z^*)\right) dz^*}{T_{f,in} - T^{'}_{f,in}} \tag{19}$$

In addition, this ratio is also given for the STES unit by:

$$\zeta_{TES} = \frac{Q_{TES,util.}}{Q_{TES,th.}} = \frac{\dot{m}_f\, \tau\, c_{p,f} \left(\overline{T}^{'}_{f,STES,out} - T^{'}_{f,in}\right)}{m_{TES}\, c_{p,TES} \left(T_{f,EFH,out} - T^{'}_{f,in}\right)} \tag{20}$$

where m_{TES} is the storage mass with the appropriate heat capacity $c_{p,TES}$ and $T_{f,EFH,out}$, which is the TES charging temperature caused by the EFH component (see Fig. 2).

In the case of $\zeta_{TES} = 1$ or $\zeta = 1$ for $\Phi = 0$, the thermal reservoir is ideally utilized with a thermal front crossing the entire storage inventory during cyclic operation. As a consequence of the PtH implementation ($\Phi > 0$), utilization ratios larger than one are feasible, thus demonstrating the benefit of capacity enhancement.

3.4. Coefficient of uniformity

In contrast to the utilization ratio, the coefficient of uniformity is a performance-related KPI and describes the uniformity of the discharge temperature at the hot end of the storage tank. It can be expressed as the ratio of fluctuating thermal power to a uniform power output during discharging. Reducing the heat capacity rates, the ratio can be expressed by:

$$\xi = \frac{\ddot{\overline{Q}}_{f,out}}{\dot{Q}_{f,out,max}} = \frac{\int_0^{t^*=1} \left(T^{'}_{f}(t^*, z'^* = H) - T^{'}_{f,in}\right) dt^*}{T_{f,in} - T^{'}_{f,in}} \tag{21}$$

The coefficient of uniformity is also given for the STES by:

$$\xi_{TES} = \frac{\ddot{\overline{Q}}_{f,TES,out}}{\dot{Q}_{f,TES,out,max}} = \frac{\overline{T}^{'}_{f,STES,out} - T^{'}_{f,in}}{T_{f,EFH,out} - T^{'}_{f,in}} = \frac{\Delta \overline{T}^{'}_{f,TES}}{\Delta T^{'}_{f,TES,max}} \tag{22}$$

Thus, a maximum averaged outlet temperature $\overline{T}^{'}_{f,STES,out}$ leads to $\xi_{TES} = 1$ and $\xi = 1$ for $\Phi = 0$. For a PtH operation with $\Phi > 0$, the coefficient of uniformity can be increased to $\xi > 1$ for the storage system, which would enable an advantageous bypass operation to ensure uniform power output at the mixing point.

Table 1
Material combinations for EFH and STES satisfying $\mathbf{f_{mat}} = 0.60$

Materials/property	$\overline{\rho}$ (kg m^{-3})	$\overline{c_p}$ (J kg^{-1} K^{-1})	$\overline{\rho c_p}$ (kJ m^{-3} K^{-1})
EFH-mat1: stainless steel	7700	448	344.96
STES-mat1: oxide ceramics	2300	900	2070.0
EFH-mat2: silicon carbide	3210	1060	344.96
STES-mat2: quartzite	2500	828	2070.0

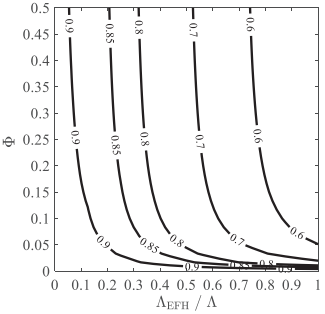

Fig. 3. Contour lines for thermodynamic efficiency $\eta_{EH-STES}$ of the storage system ($\Pi = 100$; $\Lambda = 100$).

4. Simulation setup

The Eq. (3a) through Eq. (4b) are implemented using the commercial simulation tool MATLAB R2019a. The temporal variable temperature profiles are obtained using the implicit centered method for Eqs. (3a) and (3b). The spatially discretized differential Eqs. (4a) and (4b) are solved numerically using the backward finite difference method. Therefore, the uniformly meshed EH-STES model is discretized in $N = 400$ compartments for the total reduced length Λ. In addition, the modeling approach for the STES component (Eqs. (3a) and (4a)) was confirmed using the one-dimensional continuous solid phase model from Ismail et al. [16]. Results for this comparison are presented in Appendix A.

Computations are started from an initial completely discharged state ($\overline{T}_s = 0$). After a transient cyclic mode with a fluid charging ($T_{f,in} = 1.0$ at Ω_L) and discharging ($T'_{f,in} = 0$ at Ω_R) inlet temperatures, the computation stops once the cyclic change of the delivered thermal energy falls below 10^{-4} J. This criterion is reached after six to eight cycles for design configurations with $\Pi = 100$ and $\Lambda = 100$. The corresponding computing time for each cycle additionally depends on the heat source number Φ and ranges from 4.5 to 5.4 s.

5. Results and discussion

In the following subsections, simulation studies based on the Φ-Λ-St model are conducted. First, the storage is investigated according to the location and extension of the EFH inside the storage tank. In the next step, the results for the introduced KPIs based on wide variations of Φ, Λ and Stanton numbers are discussed. This discussion reveals the improvements in storage performance and capacity due to the PtH extension.

5.1. Location and heat rate of the EFH

The analysis of the advantageous location and extension of the EFH is conducted by varying the dimensionless heat source number Φ and the heating area $z_{EFH} = \Lambda_{EFH}/\Lambda$ (see Fig. 2). This value increases from the

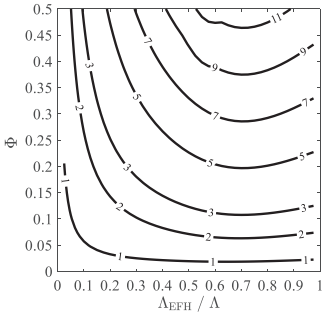

Fig. 4. Contour lines for gravimetric energy density $q_{EH-STES}$* in kJ/(kg K) of the EH-STES system (Π = 100; Λ = 100).

hot end ($z_{EFH} = 0$) of the thermal reservoir, reaching the cold end at $z_{EFH} = 1$. Moreover, the material related factor $f_{mat} = 0.60$ (see Eq. (9)) is applied for further investigations. Feasible material combinations for EFH and STES satisfying $f_{mat} = 0.60$ are presented in Table 1.

Fig. 3 presents the results for the thermodynamic efficiency of the EH-STES system for an example design configuration with a reduced regenerator length Λ = 100 and reduced period duration Π = 100. The contour lines for thermodynamic efficiency decrease with increased Λ_{EFH}/Λ ratio and heat source numbers Φ due to the growing exit loss at the cold end of the thermal reservoir. In contrast, small heating areas and small Φ cause high storage efficiencies but result in low gravimetric energy densities as indicated in Fig. 4. Nevertheless, there is a beneficial operation mode for small heating areas and high heat source numbers. For heating areas $z_{EFH} < 0.20$ and $\Phi \gg 0$, the heater outlet temperature significantly increases, resulting in high values for the energy density while still maintaining a high storage efficiency greater than 0.85. This effect is particularly pronounced for $\Phi > 0.20$ where the thermodynamic efficiency is only marginally affected by the increasing heat source. Qualitatively, the resulting contour lines remain similar for other values of Λ and Π. Thus, small heating masses heated with $\Phi \gg 0$ and located at the hot end of the EH-STES system are beneficial in terms of an energetic evaluation.

5.2. Impact on thermal storage capacity

For a compact presentation and a better interpretation of the following results, the parameter C_{TES} is introduced expressing the ratio of Λ to Π for the TES component. This relationship is valid for the cyclic operation and is given by Eq. (23), which extends the expression for Λ_{TES}/Π_{TES} by the TES inventory volume V_{TES}:

$$C_{TES} = \frac{\Lambda_{TES}}{\Pi_{TES}} = \frac{\rho_{TES}\, c_{p,TES}\, H\,(1-\varepsilon)\, V_{TES}}{w_f\, \rho_f\, c_{p,f}\, \tau\, \varepsilon\, V_{TES}} = \frac{m_{TES}\, c_{p,TES}}{\dot{m}_f\, c_{p,f}\, \tau} \tag{23}$$

This equation can be further extended by the temperature ratio $\Delta\overline{T}'_{f,TES}/\Delta T'_{f,TES,max}$ from Eq. (22). An additional substitution of Eq. (21) into Eq. (20) expresses C_{TES} by the ratio of ξ_{TES} to ζ_{TES}:

$$C_{TES} = \frac{m_{TES}\, c_{p,TES}{}^{*}\Delta T'_{f,TES,max,*}}{\dot{m}_f\, c_{p,f}\, \tau^{*}\Delta\overline{T}'_{f,TES}} \frac{\Delta\overline{T}'_{f,TES}}{\Delta T'_{f,TES,max}} =$$

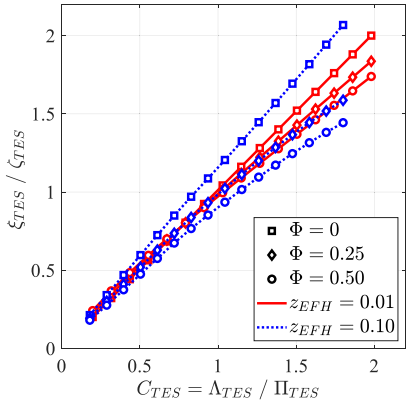

Fig. 5. Proportionality of ξ_{TES} to ζ_{TES} ratio and C_{TES} for Φ = [0 : 0.5], z_{EFH} = 0.10 and z_{EFH} = 0.01.

$$= \frac{Q_{TES,th.}}{\dot{Q}_{f,TES,out,max}\,\tau} = \frac{\xi_{TES}}{\zeta_{TES}} = \frac{\Lambda_{TES}}{\Pi_{TES}} \text{ for } \Phi = 0 \text{ and } z_{EFH} = 0 \tag{24}$$

The Λ_{TES} to Π_{TES} ratio given in Eq. (24) is the proportion of the theoretical thermal storage capacity $Q_{TES,th.}$ to the maximum thermal energy $Q_{f,TES,out,max.}$ delivered by the storage during discharging. Thus, C_{TES} is interpreted as the ratio of the storage size to the amount of energy delivered, which is inversely proportional to q_{TES}* according to Eq. (17a). Moreover, this interpretation could be used for investment decisions where the capital costs are set in relation to the revenues generated from energy sales.

The relationship from Eq. (24) is derived for Φ = 0 and z_{EFH} = 0; nonetheless, the preceding interpretation of C_{TES} could also be used for Φ > 0 and $z_{EFH} > 0$ according to Fig. 5. Here, both the cases with and without PtH are compared for two heating areas. This comparison shows that with increasing heat source numbers and heating areas, the results

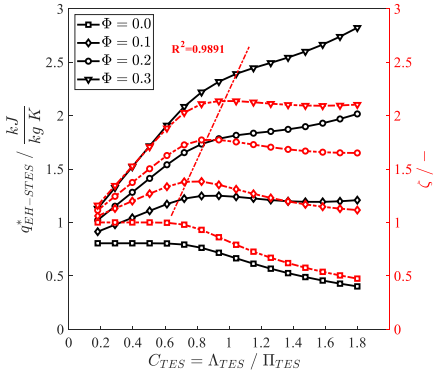

Fig. 6. Gravimetric energy density and storage utilization ration related to Λ and Φ for Π = 100 and $\Lambda_{EFH}/\Lambda = 0.10$

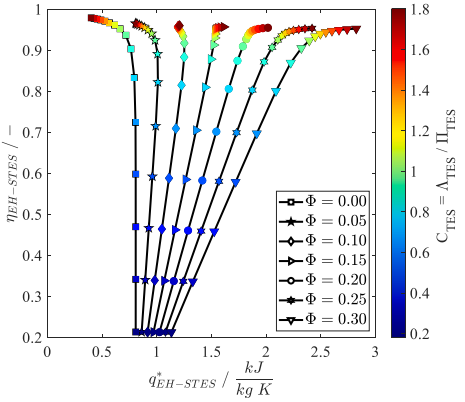

Fig. 7. Thermodynamic efficiency related to Λ and Φ for Π = 100 and Λ_{EFH}/Λ = 0.10

noticeably deviate from the bisector. Nevertheless, the proportionality remains for small heating areas ($z_{EFH} = 0.01$). Although for larger z_{EFH} in combination with Φ > 0 this linearity is slightly damped, the behavior is still interpreted as proportional:

$$C_{TES} = \frac{\xi_{TES}}{\zeta_{TES}} \sim \frac{\Lambda_{TES}}{\Pi_{TES}} \text{ for } 0 < \phi < 0.5 \text{ and } 0 < z < 0.10 \tag{25}$$

Increasing the capacity of the storage tank through inner heat sources results in higher losses in efficiency (see Section 5.1). This effect primarily depends on the heat source number Φ, Λ and Π. To analyze the trade-off between these losses and the energy density, simulation studies varying the characteristic parameters Λ in range from 20 to 200 and Φ from 0 to 0.30 for Π = 50, 100 and 200 are performed. Moreover, the EH-STES system operates in cyclic mode with periodic charging and discharging cycles, in which a heating area $z_{EFH} = 0.10$ is chosen based on the findings from Section 5.1.

The results of the capacity-related KPI are discussed in relation to the PtH implementation before the performance-related results for the thermodynamic efficiency are presented. Fig. 6 depicts the gravimetric energy density and the storage utilization ratio in relation to the Λ_{TES} to Π_{TES} ratio and heat source number Φ. For the reference case without PtH (Φ = 0), there is a limitation of the gravimetric energy density, which is solely caused by material properties since the maximum solid media temperature is determined by the inlet temperature $T_{f,in}$. The inverse proportional relationship from Eq. (17a) explains the continuous decrease of gravimetric energy density for increasing C_{TES} (Fig. 7 shows again this relationship and additionally illustrates the effect on thermodynamic efficiency).

In contrast to the reference case, the gravimetric energy density increases for Φ > 0 due to heating temperatures $T_{f,EFH,out} > 1.0$. This characteristic is attributable to the curve progression of the utilization ratio ζ (dashed lines in Fig. 6), which increases for $0.20 < C_{TES} < 0.80$ due to higher storage utilization in small and additionally heated reservoirs. The subsequent drop for $C_{TES} > 0.80$ results from the dominating increase of the thermal storage capacity provided by large reservoirs. The dashed regression line in Fig. 6 describes the positions of the maximum utilization ratios, which are given by:

$$\zeta_{max} = 3.25\ C_{TES} - 1.0 \,\forall\, C_{TES} \in [0.615,\ 1.12] \tag{26}$$

indicating a high coefficient of determination of $R^2 = 0.9891$. In addition, the maximum utilization ratio may be expressed as a linear function of the dimensionless heat source number $\zeta_{max} = 3.65\ \Phi + 1.0$ with $R^2 = 0.9984$ and $0 \le \Phi \le 0.50$. Combining Eqs. (23) and (26), the maximum utilization ratio may be either expressed with respect to the storage mass or the mass flow rate for given material properties and operating durations.

In addition to the capacity-related KPI presented in Fig. 6, Fig. 7 provides the findings for the thermodynamic efficiency for the previous discussion on beneficial Λ_{TES} to Π_{TES} ratios. These results illustrate that regardless of the energy density, small thermal reservoirs with $0.20 < C_{TES} < 0.80$ indicate low thermodynamic efficiency <85%. In contrast, a high efficiency >85% is achieved for large reservoirs with $C_{TES} > 0.80$ due to the decreasing exit loss at cold end of the thermal reservoir.

Furthermore, Fig. 7 illustrates the impact of PtH on the energy density for various heat source numbers. For Φ < 0.10, the energy density significantly decreases with increases in the reservoir size ($C_{TES} > 0.80$). In contrast, the thermodynamic efficiency increases so that either a maximum energy density or efficiency can be achieved. This behavior has already been discussed in literature [14,22] for the reference case without external heat sources (Φ = 0). Integrating PtH with heat source numbers Φ > 0.10 allows rising values for both the thermodynamic efficiency and energy density. Thus, large thermal reservoirs with short charging and discharging periods ($C_{TES} > 1$) not only lead to high efficiency but also to high energy density, whereby higher heat source numbers result in a slight loss in efficiency. This loss is marginal comparing constant C_{TES} values; however, the energy density significantly increases with higher heat source numbers: a heat source number of Φ = 0.30 results in an efficiency drop of 3.3 percentage points for $C_{TES} = 1.0$ but increases the gravimetric energy density from 0.66 kJ/kg K at Φ = 0 to 2.39 kJ/kg K.

Demanding a high energy density in addition to high efficiency leads to EH-STES design configurations that suggest either $C_{TES} > 1.0$ for Φ > 0.10 or $0.80 < C_{TES} \le 1.0$ for $\Phi \le 0.10$. Here, a heat source number of Φ = 0.10 leads to a loss in thermodynamic efficiency by a maximum of 2.0 percentage points but an improvement in gravimetric energy density by 63.7% for $C_{TES} = 0.80$ and 86.7% for $C_{TES} = 1.0$.

Additional results from simulation studies for Π = 50 and Π = 200 show analogous curve characteristics compared to those presented in Figs. 6 and 7; however, the maximum value for the utilization ratio shifts to $C_{TES} = 0.75$ for Π = 50 and $C_{TES} = 1.05$ for Π = 200. In conclusion, the EH-STES designs that provide maximum thermal utilization for a given Φ as well as a thermodynamic efficiency greater than 90% are identified for Λ_{TES} to Π_{TES} ratios in the range of 0.75 to 1.05 for Π = [50:200].

5.3. Impact on storage performance

A major requirement for the process integration of STES units is the constant power output during discharging. Since counterflow regenerator storage experiences an inevitable drop in discharge power, many authors propose a bypass operation to sustain the outlet temperature at the mixing point for the entire discharging period [15,20]. In this case, the coefficient of uniformity is limited to ξ = 1, which leads to the mixing temperature $T'_{f,out,mix} < T_{f,in}$ due to irreversible losses during the cyclic operation. Conversely, integrating PtH with Φ > 0 results in higher storage temperature that hypothetically leads to higher outlet and mixing temperature $T'_{f,out,mix} > T_{f,in}$ compared to the case without an EFH. Therefore, further investigation focuses on the effects of the PtH integration on the discharging performance by evaluating the coefficient of uniformity and the achieved averaged outlet temperature $\overline{T}'_{f,out}$. For this purpose, simulation studies are performed with target values for the outlet temperature drop at a given thermodynamic efficiency of 90%. The permissible outlet temperature drop $\Delta T_{f,drop}$ at the end of the discharging period is specified with 10%, 20% and 30% related to the inlet temperature $T_{f,in} = 1$. The additional specification of the thermodynamic efficiency is needed to limit the heat source number Φ (otherwise, arbitrarily high coefficients of uniformity might be achieved). Thus, the

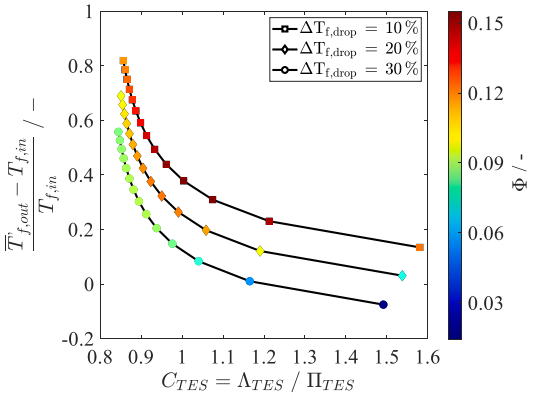

Fig. 8. Nominal temperature raise of the averaged outlet temperature $T'_{f,out}$ during discharging for $\eta_{EH\text{-}STES} = 90\%$, $\Delta T'_{f,drop} = 10\text{–}30\%$ and $\Lambda_{EFH}/\Lambda = 0.10$

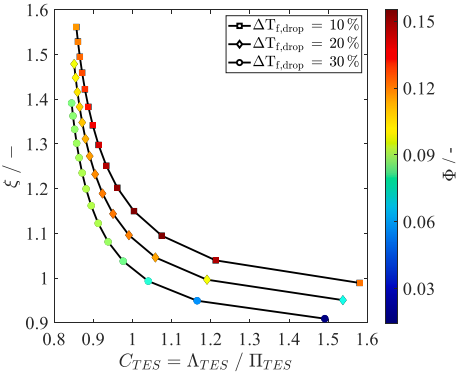

Fig. 9. Coefficient of uniformity as a function of C_{TES} and Φ for $\eta_{EH\text{-}STES} = 90\%$, $\Delta T'_{f,drop} = 10\text{–}30\%$ and $\Lambda_{EFH}/\Lambda = 0.10$.

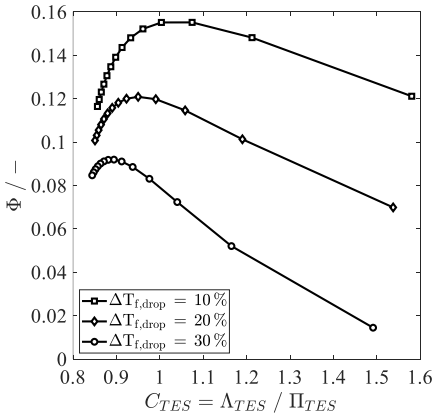

Fig. 10. Dimensionless heat source number as a function of C_{TES} for $\eta_{EH\text{-}STES} = 90\%$, $\Delta T'_{f,drop} = 10\text{–}30\%$ and $\Lambda_{EFH}/\Lambda = 0.10$

parameters Λ and Φ are iteratively calculated varying Π = [20:150] for the given temperature drop and thermodynamic efficiency at a heating area $\Lambda_{EFH}/\Lambda = 0.10$.

The results presented in Figs. 8 and 9 illustrate the increased performance and flexibility through the PtH integration. A significantly higher power output caused by the higher averaged temperature $\overline{T}'_{f,out}$ (Fig. 8) is achieved. In addition, values for the coefficient of uniformity with $\xi > 1$ (Fig. 9) are obtained, indicating the potential for a beneficial bypass operation. Design solutions ranging in $0.85 < C_{TES} < 1.60$ for $0 < \Phi \leq 0.15$ are feasible to ensure 90% efficiency at the given temperature drop. Considering Eq. (23), this flexibility could be used for cost savings by decreasing components' size due to the increased gravimetric energy density.

Furthermore, Fig. 9 shows that high heat source numbers are either achieved for small temperature drops and a constant reservoir size or for small reservoir sizes and a constant outlet temperature drop. Since short thermal reservoirs generally suffer from a high outlet temperature drop, the EFH compensates with a high heat source number to achieve the targeted value, for instance $\Delta T_{f,drop} = 20\%$. Moreover, this compensation effect increases as the permissible temperature drop decreases, resulting in a high heat source number. Fig. 10 additionally illustrates that the heating source does not continuously rise with falling C_{TES} values. The curve profiles indicate two feasible STES design configurations with the same heat source number for any given temperature drop: one configuration with a small Λ_{TES} to Π_{TES} ratio < 1.0 and another with a high ratio > 1.0. According to Eq. (11), small reservoirs with a small heating volume V_{EFH} are heated by a high Joule heat power to compensate for the less efficient heat transfer due to the small surface area to volume ratio a_v and vice versa.

Altogether, the PtH integration increases the storage performance and flexibility since a higher power output together with a higher coefficient of uniformity is achieved without decreasing the thermodynamic efficiency. Moreover, high heat source numbers up to Φ = 0.15 allow for compact EH-STES design configurations ($0.85 < C_{TES} < 1.0$) with a high output power and thermodynamic efficiency at 90%.

6. Conclusions

A transient thermodynamic model is developed for the electrically heated solid media based thermal energy storage (EH-STES) to identify high performing and energy-efficient design solutions with a high thermal storage capacity. The compact and dimensionless modeling approach enables the characterization of such a hybrid storage system by introducing characteristic parameters such as the dimensionless heat source number Φ, the dimensionless storage length Λ and the period duration Π. Based on these parameters, the key performance indicators (KPIs) of energy density, storage utilization ratio, coefficient of uniformity and thermodynamic efficiency are derived to evaluate the improvement in thermal storage capacity and performance due to the power-to-heat integration.

Simulation studies varying the characteristic parameters are conducted to identify general design solutions with high values for the defined KPIs. The results for thermodynamic efficiency and energy density indicate that integrating a small and powerful electrical fluid heater at the hot end of the thermal reservoir is beneficial in terms of energetic and exergetic efficiency. In contrast to an operation without a power-to-heat extension ($\Phi = 0$) where either a high efficiency or a high energy density is achieved, the operation with heat source numbers $\Phi > 0.10$ in large thermal reservoirs ($\Lambda_{TES}/\Pi_{TES} > 1.0$) allows for the first time high values for both the efficiency and energy density. The comparison with the reference case ($\Phi = 0$) reveals an increase of 60% for the energy density at efficiencies above 0.90. These results are obtained together with maximum storage utilization ratios ($\zeta_{max} = 3.65\,\Phi + 1.0$), which convey a significant improvement in thermal storage capacity for $\Phi > 0$.

Another major conclusion related to generalized storage design is that EH-STES design configurations close to $\Lambda_{TES}/\Pi_{TES} \cong 1.0$ and heated with heat source numbers $\Phi < 0.15$ result in a high thermal storage capacity along with a high discharging performance at efficiencies above 0.90. To meet demands for a higher thermal storage capacity, the heat source number could be increased to $\Phi \gg 0.15$, albeit with increasing efficiency losses.

CRediT authorship contribution statement

Sergej Belik: Conceptualization, Methodology, Software, Data curation, Investigation, Writing-Original draft, Visualization. **Volker Dreissigacker**: Investigation, Writing- Reviewing and Editing. **Stefan Zunft**: Writing-Reviewing and Editing, Supervision.

Declaration of competing interest

The authors declare that they have no known competing financial interests or personal relationships that could have appeared to influence the work reported in this paper.

Appendix A

Fig. A1 shows the comparison between the calculated temperature profiles from the dimensionless modeling approach presented in chapter 2 (Eqs. (3a) and (4a)) and the continuous solid phase model introduced by Ismail et al. [16] for the STES unit. Both models are discretized in four hundred compartments for the reduced regenerator length $\Lambda = 100$ ($\Lambda_{EFH} = 0$). For the detailed model from [16], a storage tank with a length and diameter of 10 m each is chosen. In addition, the STES-mat1 material from Table 1 with a thermal conductivity of 3.0 W m^{-1} K^{-1}, a void fraction of 40% and a particle diameter of 44.25 mm is assumed for the packed bed. Furthermore, the charging and discharging period is varied from 3.37 h to 6.0 h to modify Π and thus C_{TES} from 1.60 to 0.90. The results for the fluid temperature show a good agreement with the detailed model from [16]. The largest deviation of up to 5% occurs for $C_{TES} = 1.60$ due to the greater influence of heat conduction in large storage tanks, which is neglected in the proposed model.

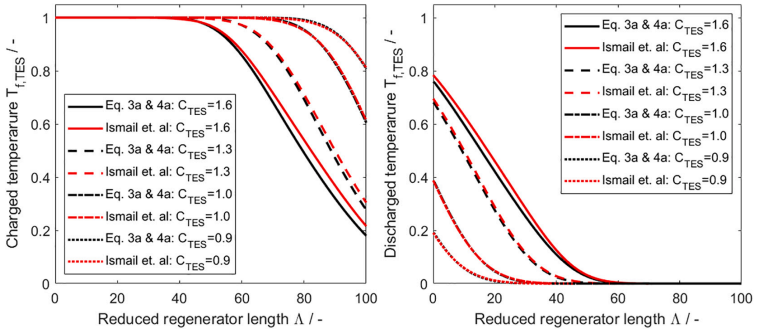

Fig. A1. Normalized fluid temperature profiles under cyclic operation at the last time step of respective charging and discharging for $\Lambda = 100$ and different C_{TES} used in the study from chapter 5 ($\Gamma_{TES} = 0$ and $\Lambda_{EFH} = 0$).

References

[1] Franz Trieb, André Thess, Storage plants–a solution to the residual load challenge of the power sector? J. Energy Storage 31 (2020) https://doi.org/10.1016/j.est.2020.101626.

[2] C.-P. Bartsch, tructural change and plant repurposing in the Rhenish lignite mining area, RWE, Presentation given at 6th working group meeting of "Platform for coal regions in transition". https://ec.europa.eu/energy/sites/ener/files/documents/5.3._master_coal_plant_repurposing.pdf, 2021. (Accessed 16 April 2021).

[3] MAN, Energy Storage. "Electro-thermal energy storage". https://www.man-es.com/energy-storage/solutions/energy-storage/electro-thermal-energy-storage, 2021. (Accessed 16 April 2021).

[4] Alberto Benato, Anna Stoppato, Energy and cost analysis of a new packed bed pumped thermal electricity storage unit, J. Energy Resour. Technol. 140 (2) (2018), https://doi.org/10.1115/1.4038197.

[5] Daniel C. Stack, Daniel Curtis, Charles Forsberg, Performance of firebrick resistance-heated energy storage for industrial heat applications and round-trip electricity storage, Appl. Energy 242 (2019) 782–796, https://doi.org/10.1016/j.apenergy.2019.03.100.
[6] Philipp Vinnemeier, et al., Integration of heat pumps into thermal plants for creation of large-scale electricity storage capacities, Appl. Energy 184 (2016) 506–522, https://doi.org/10.1016/j.apenergy.2016.10.045.
[7] Charles W. Forsberg, et al., Converting excess low-price electricity into high-temperature stored heat for industry and high-value electricity production, Electr. J. 30 (6) (2017) 42–52, https://doi.org/10.1016/j.tej.2017.06.009.
[8] Schniewindt, Flow Heaters, 2021. https://www.schniewindt.de/en/csn-flow-heaters/. (Accessed 15 April 2021).
[9] Ohmex, Electrical Process Flow Heaters datasheet, in: https://www.ohmex.de/en/wp-content/uploads/sites/3/2020/03/electric-process-heater_STR_2020-03.pdf, 2021. (Accessed 15 April 2021).
[10] Kanthal®, Resistance heating alloys and systems for industrial furnaces. https://www.kanthal.com/globalassets/kanthal-global/downloads/materials-in-wire-and-strip-form/resistance-heating-wire-and-strip/home-appliance_s-ka026-b-eng_lr.pdf, 2021. (Accessed 1 May 2021).
[11] Markus Hänchen, Sarah Brückner, Aldo Steinfeld, High-temperature thermal storage using a packed bed of rocks–heat transfer analysis and experimental validation, Appl. Therm. Eng. 31 (10) (2011) 1798–1806, https://doi.org/10.1016/j.applthermaleng.2010.10.034.
[12] H. Hausen, Wärmeübertragung im Gegenstrom, Gleichstrom und Kreuzstrom, Springer, Berlin, Heidelberg, 1976.
[13] T.E.W. Schumann, Heat transfer: a liquid flowing through a porous prism, J. Frankl. Inst. 208 (1929) 405–416.
[14] F.W. Schmidt, A.J. Willmott, Thermal Energy Storage and Regeneration, Hemisphere Press, 1981.
[15] Ryan Anderson, et al., Packed bed thermal energy storage: a simplified experimentally validated model, J. Energy Storage 4 (2015) 14–23, https://doi.org/10.1016/j.est.2015.08.007.
[16] K.A.R. Ismail, R. Stuginsky Jr., A parametric study on possible fixed bed models for pcm and sensible heat storage, Appl. Therm. Eng. 19 (7) (1999) 757–788, https://doi.org/10.1016/S1359-4311(98)00081-7.
[17] Anton Meier, Christian Winkler, Daniel Wuillemin, Experiment for modelling high temperature rock bed storage, Solar Energy Mater. 24 (1-4) (1991) 255–264, https://doi.org/10.1016/0165-1633(91)90066-T.
[18] Ryan Anderson, et al., Experimental results and modeling of energy storage and recovery in a packed bed of alumina particles, Appl. Energy 119 (2014) 521–529, https://doi.org/10.1016/j.apenergy.2014.01.030.
[19] Harmeet Singh, R.P. Saini, J.S. Saini, A review on packed bed solar energy storage systems, Renew. Sustain. Energy Rev. 14 (3) (2010) 1059–1069, https://doi.org/10.1016/j.rser.2009.10.022.
[20] Thibaut Esence, et al., A review on experience feedback and numerical modeling of packed-bed thermal energy storage systems, Solar Energy 153 (2017) 628–654, https://doi.org/10.1016/j.solener.2017.03.032.
[21] Syed M. Zubair, Meamer El-Nakla, Shahzada Z. Shuja, Thermoeconomic design and analysis of a sensible-heat thermal energy storage system with Joulean heating of the storage element, Exergy Int. J. 2 (4) (2002) 237–247, https://doi.org/10.1016/S1164-0235(02)00074-2.
[22] Volker Dreißigacker, Sergej Belik, System configurations and operational concepts for highly efficient utilization of power-to-heat in A-CAES, Appl. Sci. 9 (7) (2019) 1317, https://doi.org/10.3390/app9071317.
[23] Sammy Houssainy, et al., Thermodynamic analysis of a high temperature hybrid compressed air energy storage (HTH-CAES) system, Renew. Energy 115 (2018) 1043–1054, https://doi.org/10.1016/j.renene.2017.09.038.

2.4 Paper III (macro scale): Verification of the main hypothesis through techno-economic system analysis

Sergej Belik

The following research paper was published in
Journal of Energy Storage
Volume 68, September 2023, 107416
https://doi.org/10.1016/j.est.2023.107416

Contribution roles
Sergej Belik:
Research work - Conceptualization, methodology, software and model development, investigation, formal analysis and data curation
Writing - Conceptualization, original draft preparation, review, editing and visualization

Stefan Zunft:
Reviewing and supervision

Journal of Energy Storage 68 (2023) 107416

Contents lists available at ScienceDirect

Journal of Energy Storage

journal homepage: www.elsevier.com/locate/est

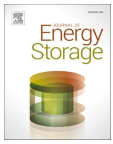

Research papers

Techno-economic evaluation of a Brayton battery configuration with power-to-heat extension

Sergej Belik

Institute of Engineering Thermodynamics, German Aerospace Center (DLR), Stuttgart, Germany

ARTICLE INFO

Keywords:
Joule-Brayton PTES
Brayton Carnot battery
Techno-economic analysis
Power-toheat
Induction air heater

ABSTRACT

The development of cost-efficient, environmentally friendly, and reliable technologies for utility-scale electricity storage is a key element for future flexible power systems. Brayton cycle-based Pumped Thermal Energy Storage (PTES) offers the potential of making a substantial progress to reach this goal. For further improvements in cost efficiency and flexibility we investigate the additional integration of Power-to-Heat (PtH) into the heat pump cycle. This integration allows a reduction in component size due to higher energy density; however, it also leads to efficiency losses. The objective of this paper is to quantify this tradeoff between round-trip efficiency and cost efficiency for closed-cycle Joule-Brayton PTES configurations and to provide design solutions for the novel PtH component. To this end, a wide-range design study with variable electric heating power and component efficiencies is conducted. In addition to the thermodynamic analysis, an economic assessment is presented, which clarifies the benefits of PtH extension. The results demonstrate a significant reduction of capital expenditures by up to 23 % along with higher system flexibility and a loss in round-trip efficiency of up to 5 %.

1. Introduction

The ongoing transformation of electrical energy systems from conventional to renewable energy supplies increases the need for energy storage technologies [1]. Large-scale electrical energy storage (EES) supports the integration of fluctuating renewable energy sources, which allows for a more reliable and flexible supply of low-carbon and zero-carbon electricity generation. However, EES technologies typically have significant drawbacks, such as capital costs, round-trip efficiency, cycle stability and locational dependency. To reduce these constraints, various technologies have been developed.

1.1. Established electric energy storage technologies

Pumped hydro energy storage (PHES) and diabatic compressed air energy storage (D-CAES) are established, large-scale EES technologies providing gigawatt hours of energy storage capacity for grid-scale peak leveling applications.

PHES is the most mature EES and benefits from high output power of 1.0–1.50 GW and high round-trip efficiency (RTE) in the range of 70 %–80 % but suffers from locational dependency and high capital costs of 600–2000 $/kW [2,3].

D-CAES technology is derived from a temporally decoupled multi-stage Brayton cycle in which air is compressed in an underground cavern during charging and mixed with natural gas for combustion in a modified gas turbine during the delivery period. Existing diabatic plant configurations operating in Huntorf (Germany) and McIntosh (USA) output 321 MW and 110 MW with an RTE of 42 % and 54 %, respectively [5]. The capital costs estimated for this storage technology range from 400 to 800 $/kW [4,5]. In addition to the required geographical morphology, a major drawback of D-CAES technology is the low RTE accompanying the use of fossil fuels.

1.2. Adiabatic electric energy storage

Alternative thermo-mechanical EES technologies are currently being developed, namely, adiabatic CAES (A-CAES) and Carnot batteries (CB). Carnot batteries can be categorized into pumped thermal energy storage (PTES) and adiabatic liquid air energy storage (A-LAES). These storage technologies are adiabatic due to the integration of thermal energy storage (TES) following the polytropic compression process. The references [6–8] give a comprehensive overview of CB, while de Sisternes et al. [9] and Xue [10] show the state of the art of A-CAES and A-LAES. In addition, Benato et al. [5] focussed their study on PTES, which categorizes Rankine cycle-based (Rankine Carnot battery) and inverse Brayton cycle-based (Brayton Carnot battery) CBs. The essential

E-mail address: Sergej.Belik@dlr.de.

https://doi.org/10.1016/j.est.2023.107416
Received 30 June 2022; Received in revised form 4 April 2023; Accepted 10 April 2023

Table 1
Comparison of large-scale adiabatic EES [10–29].

Adiabatic EES	A-CAES (TRL 5–6)	A-LAES (TRL 7–9)	Brayton-PTES[a]	Rankine-PTES[b]
Storage capacity [MWh]	1–1000	10–1000	1–1000	20–600
Power rating [MW]	0.5–90	0.35–100	0.5–150	1–100
Round-trip efficiency [%]	60–75	45–65	45–67	25–64
Volumetric energy density [kWh/m^3]	0.5–20	50–80	20–70 (430)	10–22
CAPEX [$_{2021}/kWh]	150–316	250–640	100–400	250–400
Lifetime [a]	20–40	20–40	25–30	25–30
Locational-dependency	Yes	No	No	No

[a] HT-regenerator based system using air as WF (TRL 2–5) [21,23].
[b] Transcritcal Rankine PTES using CO_2 as WF (TRL 2–4) [13–16].

performance characteristics of these adiabatic EES are summarized in Table 1.

A-CAES and A-LAES use TES to store compression heat during the charging period and transfer it during the delivery period to the heat engine process in a modified gas turbine. In contrast to D-CAES, the addition of TES results in a higher RTE in a range from 60 % to 75 % [11] and, as no additional fossil fuel is used, it operates without CO_2 emissions. The main benefit of A-LAES is the high energy density due to the low volume of liquefied air. Major drawbacks are the high capital expenditures (CAPEX) for A-LAES and geographical constraints for the air storage (aquifers and salt caverns) in the case of A-CAES [11,12].

Nomenclature

a_v	specific surface area (m^{-1})
c_p	specific heat capacity (J kg^{-1} K^{-1})
H_0	magnetic field strength (A m^{-1})
H	total length (m)
k	heat transfer coefficient (W m^{-2} K^{-1})
m	storage mass (kg)
$\dot{m}_f$	mass flow rate (kg s^{-1})
P_{el}	electrical power input (W)
$\dot{Q}_{PtH}$	Joule heat induced by electrical heating (W)
$\dot{q}_{PtH}$	Joule heat power density (W m^{-3})
St	Stanton number
t	time scale (s)
T	temperature (K)
V	volume (m^3)
w_f	free flow velocity (m s^{-1})
w_t	specific technical work (J kg^{-1})
z	length scale (m)

Greek letters

β	compression ratio (−)
ε	void fraction (−)
κ	fluid's isentropic exponent (−)
η_{PtH}	electric heating efficiency, $\dot{Q}_{PtH}/P_{el}$
λ	thermal conductivity (W m^{-1} K^{-1})
ρ	density (kg m^{-3})
τ	duration of charging/discharging period (s)
μ_0	magnetic field constant $4\pi 10^{-7}$(N A^{-2})
Γ	dimensionless heater loss number (−)
Λ	dimensionless heater length (−)
Π	dimensionless heater period duration (−)
Φ	dimensionless heat source number (−)
Ψ	thermal compression ratio (−)
$\dot{X}$	dimensionless exergy rate: $\dot{X}_{EFH} = \Phi\Lambda(1-\epsilon)$

Acronyms

A/D-CAES	a/diabatic compressed air energy storage
A-LAES	adiabatic liquid air energy storage
CAPEX	capital expenditures (€)
CB	Carnot battery
EES	electrical energy storage
EFH	electric flow heater
HE/HP	heat engine/heat pump (cycle)
HT/LT	high-temperature/low-temperature
HX	heat exchanger
PTES	pumped thermal energy storage
PtH	power-to-heat
RTE	round-trip efficiency
STES	solid media thermal energy storage
ETES	electrically heated thermal energy storage
TM	turbomachinery
WF	working fluid

Subscripts and superscripts

in/out	inlet/outlet
S/F	solid phase/fluid phase
p/poly	polytropic process
is	isentropic process
$'$	related to charging period (HP cycle)
$''$	related to discharging period (HE cycle)
$\bar{x}$	averaged quantity x
x^*	normalized quantity x

The Rankine Carnot battery uses various working fluids in dependence with the thermodynamic cycle. Transcritical Rankine battery uses CO_2, subcritical Rankine battery uses water, synthetic or organic fluids. In addition to the HCES concepts, Steinmann introduced Power to Heat to Power (PHP) concepts employing an ETES unit, which is heated completely by Joule heating in order to power the coupled Clausius Rankine cycle (CRC) or Organic Rankine cycle (ORC), for instance.

The Rankine Carnot battery, i.e. a Rankine PTES, uses a phase change working fluid (WF) to run the heat pump (HP) and the heat engine (HE) cycles. Rankine PTESs are categorized into transcritical and subcritical cycles according to their WF type. Transcritical Rankine battery uses CO_2 [13,14], subcritical Rankine battery uses water (steam) [15] or organic fluids as WF. During charging the WF evaporates receiving the heat from the low-temperature (LT) reservoir. This gaseous WF compresses afterwards by the vapour compressor to high temperatures and pressures, accounting storage temperature of 123 °C at 140 bar maximal pressure for the transcritical CO_2 cycle [14] and 365 °C at 105 bar for subcritical steam Rankine cycle [15]. Then, the WF condensates releasing the latent heat to the high-temperature (HT) TES before it finally expands to the initial state. During discharging, the thermal energy stored inside the HT-TES is used to evaporate the pressurized WF that later expands in a turbine to deliver technical work. Finally, the WF condensates releasing the heat to the LT-TES.

Another option for the Rankine Carnot battery system is the implementation of an electrically heated TES (ETES) [16] instead of the usually expensive heat pump for charging the HT-TES. This CB system has recently received attention for the purpose of retrofitting existing coal-fired power plants into EES [17]. Here, the electrically charged high-temperature heat of a sensible TES can be dispatched through the Rankine steam cycle. A resistive heater generates the HT heat for the sensible molten salt TES with a maximum storage temperature of 560 °C [17].

The Brayton Carnot battery, i.e. a Brayton PTES has a similar working principle compared to the Rankine Carnot battery. In contrast to the phase change WF from Rankine CB systems, it employs a gaseous WF that is usually argon or air [5]. Here, the thermal energy is converted

from electricity in a high-temperature HP cycle and stored inside two TESs, comprising a low- temperature and a high-temperature pressure vessel. The stored thermal energy is then reconverted into electrical energy using a gas turbine cycle. The residual heat from the gas turbine is stored in the low-temperature TES tank for feeding back into the Brayton HP cycle. Given this layout, the Brayton CB contains two thermal tanks and four turbomachines (two compressors and two expanders). Desrues et al. [23] first performed system simulations based on the Brayton cycle with a energy storage capacity of 602.6 MWh and a round-trip efficiency of 66.7 %. In comparison to other EES technologies, Brayton PTES benefits from its high energy density and low CAPEX. Additionally, this EES has no geographical constraints [5,6].

From an economic standpoint, the current revenue options from energy arbitrage and frequency regulation are still too low to cover the high capital costs [11]. Therefore, cost efficiency and system flexibility need to be improved. One promising option for cost reduction alongside with gains in performance and flexibility is the implementation of an additional electric heating component downstream of the HP compressor [12].

1.3. Power-to-heat integration in A-CAES and Brayton CB

Adding a high-performance Power-to-Heat (PtH) unit into the heat pump cycle increases the thermal energy density of the system [18,19,21] that can be used to reduce the pressure ratio of turbomachines (TM) and hence to minimize their size. This allows for a lower pressure setting for the high-pressure stage while maintaining a high system temperature. Moreover, component size of TESs and heat exchangers can be minimized which consequently lowers their equipment costs without affecting system's power output [20,24]. The main drawback of PtH integration is the reduction in round-trip efficiency (RTE) caused by the lower coefficient of performance (COP) during charging on the one hand, and the limited Carnot efficiency of the gas turbine cycle on the other hand [19–21].

Several research efforts have been carried out to investigate A-CAES and Brayton CB configuration concepts with additional PtH integration in terms of energy efficiency, cost efficiency and flexibility. For application in A-CAES, Dreissigacker et al. [19] found that the integration of PtH in the low-pressure stage upstream of the TES is associated with the least efficiency losses while Houssainy et al. [20] clearly showed the increase in storage density with a resulting decrease in system costs and efficiency through an ETES implementation in the high-pressure stage. Central results reveal major CAPEX reduction from 200 $/kWh at 57.5 % RTE to 65 $/kWh at 24.5 % RTE.

For the application in Brayton CB, Benato [18] and Chen et al. [21] proposed the integration of an electric heater between the HP compressor and HT-TES, as proposed in Fig. 1, with the aim of

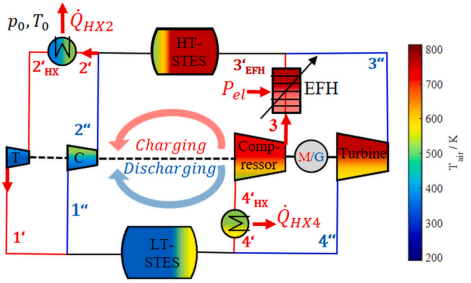

Fig. 1. Schematic of Brayton battery configuration with an electric flow heater (EFH); illustrated operation state is at the end of the charging period.

decoupling the compressor pressure from its outlet temperature. In doing so, Benato intended to reduce the costs of the HP compressor by limiting its capability. Therefore, the author limited the HP compressor pressure ratio to 6, thereby reducing its outlet temperature to 550 °C and raising the HT-TES inlet temperature up to 1050 °C using the electric heater. At this maximum storage temperature, Benato's techno-economic assessment for a TES build-up with Al_2O_3 brick indicates an energy density increase of 105 % to 430 kWh/m^3, a CAPEX reduction of 35 % to 54 $/kWh, and an unexpected upgrade of the RTE from 6.3 % to 7.0 %. While efficiency is expected to fall with reduced system costs, low-cost turbomachines with a poor isentropic efficiency of 0.80 dominate the enormous drop in RTE below 10 % [23,25] and the overall system costs [26,29]. Therefore, a temperature rise within the HE cycle might improve the RTE and reduce costs at such a low-efficiency level. Chen et al. [21] presented a similar system configuration and proposed to utilize the excess heat with a bottoming organic Rankine cycle (ORC). Since the excess heat temperature ranges from 550 K to 750 K, its exergy can be suitably dispatched through the ORC, improving the system's RTE to 47.1 %. Although this RTE is 5.89 % lower compared to the operation without an additional electric heater, the energy density is more than doubled to 62.2 kWh/m^3. In summary, all these studies show the effects of additional PtH integration into the thermo-mechanical and adiabatic EES, wherein energy density increases significantly and results in cost reduction accompanied by a slight loss in RTE.

1.4. Review of calculation methods

In the reviewed literature [18–21], the authors used similar methods for modeling the system and each component. Table 2 summarizes these approaches.

Different model complexities are implemented for component modeling depending on their individual characteristics. In all of the reviewed sources, turbomachinery and HX are modeled as stationary components. For the turbomachines, the isentropic state change is used to determine the outlet temperature. For the HX, practical NTU formulations [30,31] are applied to determine its size. In contrast, the modeling of the TES and the electric heater has a different complexity. While Houssainy et al. [20] model the HT-TES together with the heater as a lumped capacity, assuming a constant temperature during discharging, Dreissigacker et al. [19] and Chen et al. [21] take into account the typical drop in outlet temperature for the regenerator-based HT-TES using a one-dimensional and two-phase thermal model for their design study. However, in both studies, as well as in [18], the electric heater is ideally considered a punctiform heat source inside the system, providing only the required energy demand for a given temperature increase of the WF. Benato [18] uses a one-dimensional thermal model from [32] to design the TES unit. In accordance with [20,21], the author also assumes an ideal electric heater as a punctiform heat source without giving any details about its shape and dimension.

The system model connects the component models at the appropriate intersections for both the HP and HE cycles, and iterates until achieving cyclic equilibrium for HP and HE temperatures. Since WF properties change at each iteration and in each cycle point with its temperature, the implementation of a material property database at the system level is necessary. Therefore, Benato [18], Dreissigacker et al. [19], and

Table 2
Comparison between modeling approaches from reviewed literature (model dimensions and phases S:solid and F:fluid).

References	WF property database	TM	HX	TES	EFH
[18]	CoolProp	0d, ad.	NTU	1d; F	0d (fluid)
[19]	CoolProp	0d, ad.	NTU	1d; S/F	0d (fluid)
[20]	calorically perfect gas	0d, ad.	NTU	0d	0d (fluid)
[21]	REFPROP	0d, ad.	NTU	1d; S/F	0d (fluid)
This study	CoolProp	0d, ad.	NTU-ε	1d; S/F	1d (S/F)

McTigue et al. [29] used the CoolProp database [27], while Chen et al. [21] implemented the REFPROP [28] database into the system-level simulation to calculate the temperature-dependant thermal properties of a real WF gas. Furthermore, Houssainy et al. [20] use formulations for mass and energy balance in combination with calorically perfect gas equations of state.

1.5. Contributions

In literature [18–21], the authors have carried out a technical evaluation and demonstrated the increase in energy density along with the decrease of component size through the implementation of a high-temperature EFH component into the adiabatic EES system. However, the EFH component is simply specified according to a given temperature rise [18,21] or a required energy demand [19,20]. As such, the shape and dimension of the component cannot be determined. Apart from Dreissigacker et al. [19], the authors further specify high-temperature requirements for the EFH without providing technical solutions: while an outlet temperature around 420–450 °C [19] is feasible for a two-stage A-CAES with available EFH technology, the Brayton CB requires considerably higher temperatures of up to 1050 °C [18] or even more (1400 K) [21] with a lack of technical EFH solutions. Despite the mentioned lack of solutions, Benato [18] conducted a techno-economic evaluation that puts the cost of the EFH at $C_{\mathrm{EFH}} = 75000 \cdot P_{EFH}^{0.9}\ \$/MW$. Furthermore, as mentioned in Section 1.3, the author demonstrates a cost reduction along with a slight improvement in RTE to 7.0 %, where a tradeoff is normally expected. Therefore, the main objective of the present paper is to quantify this tradeoff between system costs and its efficiency that arises from the additional integration of PtH. The main hypothesis is that PtH offers a significant cost leverage when a compact EFH component is added downstream of the HP compressor. Another objective is to present a novel design solution for the EFH that meets the application-specific requirements of a Brayton CB. These essentially include a high cost and energy efficiency of over 85 % at an outlet temperature above the maximum compressor temperature of 550 °C [18].

The following contributions of this study are derived from above considerations:

- Provision of an efficient Brayton CB model employing component costs and real gas behavior for the WF
- Techno-economic system analysis quantifying the impact of the additional EFH on costs and efficiency
- Design study providing a design solution for the EFH component

To address these contributions, Section 2 first introduces a simplified modeling approach for a closed-cycle Brayton CB configuration with a PtH extension. Sections 3 and 4 describe the component models and the setup for system simulation. Results for wide-range parameter and design studies with increased PtH heating rates are presented in Section 5. In addition to the thermodynamic analysis, we conduct an economic assessment of these advanced Brayton CB configurations to demonstrate the effect of cost reduction through the PtH extension. Finally, Section 6 presents our study conclusions.

2. System description and thermodynamic cycle analysis

2.1. Brayton Carnot battery with extended electric flow heater

The closed-loop system configuration from Fig. 1 without an electric heater component has been studied in various theoretical works [10,33–37] where air has been used as WF. This system consists of one compressor and turbine pair for charging and another for the discharging period, two solid media thermal energy storage (STES) systems integrated in between the turbomachines, and two heat exchangers (HX). In addition, a motor and generator with associated clutches are needed to convert the electrical energy into mechanical energy and vice versa for the respective adiabatic compression and expansion processes.

In order to increase system energy density and cost efficiency, the electric flow heater (EFH) employed in [18] is integrated in the process scheme from Fig. 1 in the same manner. The red area in the associated temperature-entropy diagram from Fig. 2 illustrates the additional high-temperature heat given to the system. The integration downstream of the HP compressor has two technical reasons. First, the application of the EFH lowers the temperature requirements for the HP compressor, which has a maximum outlet temperature of 550 °C. Second, the isobaric heating process of a pressurized gas (states $3' \rightarrow 3'_{\mathrm{EFH}}$ in Fig. 2) generates a lower entropy rate compared to the isobaric heating at lower gas pressures. This makes the heating process more efficient from a Second Law perspective. Therefore, the combination of compression heat ($4'_{\mathrm{HX}} \rightarrow 3'$) from the heat pump cycle and HT heat from the EFH ($3' \rightarrow 3'_{\mathrm{EFH}}$) is a feasible and exergetically efficient solution for generating HT heat for the Brayton heat engine cycle.

Two PtH technologies are worth considering for the EFH due to the high-power density and high efficiency required for the heating process: resistance heating and induction heating. Both operate on the principle of the Joule effect and provide high temperatures above 500 °C, which are required to efficiently run the closed-loop Brayton heat engine cycle. However, EFHs based on commercially available resistance heating elements are limited to outlet temperatures of 600 to 700 °C due to the limited heat transfer area of the tubular heating elements [38,39]. To reach higher outlet temperatures, we propose a PtH concept that consists of an inductively heated and fluidized pebble bed [40]. In contrast to tubular heating elements, the pebble bed provides a 50 % larger specific heat transfer area, which makes the convective heat transport of the inductively generated heat more efficient. Moreover, the contactless electric power transmission allows temperatures above 900 °C inside the pebble bed without being limited by electrical contacts. Therefore, we prefer to use the induction air heater that is based on a pebble bed concept for generating high-temperature heat for Brayton CB application.

To take advantage of the high-temperature potential of the induction air heater, we propose the combination with a counterflow regenerator STES [22]. The high-temperature and low-temperature STES

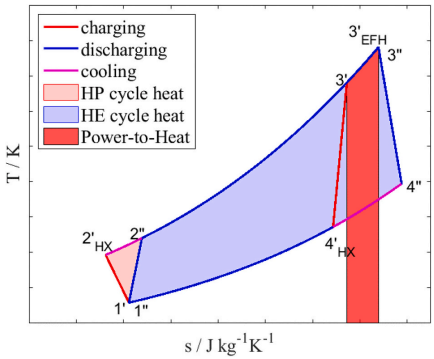

Fig. 2. T-s-diagram of Brayton heat pump (charging) and heat engine (discharging) cycles with electrical heat input (red area: $3' \rightarrow 3'_{\mathrm{EFH}}$) and applied turbomachines' polytropic efficiency of $\eta_{\mathrm{p}} = 0.90$. (For interpretation of the references to color in this figure, the reader is referred to the web version of this article.)

regenerators are comprised of thermally insulated pressure vessels with a ceramic honeycomb inventory. The honeycomb inventory concept allows maximum operating temperatures of up to 1200 °C [32]. The direct contact heat transfer between the WF air and the honeycomb inventory leads to an efficient heat transport provided by the large heat transfer area. Additionally, the large diameter of the storage tanks results in low air velocities, which lead to low-pressure losses.

The HXs used in the study are common counterflow shell-and-tube type HXs that use water as a coolant. These are installed downstream of each STES and are operated only during the charging period to take advantage of the low-cost electricity running the water pumps.

2.2. Thermodynamic cycle analysis

The thermodynamic analysis aims at discussing the impact of PtH integration on the performance of the Brayton CB configuration from Fig. 1. To derive a general conclusion on the storage systems' performance, we chose the discharged specific technical work $w_{\{t,HE\}}$ of the Brayton HE cycle (blue area in Fig. 2: $1'' \rightarrow 2'' \rightarrow 3'' \rightarrow 4'' \rightarrow 1''$) as the key performance metric. Assuming ideal gas behavior of the working fluid and an adiabatic system with a reversible heat transport inside the STES and HX components, only the turbomachine irreversibility needs to be considered. Based on these assumptions, we apply polytropic process equations to the HP (notation ′) and HE cycles (notation ″) of Fig. 2. using the thermal compression ratio Ψ and the polytropic efficiency η_p to calculate the outlet temperature of turbomachinery:

$$T_{1'} = T_{2',HX} \cdot \Psi_{turb}^{-\eta_{p,turb}} \text{ and } T_{1''} = T_{1'} \tag{1}$$

$$T_{2''} = T_{1''} \cdot \Psi_{comp}^{\frac{1}{\eta_{p,comp}}} \tag{2}$$

$$T_{3'} = T_{4',HX} \cdot \Psi_{comp}^{\frac{1}{\eta_{p,comp}}} \tag{3}$$

$$T_{4''} = T_{3''} \cdot \Psi_{turb}^{-\eta_{p,turb}} \text{ and } T_{3',EFH} = T_{3''} \tag{4}$$

The EFH outlet temperature $T_{3',EFH}$ may be expressed using the dimensionless exergy rate $\dot{X}_{EFH}$ for the EFH from Belik et al. [22]:

$$T_{3',EFH} = T_{3'}\left(1 + \dot{X}_{EFH}\right) = T_{3'}\left(1 + \Lambda\Phi(1-\varepsilon)\right) \tag{5}$$

where Λ is the dimensionless heater length, Φ is the dimensionless heat source number, ε is the void fraction of the EFH material [22].

To calculate the discharged specific technical work w_t, the proportional relationship between specific enthalpy and temperature ($\Delta h_{HE} = \bar{c}_p \Delta T_{HE}$) given by the ideal gas law is applied assuming the averaged specific heat capacity of $\bar{c}_p = 1.14\ kJkg^{-1}K^{-1}$ for dry air at HT conditions of the ideal gas:

$$w_t = \bar{c}_p \Delta T_{HE} \tag{6}$$

where ΔT_{HE} is the total temperature difference provided by the HT- and LT-STES to run the Brayton heat engine cycle. Since a reversible heat transport from the storage inventory to the WF is assumed ($\eta_{STES} = 1$), we can express this temperature difference using turbomachine's inlet and outlet temperatures:

$$\Delta T_{HE} = \Delta T_{turb''} - \Delta T_{comp''} = (T_{3''} - T_{4''}) - (T_{2''} - T_{1''}) \tag{7}$$

Substituting Eq. (7) in Eq. (6) with associated temperature definitions from Eqs. (1) to (5) leads to an expression for w_t that is further simplified using the equivalent polytropic efficiency $\eta_p = \eta_{p,turb} = \eta_{p,comp}$ and equivalent thermal compression ratio $\Psi = \Psi_{turb} = \Psi_{comp}$ for the turbomachines:

$$w_t = \frac{\bar{c}_{p,F} \cdot \Psi^{-\eta_p}\left(T_{2',HX}\Psi^{\frac{1}{\eta_p}} + T_{4',HX}(\dot{X}_{EFH}+1) - T_{2',HX}\right)}{\Psi^{\frac{1}{\eta_p}}} + \frac{\bar{c}_{p,F} \cdot T_{4',HX}(\dot{X}_{EFH}+1)}{\Psi^{\frac{1}{\eta_p}}} \tag{8}$$

Eq. (8) might be further specified using the definition $\Psi = \beta^{\frac{\kappa-1}{\kappa}}$ with the pressure ratio β and WF's isentropic exponent κ:

$$w_{t,poly} = \frac{\bar{c}_{p,F} \cdot \left(\beta^{\frac{1-\kappa}{\kappa}}\right)^{\eta_p}\left(T_{2',HX}\left(\beta^{\frac{1-\kappa}{\kappa}}\right)^{\frac{1}{\eta_p}} + T_{4',HX}(\dot{X}_{EFH}+1)\right)}{\left(\beta^{\frac{1-\kappa}{\kappa}}\right)^{\frac{1}{\eta_p}}} - \frac{\bar{c}_{p,F} \cdot T_{2',HX}\left(\beta^{\frac{1-\kappa}{\kappa}}\right)^{\eta_p}}{\left(\beta^{\frac{1-\kappa}{\kappa}}\right)^{\frac{1}{\eta_p}}} + \frac{\bar{c}_{p,F} \cdot T_{4',HX}(\dot{X}_{EFH}+1)}{\left(\beta^{\frac{1-\kappa}{\kappa}}\right)^{\frac{1}{\eta_p}}} \tag{9}$$

For $\eta_p = 1$ and $\dot{X}_{EFH} = 0$, Eqs. (8) and (9) reduce to a simplified expression that describes the isentropic process with ideal gas conditions:

$$w_{t,is} = \bar{c}_{p,F} T_{2',HX}\left(\beta^{\frac{1-\kappa}{\kappa}}\right) + \bar{c}_{p,F}\left(\beta^{\frac{\kappa-1}{\kappa}}\right) T_{4',HX} - 2\,\bar{c}_{p,F} T_{4',HX} + \bar{c}_{p,F}\left(T_{4',HX} - T_{2',HX}\right) \tag{10}$$

Results from Eqs. (9) and (10) for dry air are presented in Fig. A1 from Appendix A for various pressure ratios and HX temperatures using averaged values for the specific heat capacity $\bar{c}_{p,air} = 1.14\ kJ\ kg^{-1}K^{-1}$ and for the isentropic exponent $\kappa = 1.35$. These values have also been used to obtain results from Fig. 3.

The power ratio of the polytropic and isentropic process power output can be calculated using the ratio of the specific technical work from Eqs. (9) and (10) with the associated mass flow rates:

$$\frac{P_{discharge,poly}}{P_{discharge,is}} = \frac{w_{t,poly}\,\dot{m}_{F,poly}}{w_{t,is}\dot{m}_{F,is}} = 1 \tag{11}$$

To analyze the impact of PtH integration we conducted a simulation study based on Eqs. (9) to (11) for WF air using various polytropic efficiencies η_p. The results presented in Fig. 3 confirm that an increasing electrically fed exergy rate $\dot{X}_{EFH}$ leads to a higher specific work output and thus to a lower mass flow rate during discharging. This effect is particularly evident at lower polytropic efficiency. In conclusion, the integration of PtH into the Brayton battery generally results in higher energy density and lower mass flow rates, which can be used to reduce the component size with associated cost reduction.

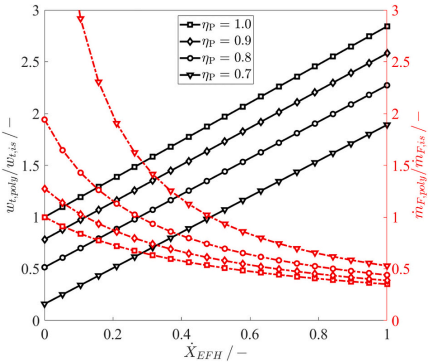

Fig. 3. Specific technical work and mass flow rate ratios for dry air: $\kappa = 1.35$, $\bar{c}_{p,air} = 1.14\ kJ\ kg^{-1}K^{-1}$; $T_{4',HX} = [0:200]°C$; $T_{2',HX} = 20°C$: $\beta = [3:15]$.

3. Modeling

A techno-economic analysis of the Brayton battery concept from Fig. 1 requires the interconnected modeling of the central components. The simulation algorithm is presented in Fig. 5, showing both the system-level and the component-level calculation procedures and the usage of the following governed equations.

In order to perform a detailed calculation on the system and component level, we obtained thermal properties from the CoolProp database [27] for heat capacity, density, thermal conductivity, and viscosity as a function of temperature at each cycle point in Fig. 2. We calculate entropy and enthalpy values in the same manner for the WF dry air, which is composed as a mixture of nitrogen, oxygen, and argon. In addition, water is used for HX as a heat-rejection fluid acquiring thermal properties from [27].

To ensure efficient computation, we used different model complexities on the component level according to component characteristics, as such components can be divided into static and transient. Regenerator-based STES and EFH have a transient behavior that requires detailed, multiple-dimension modeling. In contrast, a HX can be viewed as a stationary component, enabling a compact formula for mass and heat balance. As shown in Table 2, simplified formulations are suitable for modeling turbomachinery for which the isentropic state change is used to determine the outlet temperatures.

3.1. Turbomachines

Eqs. (1) to (4) are used to model compressors and turbines in a simplified fashion. In contrast to the analysis from Section 2.2, real WF properties from [27] are used to determine the isentropic outlet temperatures $T_{F,out,is} = T_{F,in}\,\beta^{\frac{\kappa-1}{\kappa}}$ and enthalpies $h_{out,is}$. The isentropic efficiency η_{is} is then used to calculate the irreversible adiabatic compression outlet enthalpy

$$h_{out,comp} = \frac{h_{out,is} - h_{in}}{\eta_{is,comp}} + h_{in} \tag{12}$$

and the irreversible adiabatic expansion outlet enthalpy

$$h_{out,turb} = \left(h_{out,is} - h_{in}\right)\cdot\eta_{is,turb} + h_{in} \tag{13}$$

for both turbomachines.

The connected motor and generator are assumed to be permanent magnet synchronous machines with an exergetic efficiency of 97 %.

3.2. Solid media thermal energy storage

3.2.1. Porous two-phase model

The counterflow STES has been investigated in the context of a Brayton battery in [19–23,32,33,41]. The basis of these introduced models is Schumann's two-phase and one-dimensional model [42] with a time-varying temperature field during thermal cyclic operation. On this basis, a simplified thermal model can be formulated under three simplifying assumptions. First, the thermal storage capacity in the fluid phase is assumed to be small. Second, conduction is assumed to be exclusively axial due to the low thermal conductivity. Finally, thermal losses to the ambient are small for large-scale dimensions [30]. The one-dimensional axial model can be normalized in time t^* and space z^* and expressed as follows:

$$\frac{dT_S}{dt^*} = \Pi_{\mathrm{STES}}\left(T_F - T_S\right) \text{ with } \Pi_{\mathrm{STES}} = \frac{k\,a_v\,\tau\,V_{STES}}{m_{STES}\,c_{p,STES}} \tag{14}$$

$$\frac{dT_F}{dz^*} = \Lambda_{\mathrm{STES}}\left(T_S - T_F\right) \text{ with } \Lambda_{\mathrm{STES}} = \frac{k\,a_v\,V_{STES}}{\dot{m}_F\,c_{p,F}} \tag{15}$$

The thermodynamic behavior can then be summarized with only the reduced period duration Π_{STES} and the reduced regenerator length Λ_{STES}. Here, the solid and fluid phase temperatures are represented by T_S and T_F. Other properties of the setup are: a_v is the heat transfer surface to volume V_{STES} ratio, τ is the period duration, $\dot{m}_F$ is the mass flow rate, m_{STES} is the total STES inventory mass, and $c_{p,F}$ and $c_{p,STES}$ are the specific heat capacities of the fluid and the solid.

3.2.2. Packed bed regenerator

The characteristic parameters introduced in the previous section are set for the honeycomb inventory option using a reduced regenerator length of $\Lambda_{STES} = 100$, the specific surface area $a_v = 344\ \mathrm{m}^{-1}$ and a void fraction $\varepsilon = 0.70$ of a 10 m packed bed diameter. Pressure loss is considered for the design study and is limited to the practical value of 10 mbar using the correlation from [43]. These specifications have been chosen for both, the LT- and HT-STES, respectively. A temporal averaged fluid outlet temperature $T_{F,out}$ is used to simplify the modeling of the time-varying fluid outlet temperature on system-level simulation:

$$T_{F,out} = T_{F,in} - \eta_{ex,STES}\cdot\left(T_{in} - T_{in,cold}\right) \tag{16}$$

$$T_{F,out} = T_{F,in} + \eta_{ex,STES}\cdot\left(T_{in,hot} - T_{in}\right) \tag{17}$$

The outlet temperature is given by the cyclic inlet temperatures $T_{F,in}$ during charging and discharging period, as well as the regenerator's exergetic efficiency $\eta_{ex,STES}$:

$$\eta_{ex,STES} = \frac{\left|T_{F,in} - T_{F,out}\right|}{T_{F,hot,in} - T_{F,cold,in}} \tag{18}$$

3.3. Heat exchanger

3.3.1. NTU-ε-model

In order to describe the heat transfer in the HX, the well-known NTU-ε-model [44] has been applied with the assumption of small thermal losses. The efficiency of transferring heat from the air towards the water coolant during the charging period determines the thermal cyclic behavior of the HX. By considering the heat and mass balances, the hot and cold WF outlet temperatures can be determined using the HX effectiveness $\varepsilon_{\mathrm{HX}} = \dot{Q}_{HX}/\dot{Q}_{HX,max}$:

$$T_{F,hot,out} = -\varepsilon_{HX}\cdot\left(T_{F,hot,in} - T_{HX,in}\right) + T_{F,hot,in} \tag{19}$$

$$T_{F,cold,out} = \varepsilon_{HX}\cdot\left(T_{F,hot,in} - T_{HX,in}\right) + T_{HX,in} \tag{20}$$

Here, $T_{F,hot,in}$ and $T_{HX,in}$ represent the HX inlet temperatures of the hot WF and water coolant temperatures, where $T_{HX,in} = T_{2',HX}$ for the first HX and $T_{HX,in} = T_{4',HX}$ for the second HX. When the charging and discharging periods have equal durations and mass flow rates, only the heat exchanger effectiveness $\varepsilon_{\mathrm{HX}}$ is required. Finally, heat exchanger size (*NTU*: number of transfer units) in counter flow is calculated as:

$$NTU = \frac{\varepsilon_{HX}}{1 - \varepsilon_{HX}} \tag{21}$$

This set of equations facilitates the computation of the pressurized air temperatures and water coolant after passing through the heat exchanger during the cyclic Brayton CB operation.

3.3.2. Shell-and-tube heat exchanger

Shell-and-tube heat exchangers are considered using the *ε-NTU* in combination with the Kern method [44], applying the operating conditions of the Brayton battery. The heat transfer tubes have a set length of $L_{HX} = 9$ m, a thickness of 2 mm and an outer tube diameter of 38 mm. To reduce pressure loss, the WF flows through the shell side, which is fixed at a pressure loss of 20 mbar. The design method is described in detail in [44].

3.4. Electric flow heater

3.4.1. Porous two-phase model with heat source

The modeling approach for the EFH is based on a simplified two-phase transient model developed by Belik et al. [22]. This approach uses dimensionless characteristic parameters referred to as heat source number Φ, heater length Λ_{EFH}, heater loss number Γ_{EFH} and Stanton number *St*. The one-dimensional axial model is normalized in time t^* for the solid phase (S)

$$\frac{dT_S}{dt^*} = \Phi\ St\ T_{F,in} + \frac{St}{1-\varepsilon}(T_F - T_S) \tag{22}$$

and in space z^* for the fluid phase (F)

$$\frac{dT_F}{dz^*} = \Lambda_{EFH}(T_S - T_F) - \Gamma_{EFH}(T_F - T_0) \tag{23}$$

using the Dirichlet boundary condition for the inlet $T_{F,in} = T_{3'}$ and adiabatic boundary condition for the outlet $-\lambda\frac{\partial T_{eF}}{\partial z^*} = 0$.

The introduced formulation describes the thermodynamic behavior of the EFH with only four dimensionless parameters. Neglecting thermal insulation losses to the ambient with $\Gamma_{EFH} = 0$, this formulation reduces to only three parameters:

$$\Phi = \frac{\dot{Q}_{PtH}}{V_{EFH}(1-\varepsilon)\ k\ a_v\ T_{F,in}} = \frac{\dot{q}_{PtH}}{k\ a_v\ T_{F,in}} \tag{24}$$

$$\Lambda_{EFH} = \frac{k\ a_v\ H_{EFH}}{w_F\ \varepsilon\ \bar{\rho}_F\ \bar{c}_{p,F}} \tag{25}$$

$$St = \frac{k\ a_v\ \tau}{\bar{\rho}_{EFH}\ \bar{c}_{p,EFH}} \tag{26}$$

where $\dot{Q}_{PtH}$ represents the electrical heat source inside the total EFH volume V_{EFH}, *k* denotes the heat transfer coefficient to the porous media, and a_v the surface area-to-volume ratio for the convective heat transfer. Furthermore, H_{EFH} gives the length, w_F represents the fluid's velocity, $\bar{\rho}_{EFH}$ denotes the solid's density, $\bar{c}_{p,EFH}$ gives the solid's heat capacity, and τ' indicates the charging duration.

3.4.2. Induction air heater

The introduced general modeling approach can be adjusted to the proposed EFH concept, referred to as the induction air heater. This EFH concept achieves high process temperatures due to the typically high power density of the induction heating technology [45] required for the application in Brayton CB. A dispersed silicon infiltrated silicon carbide (SiSiC) pebble bed (PB) is proposed to obtain a high heater efficiency of 85 % [40], even at the required heater temperatures beyond the Curie point of steel (768 °C). This PB has a typical void fraction of $\varepsilon = 0.40$, a specific averaged heat capacity of $\bar{c}_{p,SiSiC} = 1.10\ kJ\ kg^{-1}K^{-1}$, and an averaged material density of $\bar{\rho}_{SiSiC} = 2800\ kg\ m^{-3}$.

The following formulation for the heat source term $\dot{Q}_{PtH}$ is taken from [40] where the volumetric power density $\dot{q}_{ind,PB}$ is generated inside the inductively heated pebble bed volume V_{PB}:

$$\dot{Q}_{PtH} = \dot{q}_{ind,PB} V_{PB} \tag{27}$$

The volumetric power density is given as:

$$\dot{q}_{ind,PB} = 0.75 H_o^2 2\pi f \mu_0 F \tag{28}$$

where H_0 is the external magnetic field strength, *f* is the frequency, μ_0 is the magnetic field constant, and *F* is the power transmission factor defined in [40], that characterizes the effectiveness of energy dissipation inside the pebble bed. The volume of the PB is finally given by

$$V_{PB} = \frac{\pi}{4} D_{PB}^2 H_{PB}(1-\varepsilon) \tag{29}$$

using the outer diameter, which is fixed to $D_{PB} = 1.5\ m$ and the variable bed height that corresponds for the design study to the heater length $H_{PB} = H_{EFH}$. The pressure drop of the pebble bed is calculated using the formulation given by Ergun [46].

4. Simulation setup

The governed equations from Section 3 are implemented into the Matlab environment based on the procedure from Fig. 5 using Eqs. (14) and (15), as well as Eqs. (22) and (23), the system can be numerically solved by using a backward finite-difference method in space. The WF temperatures are obtained from [27] at each iteration and in each cycle point until reaching the cyclic equilibrium, as shown in Fig. 4. This convergence criterion is satisfied once the difference between temperatures is below 10^{-6} K. On a component level, several cycles of operation must be computed to obtain the thermal equilibrium condition inside both STES components. Here, the simulation ends when the change in thermal energy falls below 10^{-4} J in between cycles.

5. Results of parametric studies

In this study, an investigation of a Brayton CB system was conducted under a steady-state operating condition with a 7 h charging period and a 7 h discharging period. The total storage capacity of the investigated system is 210 MWh.

To quantify the potential of leveraging the system costs and the influence on RTE through additional PtH integration, parameter studies are conducted. For this purpose, we applied the component models and their specifications introduced in chapter 3 using the simulation algorithm from Fig. 4. In doing so, we considered pressure drops for STESs, EFH, and HXs, but neglected their thermal losses.

In Section 5.1 we first conduct a brief techno-economic analysis to obtain a technical indicator for system's capital expenditures (CAPEX). The found correlation is then used in further sections for cost reasoning. In Section 5.2, we present a sensitivity analysis results for a system without the EFH component in order to evaluate the influence of turbomachinery, HXs and STESs on the RTE η_{rt}. Then we integrated the

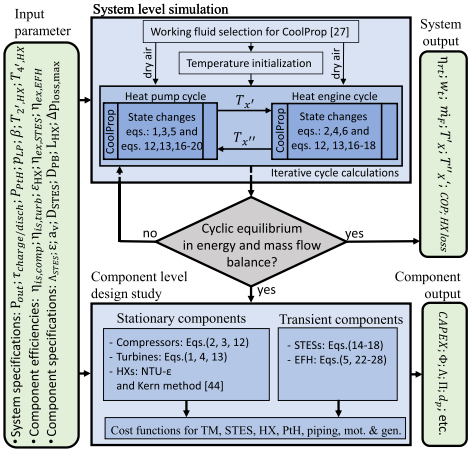

Fig. 4. Simulation algorithm for system and component level calculations.

EFH to investigate its impact on system cost and RTE. we carried out a design study for the EFH component to provide design solutions for HT application in a Brayton CB.

5.1. Correlation to system costs

In order to identify a technical key performance indicator that correlates with the CAPEX, simulation studies are conducted applying component models introduced in chapter 3 together with cost functions from Peters et al. [44] (HX and piping) and from the ADELE-ING project [11,12] (TM, STES and EFH). In this study, the 210 MWh Brayton battery system with efficient STES regenerator solutions ($\eta_{ex.STES} = 0.95$) has been investigated varying the pressure ratio β and the HX4 efficiency in the range $\varepsilon_{HX4} = [0.50 : 0.90]$ similar to the study from Section 5.3. In addition to this parameter variation, electrical heating with up to 35 MW ($\dot{X}_{EFH} = 0.23$) is applied to the system to compare the discharged specific technical work w_t with the CAPEX C_{CAPEX}. The total CAPEX is the sum of all component costs that is multiplied by two factors f_i and f_c, which consider installation and contingency costs, respectively: $C_{CAPEX} = f_i f_c \sum C_i$. Both factors are assumed to be 1.1 that is the average value taken from [44].

Results from Fig. 5 demonstrate a correlation between the specific technical work and the CAPEX for various pressure ratios and the both cases, with additional electrical heating (top) and without it (down). Accordingly, the CAPEX can be estimated as inversely proportional to the root of the specific technical work by the following relation:

$$C_{CAPEX} \sim w_t^{-0.5}$$

The linear regression fit with a high coefficient of determination of $R^2 = 0.9739$ proves the linearity and returns the coefficient of proportionality $p = 3100\ €\sqrt{Wh}/kWh/\sqrt{kg_{air}}$ and $c = -35.6\ €/kWh$ to express the following linear relationship

$$\widetilde{C}_{CAPEX} = 3100\ w_t^{-0.5} - 35.6\ \forall\ w_t^{-0.5} \in [0.09, 0.3]\ kg^{0.5}Wh^{-0.5} \tag{30}$$

that can be expressed in [€/Wh] using $p = 3.10\ €/\sqrt{Wh \cdot kg_{air}}$:

$$\widetilde{C}_{CAPEX} = 3.1\ w_t^{-0.5} - 0.0356\ \forall\ w_t^{-0.5} \in [0.09, 0.3] kg^{0.5}Wh^{-0.5} \tag{31}$$

This found correlation is in particular valid for an operation under ideal gas conditions with temperatures far beyond 500 °C and pressure ratios above 9. Especially in the validity range of $0.09\ kg^{0.5}Wh^{-0.5} < w_t^{-0.5} < 0.18\ kg^{0.5}Wh^{-0.5}$, a minor variation of the results is observed. In conclusion, this revealed relationship indicates the system costs with only two derived indicators: The mass of the working fluid m_{WF} cyclically circulated in the system and the technical work w_t delivered by the system. We use only the technical work as an indicator for further cost reasoning in this work.

Furthermore, the comparison of the volumetric energy density (color coded) between both cases from Fig. 5 shows the maximum increase by 70 % to 104.6 kWh/m^3 for the case with added electrical heating and $\beta = 15$. In comparison, Benato's techno-economic assessment for a TES build-up with Al_2O_3 bricks demonstrated an energy density increase by 105 % to 430 kWh/m^3 accompanied by a CAPEX reduction of 35 % to 54 $/kWh using low-cost turbomachinery. Chen et al. [21] also achieved a redoubling of the energy density to 62.2 kWh/m^3 by adding electrical heating into the proposed hybrid system.

5.2. Sensitivity analysis

To investigate the influence of each component on RTE and CAPEX, we conducted a sensitivity analysis, taking into account the set of central specifications listed in Table 3. In addition, the efficiencies of the following components were varied for this purpose: exergetic efficiencies $\eta_{ex.STES}$ of both STESs, effectivenesses ε_{HX} of both HXs and isentropic efficiencies η_{is} of turbomachines. All these parameters are indicated in Fig. 6 with the notation "η_i."

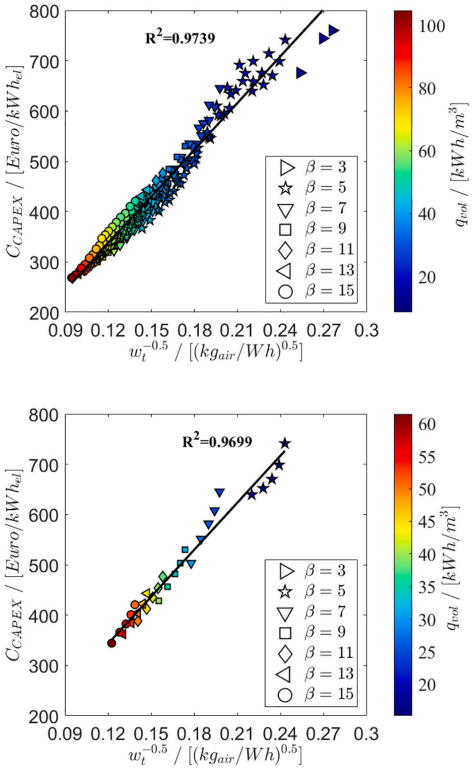

Fig. 5. Correlation between system cost and specific technical work valid for $\beta = [3 : 15]$ and $w_t^{-0.5} = [0.09 : 0.30]$; top: case with additional electrical heating; and down: case without electrical heating. (For interpretation of the references to color in this figure, the reader is referred to the web version of this article.)

Table 3
Component efficiencies defined for parameter study.

$\eta_{is.turb}$	$\eta_{is.comp}$	$\eta_{ex.STES}$	ε_{HX2}	ε_{HX4}	η_{EFH}	$\eta_{M/G}$
0.90	0.87	0.85–0.95	0.90	0.5–0.90	0.85	0.97

The results from Fig. 6 without PtH implementation are presented at the design point $\eta_i = 0.90$, with an RTE of 48 % and capital costs per unit energy discharged of 384 €/kWh$_{el}$. As expected, increasing component efficiency leads to an increased RTE.

The turbomachines have a dominant impact on the efficiency here. In particular, the turbines show the greatest impact on that performance metric since their exhaust loss at $T_{4'}$ (see Fig. 2) is associated with the highest exergy loss. In contrast, HXs have a marginal impact on RTE, however, the specific costs significantlyincrease with an increasing HX effectiveness due to the enormously rising heat transfer area. Moreover, this study shows that both STESs have significant impact on the RTE as well as on the specific system costs, since these components improve the

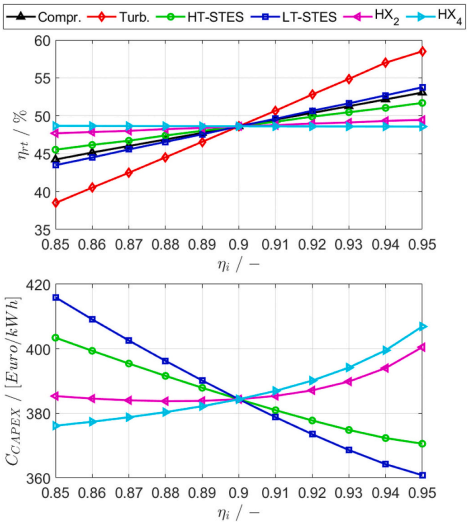

Fig. 6. RTE and specific CAPEX of a 210 MWh, 600 °C Brayton CB system without EFH for efficiencies $\eta_i = [0.85 : 0.95]$.

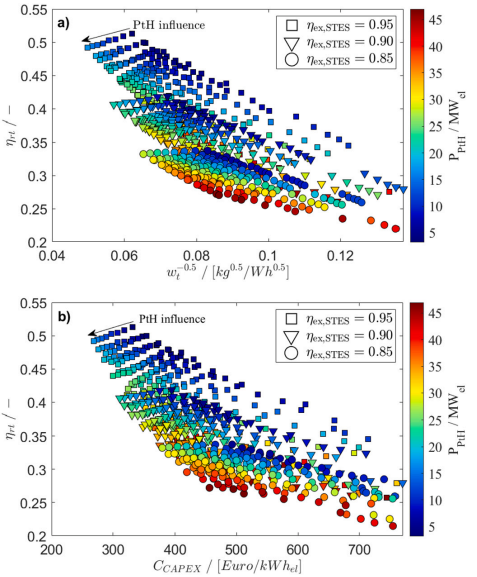

Fig. 7. Brayton CB design solutions for RTE and spec. technical work a) and spec. CAPEX b) in relation to the electric heating power.

energy density of the system by providing exergy enriched high-temperature heat to the Brayton HE cycle with high efficiencies. Therefore, to achieve a high cost efficiency and a high energy efficiency, STES components must have high efficiencies above 90 %.

5.3. Parameter study

In contrast to the sensitivity analysis, where component efficiencies varied and process parameters remained, as presented in Table 3, this study aims to vary process parameters as HX temperatures, pressure ratios and electric heating power at fixed efficiencies. The component efficiencies indicated in Table 4 have been chosen on the basis of the findings from the previous section, which indicate that turbomachines and STES components have high efficiencies while HX and EFH have lower efficiencies in order to save costs and thus achieve higher cost efficiency. Aside from the variation of the heating rate, the pressure ratio β has been varied from 3 to 15 whereby the effectiveness ε_{HX4} of HX4 and STES efficiency have been varied from 0.50 to 0.90 and from 0.85 to 0.95, respectively. The HX temperatures have been set to 20°C for the HX2 in the high-pressure stage and to 100 °C for the HX4 in the low-pressure stage. The induction air heater is assumed to operate with an induction air heater efficiency of 85 %, which agrees with the study from [40] at laboratory scale for outlet temperatures up to 700 °C.

Fig. 7 presents a variety of Brayton battery design solutions based on the wide-ranged parameter study comparing the RTE to the square root of the inverse technical work a) and to the specific CAPEX b). The comparison between the design solutions from Fig. 7 a) and b) clearly shows the linear relationship found in Section 5.1, in particular for design solutions with a high STES efficiency of 95 %.

The electric heating power is color coded and shows its influence on RTE and CAPEX: higher heating rates result in reduced system costs but also in lower RTE. The effect of cost reduction to the detriment of efficiency has already been presented in [19] for A-CAES and in [21] for a hybrid storage system comprising a HT-PTES with an ORC cycle.

To highlight the influence of the EFH on system costs and RTE, and to quantify the tradeoff between these both investment criteria, we further analyzed in Fig. 8 the difference quotients with respect to electric heating power. To this end, we extracted part of the results from Fig. 7 for $\eta_{ex,STES} = 0.95$ and calculated the difference quotients for specific technical work $\Delta w_t^{-0.5}/\Delta\eta_{rt}$ and for the CAPEX $\Delta CAPEX/\Delta\eta_{rt}$ with respect to the absolute RTE loss of 1 % point.

The results quantify the effect of cost reduction, caused by the additional electric heating power. The difference quotient for cost savings increases with less effective HX designs from 15 €/kWh/%pt$_{RTE}$ to almost 60 €/kWh/%pt$_{RTE}$. The reduced HX effectiveness lifts the inlet temperature of the HP compressor and improves the coefficient of performance (COP) for the HP cycle. The higher COP leads to improved energy-efficiency which is illustrated by the color-coded RTE in Fig. 8. As a result, the efficiency losses caused by the electrical heating are limited in relation to the total loss of RTE, hence the cost reduction effect of the EFH increases. This effect is amplified if the heating takes place at high temperatures, as this minimizes energy losses of the EFH. The tradeoff between CAPEX and RTE is further illustrated in Fig. 9 by extracting the solution marked with '*' from Fig. 8 at 30 €/kWh cost savings per 1%pt. of RTE. Results from Fig. 9 clearly demonstrate the CAPEX reduction for all system components besides the EFH itself. As a result, an electric heating power of 17 MW reduce the system CAPEX to <300 €/kWh$_{el}$. In addition, the applicability of the cost estimation function from Eq. (30) is demonstrated in Fig. 9: The linear $\widetilde{C}_{CAPEX}$ function illustrated by the dashed line, underestimates the sum of the

Table 4
Central specifications for system level simulations.

Working fluid	$T_{4,Comp,in} = T_{4,HX}$	$T_{2,HX}$	p_{LP}	β
Air (real gas)	245 °C	20 °C	1 bar	10

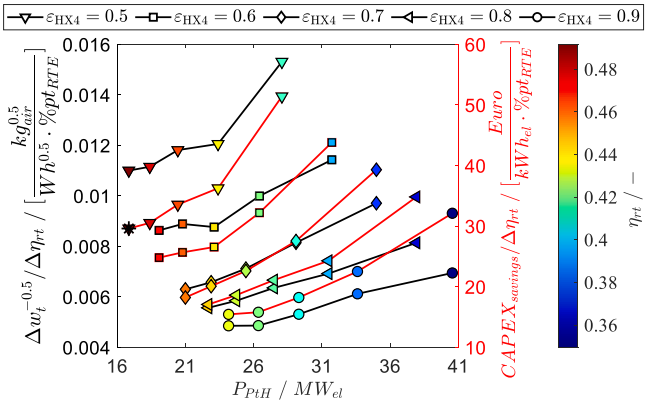

Fig. 8. Cost reduction potential through additional electric heating power on design solutions from Fig. 7 for $\eta_{ex,STES} = 0.95$ and for various ε_{HX4}.

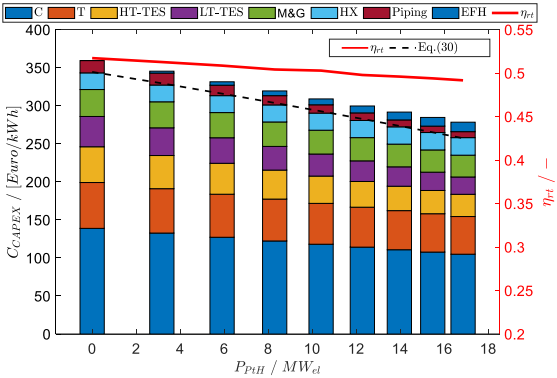

Fig. 9. Cost reduction effect through additional heating power on design configuration '*' from Fig. 8: β = 15, $\varepsilon_{HX4} = 0.50$, $T_{2,HX} = 20°C$, $\eta_{ex,STES} = 0.95$; and demonstration of CAPEX estimation using Eq. (30).

equipment costs C_{CAPEX} by a maximum of 7 %. Moreover, the red line depicted in Fig. 9 shows the RTE, which likewise decreases, but with a reduced slope: While the efficiency loss is only 5 %, the costs are reduced by 23 % compared to the case without PtH integration (360 €/kWh; $\eta_{rt} =$ 0.517). Overall, according to the results from this parameter study, CAPEX are significantly reduced with an increased heating power. Furthermore, this cost reduction effect offers the plant operator the flexibility to adjust CAPEX by the installed EFH capacity.

The results presented in Figs. 7 and 9 have been additionally verified using cost functions from [18]. Additional information regarding the verification approach and results for the highest STES efficiency of 95 % can be found in Appendix B. Fig. B1 shows similar results compared with the outcomes reported in Fig. 7 b) and therefore leads to identical conclusions. However, there are major differences to our results in the distribution of system costs, which are illustrated in Fig. B2. While our results identified the turbomachinery as the major expense, Benato's cost distribution shows that the highest costs are associated with the thermal energy storage components. In addition, Benato's cost expressions for motor and generator units have only a minor impact on the total cost of the Brayton CB. In contrast, the electric heating component significantly influence the system CAPEX: while Benato's expression gives electric flow heater cost of up to 850 €/kW_{el}, we obtained 160 €/kW_{el} for the utility scale induction air heater. Even if we apply Benato's formulation for the electric heater cost ($C_{EFH} = 75000 \cdot P_{EFH}^{0.9}$), a slight reduction of system CAPEX still occurs, confirming our main conclusion on cost leverage. However, this cost reduction effect dissipates at marginal cost of around 950 €/kW_{el} resulting in reduced cost efficiency and energy efficiency as well.

5.4. Induction air heater design solutions

Induction heating has the potential to convert utility-scale electric

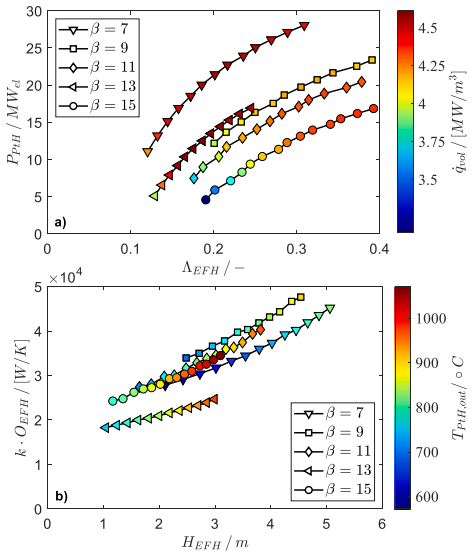

Fig. 10. EFH design solutions with three pressure vessels, each with $D_{PB} = 1.5$ m, $\eta_{PtH} = 0.85$: a) electric heating power related to dimensionless parameters from Section 3.4.1; b) k^*O in relation to the required heater length H_{EFH}.

power into high-temperature (HT) heat. However, a sufficiently high heat transfer area must be provided to transfer the induced HT heat to the gaseous WF. Therefore, the objective of this design study is on the one hand, to calculate the heat transfer area of the proposed pebble bed air heater PtH concept, and on the other hand, to determine its dimensions. To this end, we chose results with the highest RTE from Section 5.2 to obtain design solutions for the EFH using the design tool formulated in Section 3.4 and material specifications for silicon carbide obtained from [40]. To allow a proper comparison of the design solutions, the component's pressure loss is set to 100 mbar. Moreover, the induction air heater operates at 85 % efficiency using a frequency of 5 kHz and a peak current in the inductor windings of 800 A.

Fig. 10 presents design solutions for the induction air heater in a dimensionless manner a) using the dimensionless heater length Λ_{EFH}, and in a dimensioned way b), giving the outlet temperature in relation to the EFH bed height. Both diagrams show that to achieve a high volumetric power density $\dot{q}_{vol}$ together with a high outlet temperature $T_{PtH,out}$, either the heat transfer surface O_{EFH} or the heat transfer coefficient k must increase with a larger heater length (i.e., larger PB height). Moreover, to ensure a given pressure loss of 100 mbar for the obtained bed height, an EFH configuration with three modules is needed where corresponding sphere diameters between 120 mm and 180 mm are used. Thus, bed heights of up to 5 m in each module are required to ensure maximum temperatures of up to 1050 °C with a volumetric power density below 4.5 MW/m^3. Such high temperatures can be achieved by available resistive EFH only at the expense of its operational lifetime. Therefore, the silicon-carbide-based induction heater is an affordable and feasible solution that meets the high-temperature requirements of a Brayton CB application ensuring high lifetime expectations.

6. Conclusions

A techno-economic study has been conducted to assess the impact of additional Power-to-Heat (PtH) integration on a closed-loop Brayton Carnot battery (CB) system. The objective of this study was to quantify the tradeoff between system cost and round-trip efficiency (RTE) arising from the integration of the additional electric heating and to provide novel design solutions for such a high-temperature electric heating (HT-EH) component. To this end, component models for the central components were developed and implemented in the system model together with associated cost functions. On this modeling basis, we investigated a Brayton CB air system with 210 MWh energy storage capacity and a seven-hour charging and discharging periods under a cyclic steady-state operating condition and evaluated the influence of additional electric heating rates on cost and energy efficiency.

The primary results of this contribution are as follows:

- A correlation was found between system costs C_{CAPEX} and discharged specific technical work w_t ($C_{CAPEX} \sim w_t^{-0.5}$) to estimate cost reduction due to additional electrical heating
- This correlation reveals that CAPEX are principally affected by the working fluid's mass cyclically circulated in the system and by its delivered technical work
- The linear cost function derived demonstrates the significant decline in CAPEX with increasing technical work, which can be increased by additional electric heating
- A sensitivity analysis of component efficiencies clarifies that the turbomachinery primarily and the solid media thermal energy storages secondarily must have efficiencies above 90 % to ensure high cost efficiency and high energy efficiency as well for the system
- The parameter study proves that additional integration of an HT electric flow heater (EFH) upstream of the HT-STES is a cost-effective way to increase the specific technical work and thus reduce the cost of the Brayton CB. However, with the penalty of reduced round-trip efficiency, an additional electric heating power of up to 17 MW results in a cost reduction of up to 23 % to <300 €/kWh, along with an efficiency loss below 5 % to 49 % RTE.
- The design study for an induction air heater based on an inductively heated silicon infiltrated silicon carbide pebble bed reveals a compact container design providing an outlet temperature of 1050 °C with a power density of 4.5 MW/m^3

Altogether, PtH integration offers a significant cost leverage for the Brayton CB when a compact EFH is added into the system. However, this novel component must provide high outlet temperatures above 1000 °C under pressures above 10 bar while maintaining a high conversion efficiency of over 85 %. Since parasitic losses of induction heating and thermal losses to the ambient have been neglected in this work, further research effort needs to be carried out to propose design solutions for the insulated pressure vessel and to validate this PtH concept under the high-temperature working conditions of the Brayton Carnot battery.

CRediT authorship contribution statement

Sergej Belik: Conceptualization, Methodology, Software, Data curation, Investigation, Writing – original draft, Writing – review & editing, Visualization.

Declaration of competing interest

The authors declare that they have no known competing financial interests or personal relationships that could have appeared to influence the work reported in this paper.

Data availability

The data that has been used is confidential.

Appendix A

To illustrate the major impact of pressure ratio β and HX temperature (i.e. HP compressor inlet temperature) on the specific technical work w_t, the results of Eqs. (9) and (10) for dry air are presented in Fig. A1. The results show a linear increase in the specific technical work for both process parameters. In addition, the results illustrate the difference between the polytropic process and an ideal isentropic process.

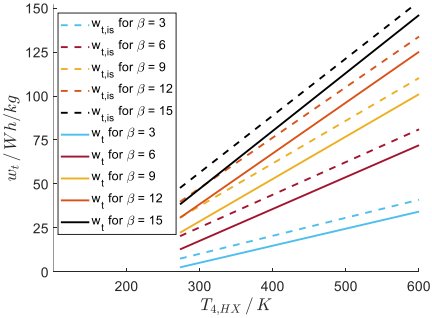

Fig. A1. Comparison of polytropic (at $\eta_p = 0.9$) and isentropic (at $\eta_p = 1.0$) specific technical work results based on the thermodynamic analysis from Section 2.2 using $\bar{c}_{p,air} = 1.14\ kJkg^{-1}K^{-1}$ and $\kappa = 1.35$.

Appendix B

To verify that our results are robustness to the use of different cost functions, we recalculated our design solutions from Fig. 7 b) using cost expressions from Benato [18]. In addition to cost functions taken from [18], we applied our piping cost to calculate the total capital cost, which equal the sum of all component CAPEX. This value is further multiplied by Benato's system cost factor and currency exchange rate €/$ of 1.12.

The results of this robustness check are presented in Fig. B1 for a thermal energy storage efficiency of $\eta_{ex,STES} = 0.95$. Fig. B1 illustrates results that are similar to the main findings reported in Fig. 7 b), which lead to identical conclusions of cost reduction through increased additional heating power.

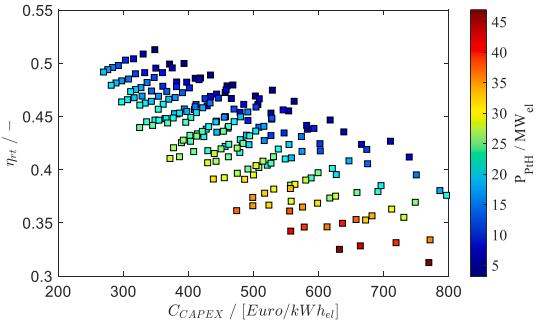

Fig. B1. Techno-economic assessment using Benato's [18] cost functions for a comparison to results for efficient STES designs with $\eta_{ex,STES} = 0.95$ from Fig. 7 b).

Moreover, Fig. B2 presents the distribution of system CAPEX for design solutions from Fig. 9 using Benato's cost functions. Although the electric heating component has significantly higher costs, the results confirm the cost reduction effect. However, this effect vanishes at the marginal cost of around 950 €/kW resulting in higher system costs and lower RTE.

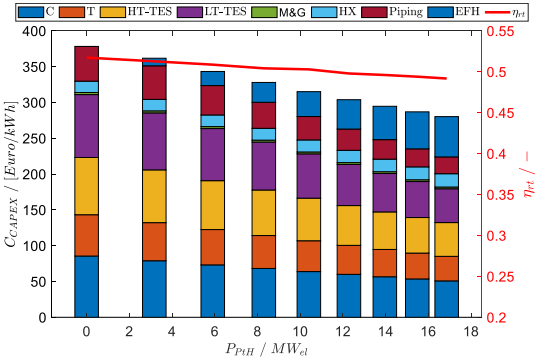

Fig. B2. Cost reduction through additional electric heating power for design solutions from Fig. 9 using Benato's [18] cost functions (C: compressors; T: turbines; TES: thermal energy storages; M&G: motor and generator; HX: heat exchanger; EFH: electric flow heater).

References

[1] Renewable Energy Policy Network for the 21st Century, Renewables 2022 Global Status Report, REN21. www.ren21.net/wp-content/uploads/2019/05/GSR2022_Full_Report.pdf, 2022.

[2] S. Rehman, L.M. Al-Hadhrami, M.M. Alam, Pumped hydro energy storage system: a technological review, Renew. Sust. Energ. Rev. 44 (2015) 586–598, https://doi.org/10.1016/j.rser.2014.12.040.

[3] E. Barbour, I.G. Wilson, J. Radcliffe, Y. Ding, Y. Li, A review of pumped hydro energy storage development in significant international electricity markets, Renew. Sust. Energ. Rev. 61 (2016) 421–432, https://doi.org/10.1016/j.rser.2016.04.019.

[4] M. Budt, D. Wolf, R. Span, J. Yan, A review on compressed air energy storage: basic principles, past milestones and recent developments, Appl. Energy 170 (2016) 250–268, https://doi.org/10.1016/j.apenergy.2016.02.108.

[5] A. Benato, A. Stoppato, Pumped thermal electricity storage: a technology overview, Therm.Sci.Eng.Prog. (2018), https://doi.org/10.1016/j.tsep.2018.01.017.

[6] Olivier Dumont, et al., Carnot battery technology: a state-of-the-art review, J. Energy Storage 32 (2020), 101756.

[7] Ting Liang, et al., Key components for Carnot Battery: technology review, technical barriers and selection criteria, Renew. Sust. Energ. Rev. 163 (2022), 112478.

[8] Andrea Vecchi, et al., Carnot battery development: a review on system performance, applications and commercial state-of-the-art, J.Energy Storage 55 (2022), 105782.

[9] F.J. De Sisternes, J.D. Jenkins, A. Botterud, The value of energy storage in decarbonizing the electricity sector, Appl. Energy 175 (2016) 368–379.

[10] Haobai Xue, A Comparative Analysis And Optimisation of Thermo-Mechanical Energy Storage Technologies, University of Cambridge, 2019. Diss.

[11] S. Zunft V. Dreissigacker M. Bieber A. Banach C. Klabunde O. Warweg , "Electricity storage with adiabatic compressed air energy storage: Results of the BMWi-project ADELE-ING," in Proc. 2017 International ETG Congress, Bonn, Germany, pp. 1-5.

[12] S. Zunft, M. Krüger, V. Dreißigacker, S. Belik, J. Hahn, P. Knödler, in: Züblin A. G. Stuttgart (Ed.), ADELE-ING: Engineering-Vorhaben für die Errichtung der ersten Demonstrationsanlage zur adiabaten Druckluftspeichertechnik: official report, 2017.

[13] M. Mercangöz, J. Hemrle, L. Kaufmann, A. Z'Graggen, C. Ohler, Electrothermal energy storage with transcritical CO2 cycles, Energy 45 (1) (2012) 407–415, https://doi.org/10.1016/j.energy.2012.03.013.

[14] MAN, Energy Storage. "Electro-thermal energy storage". https://www.man-es.com/energy-storage/solutions/energy-storage/electro-thermal-energy-storage, 2021 accessed 3 January 2023.

[15] W.D. Steinmann, The CHEST (Compressed Heat Energy STorage) concept for facility scale thermo mechanical energy storage, Energy 69 (2014) 543–552, https://doi.org/10.1016/j.energy.2014.03.049.

[16] SIEMENS, Siemens presents thermal storage solution for wind energy, 27 September 2016 (2016-09-27), WindEnergy Hamburg Ref nr: PR2016090419WPEN, pages 1 - 4, XP055456571; 2021 [accessed 03 January 2023].

[17] Franz Trieb André Thess . "Storage plants–a solution to the residual load challenge of the power sector?." Journal of Energy Storage 31.

[18] A. Benato, Performance and cost evaluation of an innovative pumped thermal electricity storage power system, Energy 138 (2017) 419–436, https://doi.org/10.1016/j.energy.2017.07.066.

[19] Volker Dreißigacker, Sergej Belik, System configurations and operational concepts for highly efficient utilization of power-to-heat in A-CAES, Appl. Sci. 9 (7) (2019) 1317.

[20] S. Houssainy, M. Janbozorgi, P. Kavehpour, Thermodynamic performance and cost optimization of a novel hybrid thermal-compressed air energy storage system design, J.Energy Storage 18 (2018) 206–217, https://doi.org/10.1016/j.est.2018.05.004.

[21] L.X. Chen, P. Hu, P.P. Zhao, M.N. Xie, F.X. Wang, Thermodynamic analysis of a high temperature pumped thermal electricity storage (HT-PTES) integrated with a parallel organic Rankine cycle (ORC), Energy Convers. Manag. 177 (2018) 150–160.

[22] Sergej Belik, Volker Dreissigacker, Stefan Zunft, Power-to-heat integration in regenerator storage: enhancing thermal storage capacity and performance, J. Energy Storage 50 (2022), 104570.

[23] T. Desrues J. Ruer P. Marty J. Fourmigué . A thermal energy storage process for large scale electric applications. Applied Thermal Engineering.

[24] T. Silvia, B. Bjarke, G. Rafael, Techno-economic assessment of a carnot battery for industrial application, in: 3rd International Workshop of Carnot Batteries. (IWCB), Stuttgart, Germany, September 2022.

[25] W.D. Steinmann, H. Jockenhöfer, D. Bauer, Thermodynamic analysis of high-temperature Carnot battery concepts, Energy Technol. 8 (3) (2020) 1900895, https://doi.org/10.1002/ente.201900895.

[26] Y. Zhao, J. Song, M. Liu, Y. Zhao, A.V. Olympios, P. Sapin, C.N. Markides, Thermo-economic assessments of pumped-thermal electricity storage systems employing sensible heat storage materials, Renew. Energy 186 (2022) 431–456.

[27] I.H. Bell, J. Wronski, S. Quoilin, V. Lemort, Pure and pseudo-pure fluid thermophysical property evaluation and the open-source thermophysical property library CoolProp, Ind. Eng. Chem. Res. 53 (6) (2014 Feb 12) 2498–2508, https://doi.org/10.1021/ie4033999.

[28] NIST Standard Reference Database 23, NIST Thermodynamic And Transport Properties of Refrigerants And Refrigerant Mixture REFPROP, Version 9.1, 2013.

[29] Joshua D. McTigue, et al., Techno-economic analysis of recuperated Joule-Brayton pumped thermal energy storage, Energy Convers. Manag. 252 (2022), 115016.

[30] H. Hausen, Wärmeübertragung im Gegenstrom, Gleichstrom und Kreuzstrom, Springer, Berlin, Heidelberg, 1976.

[31] K.R. Shah, D.P. Sekulic, Fundamentals of Heat Exchanger Design, John Wiley & Sons, Hoboken, NJ, USA, 2003. ISBN 0-471-32171-0.

[32] R. Singh, R.P. Saini, J.S. Saini, Simulated performance of packed bed solar energy storage system having storage material elements of large size-part I, Open FuelsEnergy Sci.J. 1 (1) (2008).

[33] A. Benato, A. Stoppato, Energy and cost analysis of a new packed bed pumped thermal electricity unit, J.Energy Resour.Technol. 140 (2) (2018), 020904, https://doi.org/10.1115/1.4038197.

[34] H. Zhang, L. Wang, X. Lin, H. Chen, Parametric optimisation and thermo-economic analysis of Joule-Brayton cycle-based pumped thermal electricity storage system under various charging–discharging periods, Energy 263 (2023), 125908.

[35] M. Abarr, B. Geels, J. Hertzberg, L.D. Montoya, Pumped thermal energy storage and bottoming system part A: concept and model, Energy (2016) 1–12, https://doi.org/10.1016/j.energy.2016.11.089.

[36] André Thess, Thermodynamic efficiency of pumped heat electricity storage, Phys. Rev. Lett. 111 (11) (2013), 110602, https://doi.org/10.1103/PhysRevLett.111.110602.

[37] A. White, G. Parks, C.N. Markides, Thermodynamic analysis of pumped thermal electricity storage, Appl. Therm. Eng. 53 (2) (2013) 291–298.

[38] Schniewindt, Flow heaters. https://www.schniewindt.de/en/csn-flow-heaters/, 2021. ISBN 0-471-32171-0.

[39] Ohmex, Electrical Process Flow Heaters datasheet, in: https://www.ohmex.de/en/wp-content/uploads/sites/3/2020/03/electric-process-heater_STR_2020-03.pdf, 2021 accessed 05 Januar 2023.

[40] S. Belik, O. Khater, S. Zunft, Induction heating of a fluidized pebble bed: numerical and experimental analysis, Appl. Sci. 13 (2023) 2311, https://doi.org/10.3390/app13042311.
[41] V. Dreissigacker, Heat Mass Transf. 54 (2017) 955, https://doi.org/10.1007/s00231-017-2197-y.
[42] T.E.W. Schumann, Heat transfer: a liquid flowing through a porous prism, J. Frankl. Inst. 208 (1929) 405–416.
[43] J.D. McTigue, A.J. White, C.N. Markides, Parametric studies and optimisation of pumped thermal electricity storage, Appl. Energy 137 (2015) 800–811.
[44] Max S. Peters, Klaus D. Timmerhaus, Ronald E. West, Equipment Costs-Plant Design And Economics for Chemical Engineers, 2002.
[45] O. Lucía, P. Maussion, E.J. Dede, J.M. Burdío, Induction heating technology and its applications: past developments, current technology, and future challenges, IEEE Trans. Ind. Electron. 61 (5) (2014) 2509–2520.
[46] S. Ergun, Fluid flow through packed columns, Chem. Eng. Prog. 48 (1952) 89–94.

Chapter 3

Discussion and Conclusions

The present work investigates an induction air heater for Brayton CB applications. As presented in Figure 1.2, the challenges addressed in this thesis encompass the elaboration and validation of a suitable heater design solution with an appropriate material option for the Brayton CB (secondary leading objective) and the investigation of the heater's influence on system costs and RTE (primary leading objective). The contributions presented in this discussion chapter tackle these challenges and critically discuss the following findings concerning both leading objectives. Firstly, the elaborated EFH design with a silicon carbide (SiC) pebble bed is a well-suited solution for high-temperature applications in Brayton CB and industrial process heat. Secondly, the system implementation of this EFH solution offers substantial cost leverage outweighing the minor penalty on the RTE. These findings validate the main hypothesis of this work: incorporating a compact induction air heater downstream of the heat pump compressor results

in a notable cost advantage for the Brayton CB system. The concluding section summarizes the discussion and provides valuable insights for future research.

3.1 Micro scale: Inductively heated ceramic pebble bed

The following discussion critically evaluates the extent to which the proposed inductively heated ceramic pebble bed (PB) concept solution aligns with the secondary research objective and its suitability for the Brayton CB application. To this end, findings from the concept investigation are presented concerning the technical requirements introduced in Sec. 2.1.1, which include achieving a high outlet temperature above 550 °C, maximum volumetric power density, and ensuring maximum PtH efficiency.[1] These requirements serve as criteria for evaluating the elaborated EFH concept solution across various temperature and pressure conditions.

Thus, the inductively heated ceramic PB concept solution is critically evaluated based on these criteria in the following sections. First, the outcomes for the identified SiC ceramic and the limitations of the proof-of-concept are discussed. Next, the validity of the multi-physical model for calculating the inductively heated ceramic PB concept under high temperature and pressure is critically discussed. The last paragraph concludes this discussion on the micro scale.

[1]The definition for the PtH efficiency and volumetric power density is presented by equations (1) and (2) from Section 2.1.1.

3.1.1 Material identification: Efficient high-temperature candidates

The temperature-dependent magnetic properties of the heating material influence the efficiency of the induction heating process. While paramagnetic properties above the Curie temperature are commonly disadvantageous for heating efficiency, ferromagnetic properties below the material's Curie temperature are advantageous. Therefore, the Curie temperature of carbon steel (768 °C) was chosen to distinguish between two distinct temperature ranges, one for ferromagnetic steel and the other for paramagnetic high-temperature materials. Specific material solutions were found for the application in the Brayton CB for each temperature range. In the range below the Curie point, experimental results have identified the ferromagnetic steel (UNS G10060 or the corrosion-resistant option, X10CrAlSi7) as a suitable solution due to its high-efficient induction heating procedure, providing a maximum PtH efficiency above 90% and compact design solutions with a maximum volumetric power density of up to 4.5 MW/m^3 at the laboratory scale. Next, for the high-temperature range above the Curie point where steel loses its beneficial ferromagnetic properties, a high-temperature-resistant silicon-infiltrated silicon carbide (SiSiC) ceramic solution was proposed for the Brayton battery application. For such high temperatures, numerical system-scale design studies have revealed a PtH efficiency of up to 95% with a volumetric power density of up to 5.5 MW/m^3.

Overall, the proposed material options are suitable for induction air heater applications since they have demonstrated high PtH efficiency and volumetric power density. This conclusion is first supported by experimental and numerical results obtained at the laboratory (micro) scale for the ferromagnetic steel at temperatures below the Curie point. Secondly, for the (paramagnetic) SiSiC ceramic, this conclusion is only

supported by numerical results from the validated model obtained at the system (macro) scale for significantly higher temperatures up to 1050 °C in the Brayton CB.

3.1.2 Proof-of-concept: Temperature and pressure limitations

Though the elaborated inductively heated PB concept combined with SiSiC ceramic meets the requirements for Brayton CB applications, its experimental proof was given for limited operation conditions under atmospheric pressure and below the Curie point of steel. Above the Curie point, only theoretical outcomes based on simulation results were obtained.

The high-temperature suitability of the EFH concept was confirmed in a separate master's thesis, where high-temperature measurements up to 1020 °C were conducted using the testing facility from Sec. 2.2. The EFH concept combined with the SiSiC ceramic, presented in Figure 3.1, demonstrated high-temperature stability; however, a loss in efficiency below 8.6% was observed during the induction heating process at solid temperatures above 1000 °C due to the decreased electrical conductivity. This efficiency loss was considered for the EFH application at the system scale, where a theoretical PtH efficiency of up to 95% was achieved, as discussed in the previous section. Consequently, a minimum PtH efficiency of 86.83% was expected for the utility-scale EFH application. Notably, this efficiency value remained higher compared to the calculated efficiency of approximately 70% for the steel PB at 900 °C, without considering the corrosion and solidity issues of steel at such high temperatures. Considering these factors, the inductively heated PB concept combined with SiSiC remains a suitable EFH concept for efficiently generating high-temperature heat.

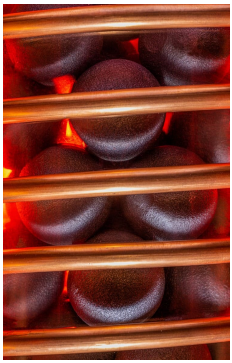

Fig. 3.1 SiSiC ceramic pebble bed with $d = 43$ mm inside the induction coil.

The experimental proof of the concept was limited to atmospheric conditions. Thus, applying a pressure setting will enhance heat transfer to the pressurized air, improving the thermal efficiency and power density, as determined in the previous master's thesis. These improvements require the implementation of a pressure vessel around the induction coil, as demonstrated in the mentioned thesis, and the proof of the gasket concept for high-temperature and operational pressure. Notably, the gasket concept from Sec. 2.2. was only tested for atmospheric pressure, so further validation is needed to demonstrate its functionality under high-temperature and high-pressure conditions in a Brayton CB.

3.1.3 Model validation: Temperature and pressure limitations

The experimental limitations discussed in the previous section allowed the model validation only under atmospheric pressure and below the Curie point using ferromagnetic steel, although the targeted model application is at high-pressure and high-temperature conditions of the

Brayton CB. While the pressure influences only the flow conditions of the fluid phase including the convective heat transfer, the temperature has additionally an impact on the strength properties and electrothermal properties of the inductively heated material.

While the numerical model accurately addressed the temperature dependence of the induction heating process by considering temperature-dependent material properties, it neglected the influence of temperature on structural strength, including elastic and plastic deformation of spheres. Moreover, the electromagnetic field solution of the numerical model essentially assumed ideal spheres electrically insulated from each other within the PB. Therefore, an electrical insulation coating was applied to the experimental PB setup to account for both assumptions before running the experiments at temperatures below the Curie point. The high-temperature coating maximized the electrical contact resistance between the spheres, preventing eddy currents from occurring over the entire PB, even at the Curie temperature.

To ensure the functionality of the ceramic coating and to avoid any loss in structural strength that could lead to potential plastic deformation, the operational temperature was kept below 600 °C. Both measures ensured the validity of the numerical model for the ferromagnetic steel PB, demonstrating satisfactory agreement (below 15% deviation) between the numerical and experimental results at Reynolds numbers above 2000. Despite these measures, the deviation increased as the solid temperature approached the Curie point at lower Reynolds numbers, leading to a non-linear change in magnetic permeability μ. The uncertainty associated with the applied μ-T-function was identified as the primary factor for the resulting deviations above 15% in the temperature field solution.

Utilizing non-magnetic SiSiC ceramic reduced the complexity of the simulation procedure since it only required consideration of temperature-dependent electric conductivity. This reduction enabled more accurate calculations of the temperature field solution, even for system-scale design studies conducted above the Curie point. In addition, SiSiC had a beneficial SiO_2 insulation layer, developing during the sintering process and operation at high temperatures through its reaction with oxygen. This insulation layer established the applied core assumption of electrically insulated particles. Furthermore, such a high-temperature-resistant material has a notable structural strength even at temperatures exceeding 1000 °C, effectively preventing plastic deformation. Therefore, the validity of the numerical model extended to high-temperature and paramagnetic materials, particularly the SiSiC ceramic, due to its ability to form and maintain an electrically insulated SiO_2 layer.

Although the experiments and simulations were conducted at atmospheric pressure instead of the costly pressure setting of up to 15 bar typically employed in the Brayton heat pump, the results obtained for the validation using the atmospheric laboratory setting are considered valid because the pressure setting does not affect the electromagnetic field solution. In contrast, the system pressure influences the temperature field solution through convective heat transfer to the airflow. This effect is considered using a WF database implemented into the numerical and simplified system model to account for the pressure- and temperature-dependent fluid conditions.

Therefore, this discussion confirms the validity of the numerical model for temperatures below the Curie point when using ferromagnetic materials and for higher temperatures when using paramagnetic materials, as long as the assumption of electrically insulated particles is established. This assumption is particularly ensured when utilizing SiSiC, which has theoretically demonstrated a high PtH efficiency and remarkable power

density with the inductively heated PB concept. However, practical confirmation of the improved EFH performance using SiSiC across various pressure and high-temperature conditions requires further concept validation, including developing and testing a novel high-temperature gasket concept. Therefore, further research should focus on concept validation in a pressurized vessel above 1000 °C.

3.2 Meso scale: High-temperature induction air heater

The discussion on the meso scale first evaluates the validity and limitations of the introduced dimensionless modeling approach, referred to as the Φ-Λ-St model developed in Sec. 2.3 for time-efficient design studies on the system scale. The meso scale also presents a novel method for a thermodynamic comparison and characterization of various EFH concepts. This method was exemplarily applied to compare the laboratory induction air heater concept with industrial EFH solutions. Finally, practical implications for an industrial use case are revealed based on previous findings from the comparison, with the potential to push the state of the art boundaries in high-temperature electrical flow heaters.

3.2.1 Model verification: Suitability of the simplified model

The two-phase continuum Φ-Λ-St model with implemented heat source introduced in Sec. 2.3 effectively characterizes the EFH's thermodynamic behavior using four dimensionless parameters. This number of parameters was reduced when thermal losses to the ambient were neglected, assuming an adiabatic operation without heat losses to the ambient using a heat loss number $\Gamma = 0$. Consequently, the heat source

number Φ, the heater length Λ, and the Stanton number[2] St are key technical parameters for the general characterization of EFH:

$$\Phi = \frac{\dot{Q}_{\mathrm{PtH}}}{V_{\mathrm{EFH}}(1-\varepsilon)ka_vT_{\mathrm{f,in}}} = \frac{\dot{q}_{\mathrm{vol,PtH}}}{ka_vT_{\mathrm{f,in}}} \tag{3.1}$$

$$\Lambda = \frac{ka_vH}{w_f\varepsilon\overline{\rho}_f\overline{c}_{p,f}} \tag{3.2}$$

$$St = \frac{ka_v\tau}{\overline{\rho}_s\overline{c}_{p,s}} \tag{3.3}$$

where $\dot{Q}_{\mathrm{PtH}}$ denotes the electrically generated heat inside the component's heating volume V_{EFH} according to the heat balance from Figure 2.2, a_v is the specific heat transfer area, and k represents the heat transfer coefficient to the porous EFH media with the void fraction ε. In addition, w_f gives the average value for air velocity, H represents the heater length, τ gives the time the heater needs to achieve a thermodynamic steady state, and $\overline{\rho}_s$ and $\overline{c}_{p,s}$ denote the averaged density and heat capacity of the solid heating elements, respectively.

The simplified continuous model describes the thermodynamic behavior of the EFH with a temperature profile discretized in time and space. Heat transfer and pressure loss phenomena are represented by Nusselt and pressure loss correlations for the specific EFH concept using Λ and St numbers. The heat source number Φ characterizes the heating method with the applied heat source $\dot{Q}_{\mathrm{PtH}}$ specified by the volumetric

[2]The Stanton number represents here the heater dynamics quantified as the normalized duration that a heater needs to achieve thermodynamic steady state condition.

power density $\dot{q}_{\mathrm{vol,PtH}}$. This scalar was formulated for the inductively heated PB concept in Sec. 2.2.4.3, aiming to implement it into the continuum of the solid phase. Moreover, this compact formulation was successfully validated when applied to the numerical model for steel. Its applicability extends to high-temperature design studies using SiSiC due to the discussed validity of the assumed electrically insulated PB. Hence, the heat transfer and heat generation phenomena can be accurately described within the validity limits of the corresponding characteristic numbers (Nu, St) for a PB adequately represented through a continuum using this modeling approach. This approach was effectively verified with the continuous solid phase model introduced by Ismail et al. [47].

Furthermore, the Φ-Λ-St model was validated considering the heat loss mechanism with $\Gamma \neq 0$ in a parallel master's thesis [46]. The validation study demonstrated that the novel modeling approach overestimated the outlet temperature by a maximum of 8.7% at air outlet temperatures above 900 °C. Concludingly, the validated Φ-Λ-St model serves as a suitable and compact design tool for accurately predicting the thermodynamic performance of EFH concepts, with an error of up to 10% when considering heat losses to the ambient. Neglecting these heat losses results in higher errors, it is estimated up to 20%. Nevertheless, this novel EFH model remains a practical and time-efficient design tool for basic design studies of EFH concepts. For more detailed and precise design calculations, the application of the numerical model from Sec. 2.2 is recommended.

3.2.2 Comparison with existing electric air heaters

The inductively heated PB air heater concept was compared with existing electric air heater concepts in the industry to evaluate the performance of the elaborated EFH design solution beyond the scope of this thesis. This comparison specifically focusses on atmospheric heater

concepts, considering the insights from Sec. 3.1.2. The discussion from the previous section revealed that the dimensionless Φ-Λ-St model was a suitable tool for comparing and characterizing EFH concepts. Hence, the introduced characteristic parameters Φ, Λ, and St ensured a general comparison between heaters of different sizes, power levels, and heating technologies. To this end, technical data on industrial EFH designs and experimental data from Sec. 2.2 were collected and processed by the Φ-Λ-St model to calculate their dimensionless parameters.

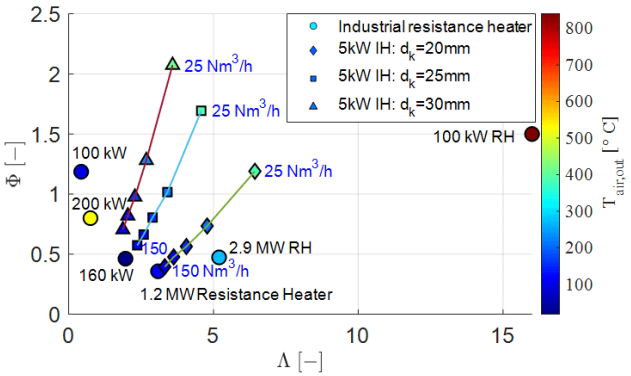

Fig. 3.2 Comparison and characterization of electric air heater concepts using the Φ-Λ-St model from Sec. 2.3 with neglected heat losses ($\Gamma = 0$).

Figure 3.2 presents the obtained parameter values for EFH design solutions working at steady-state temperature conditions. However, as the Stanton number characterizes the transient heater behavior, this parameter is irrelevant to the discussion of steady-state conditions. The dimensionless heat source number Φ is a metric for the performance of the EFH solution, indicating the ratio of electrically generated to the transferred heat. This parameter is set in relation to the dimensionless heater length Λ which is a metric for the compactness of the heater

solution. Consequently, EFH design solutions characterized by high Φ and small Λ numbers represent compact and powerful heater systems.

Figure 3.2 compares industrial resistant heater designs with three experimental design solutions (20 mm, 25 mm and 30 mm particle diameters) of the inductively heated PB from Sec. 2.2 using varying flow conditions with five different flow rates (25–150 Nm^3/h). In contrast to the industrial resistance heaters typically having a small Φ due to a volumetric power density below 1 MW/m^3 [48], the laboratory induction air heater demonstrated high Φ values, attributed to the intense electric power density of induction heating, resulting in significantly higher performance.

Moreover, the laboratory induction air heater demonstrated a reduced PtH efficiency of slightly higher than 80%, primarily caused by ohmic losses inside the induction coil. Though larger induction heating systems are beneficial in terms of efficiency, the PtH efficiency of the utility-scale induction heater design revealed in Sec. 2.4 and discussed in Sec. 3.1.2 was limited to 85%–87%. In contrast, resistance heaters have a significantly higher PtH efficiency of up to 95%–98% because external cooling of the tubular heating elements is unnecessary. However, a steady air flow at the heating area must be ensured to limit the heating temperature and to prevent damage to the metallic conductors. The service life of the heating conductor strongly depends on the cyclic heat-up times and process temperatures: to ensure a prolonged service life with 200,000 operating hours, it is necessary to limit the temperature to 800 °C for embedded and to 700 °C for freely radiating conductors, using common high-temperature resistant NiCr 8020 conductors [48]. The service life of the metallic heating conductor decreases exponentially with higher process temperatures. For example, the high-temperature technology of freely radiating conductors can only

achieve 10,000 operating hours at 900 °C, compared to the 200,000 operating hours at 700 °C [48].

On the contrary, contactless power transmission with the demonstrated high power density using an electrically decoupled induction coil ensures higher heating element temperatures without the risk of a shutdown. Furthermore, the combination with a high-temperature resistant SiSiC material offers a higher service life for the first time even at heating element temperatures above 900 °C thanks to the SiO_2 oxidation protection layer. The temperature limitation is then given close to the melting point of silicon at approximately 1400°C because of negative effects on service life and efficiency. Reaching this melting temperature, the service life reduces because the SiO_2 protection layer would dissolve. In addition, the melted phase would change the electrical conductivity, negatively affecting efficiency. Nevertheless, the PtH efficiency is supposed to be above 80% at 1000–1300 °C.

Despite the drawback of the lower PtH efficiency, induction air heaters achieve a notably higher element temperature and a longer lifetime compared with the high efficiency of resistance heaters. Therefore, the proposed SiSiC-based induction air heater concept is a unique EFH solution for air heating purposes above 900 °C, which extends the existing knowledge and state of the art in the field of EFH. Notably, resistive-heated SiC elements are already applied in industrial furnaces to combine the benefits of high lifespan and high efficiency at temperatures exceeding 1400 °C [49]. However, their application is limited to furnace heating via thermal radiation, which lies outside the scope of this work.

Altogether, the comparison between resistance heating and induction heating solutions, relying on the novel Φ-Λ-St approach, revealed a higher technical potential for the proposed SiSiC-based induction air

heater concept due to a significantly higher operating temperature together with a longer lifetime, albeit with a limited efficiency of 87%.

3.2.3 Practical implications for an industrial application

In addition to the high operating temperature and longer lifetime, the upscaled SiSiC-based induction air heater designs from Sec. 2.4 revealed compact and cost-efficient design solutions that can be applied in air-circulation furnaces instead of traditional fossil-fired burners to reduce greenhouse gas emissions in the ceramics, brick, and cement industries.

Natural gas-fired air-circulation furnaces are employed for heat treatment processes at atmospheric conditions and comprise the furnace chamber, the air-circulation system using a circulation fan, the natural gas burner, the high-temperature insulation, the furnace housing, and the control and regulation system. They are specifically designed to provide efficient convective heat transfer, resulting in a uniform temperature distribution in metallic and ceramic parts. High-temperature circulating fans are incorporated inside the furnace chamber to maintain the desired temperature uniformity. The heating process is achieved through one central or multiple heater units, which raise the air temperature or other process gases to the required operational level, reaching temperatures of up to 950 °C.

The developed induction air heater solution presents a competitive alternative to natural gas-fired burners, providing high-temperature process heat of up to 1050 °C for manufacturing bricks, sintering ceramic components, and cement clinker production [34]. The substitution with the induction air heater offers the user cost savings in operational expenditures (OPEX) using low-cost electricity from renewable energy

sources while avoiding CO_2 certificate expenses. Furthermore, the techno-economic assessment on a macro or utility scale (see Sec. 2.4) reveals competitive CAPEX of 160 €/kW with an estimated uncertainty of 20%. This cost-efficiency is attributed to the scalability and industrial availability of utility-scale induction technology combined with the scalable and low-cost PB setup. Hence, the inductively heated PB heater can replace existing natural gas burners and contribute to the decarbonization of industrial high-temperature process heat.

Nevertheless, the practical implementation of the developed induction PB air heater has certain limitations for an industrial application in an air-circulation furnace. The primary limitation concerns the maximum operating temperature of the SiSiC material, which is below 1400 °C, and the associated PtH efficiency with a maximum of 87%, as discussed in previous sections. Another limitation arises from the notable pressure loss experienced, especially when using small particle diameters in the PB for atmospheric heating applications. Industrial air-circulating fans must be employed to overcome this pressure loss. However, these are limited to 160 mbar pressure lift [50].

Furthermore, this thesis only investigated the vertical PB setup to prevent the formation of an air gap between the PB and the inner wall of the ceramic tube caused by gravity and cyclic thermal extension. A horizontal setup would result in such an air gap, promoting a parasitic airflow that does not interact with the PB thermally. Consequently, practical settings are limited to vertical column setups, imposing restrictions on the operational capability of the PB heater concept. Concerning these limitations, there is still significant potential for applying the presented induction air heater solution in air-circulation furnaces, specifically in tunnel kilns for brick production, confirming its suitability for industrial high-temperature heating applications.

The discussion regarding the substitution potential and associated limitations in the air-circulation furnace reveals further research opportunities for advancements in the induction air heater. In certain system integration scenarios, e. g. in a tunnel kiln, there may be a need for a horizontal setup with minimal pressure loss, which cannot be achieved with the current inductively heated PB concept. Therefore, developing novel induction heater concepts in combination with the identified SiSiC material is important to address such system integration requirements. Two promising solutions may be the inductively heated honeycomb concept disclosed together with the PB concept in WO2020239288A1 and the utilization of resistively heated SiC rod bundles for EFH applications. However, a detailed cost analysis aiming at cost reduction is crucial to promoting the profitability and deployment potential of these induction air heater concepts in industrial applications.

3.3 Macro scale: Brayton CB system with PtH extension

This section first interprets the quantified influence of PtH on the Brayton CB system from a technical perspective and gives insights into the relationship between various technical key metrics used on a macro scale. Secondly, the tradeoff between system costs and RTE is discussed concerning the central research question and other techno-economic studies. This comparison finally contributes to validating the main hypothesis and provides practical implications for other heating techniques that can be alternatively integrated into the Brayton CB to achieve the central objective of cost reduction.

3.3.1 Significance of the technical system evaluation

The relevance of the methodology used for the techno-economic study in Sec. 2.4 lies in its reliance on the identified technical key performance metric, discharged specific technical work w_t, rather than solely relying on cost data. Techno-economic studies typically involve uncertainties associated with cost data, which in this study was estimated to be up to 20%. By utilizing the specific technical work as a key parameter, this methodology provided a valuable approach that principally supports the techno-economic assessment, offering an in-depth understanding of the system's performance and cost implications.

Hence, a fundamental thermodynamic analysis was conducted in two steps, to investigate the correlation between the external high-temperature heat and the technical key performance metrics such as w_t and RTE. The first step involved an idealized thermodynamic cycle analysis, which served as a technical foundation to gain a basic understanding of the principal influence of an additional heat source on w_t. Subsequently, the second step focused on establishing the relationship between w_t and RTE.

The idealized thermodynamic cycle analysis presented in Sec. 2.4.2.2 showed the relationship between the maximum system temperature $T_{3,EFH}$, caused by utilizing a generic heat source, and w_t. The analysis additionally showed that the increase in the maximum system temperature $T_{3,EFH}$ through the electrically supplied heat increased the discharged technical work while decreasing the mass flow rate $\dot{m}_F$ for a constant power output of the system. The mass flow rate can be used as another technical metric as well, establishing the following relationship between the PtH heating capacity and both system's metrics:

$$P_{\mathrm{PtH}} \sim w_t \sim \dot{m}_F^{-1} \tag{3.4}$$

This finding with a sound thermodynamic basis clarifies that the temperature rise of $T_{3,EFH}$ enhances the system's energy density and benefits the discharged technical work, which is inversely proportional to the mass flow rate. Hence, a higher energy density aligns with higher discharged technical work and reduces the system's mass flow rate, providing the potential for component reduction with associated cost reduction.

Although the idealized cycle analysis revealed the general thermodynamic behavior of the discharged technical work and mass flow rate, it could not predict the RTE due to the utilization of idealized thermal components and the assumption of ideal gas behavior. Thus, a detailed thermodynamic analysis was conducted to address these limitations, considering the real gas properties of the WF and using component-specific definitions of component efficiencies. The increase in discharged specific technical work caused by isobaric heating with an external heat source was found to correlate linearly with the RTE using the following relationship:

$$w_t^{-0.5} \sim \eta_{rt} \tag{3.5}$$

Consequently, the combination with the relationship from Eq. (3.4) gives the relationship for the decrease of RTE when utilizing an additional electrical heat source P_{PtH} in the system. Thus, the RTE is inversely proportional to P_{PtH} and establishes a similar relationship to w_t.
Overall, the presented adoption of the discharged specific technical work as a key performance metric for cost analysis establishes a technically sound basis for further discussion of cost effects.

3.3.2 Tradeoff between round-trip efficiency and system cost

Utilizing the discussed technical approach with a techno-economic analysis further revealed a linear correlation of the discharged specific technical work with the system CAPEX using the following relationship:

$$C_{CAPEX} \sim w_t^{-0.5} \tag{3.6}$$

Consequently, cost results were presented together with the introduced expression $w_t^{-0.5}$ in the wide-ranged parameter study from Sec. 2.4.5.3, providing a robust technical justification for the findings based on this technical key performance metric. The comparison of $w_t^{-0.5}$ and CAPEX with the RTE η_{rt} clearly demonstrated the relationship among these metrics, in particular for system design solutions indicating a RTE above 40%. This technical metric linearly correlates with the system CAPEX:

$$\eta_{rt} \sim C_{CAPEX} \tag{3.7}$$

Hence, this proportionality proves that a reduction in CAPEX is only attainable with a reduction in RTE, demonstrating that the tradeoff was quantified in the bar graph from Sec. 2.4.5.3. This graph clearly shows the linear decrease of both the CAPEX (from 360 €/kWh$_{el}$ to 277 €/kWh$_{el}$) and RTE (from 51.7% to 49.2%) for an increasing electrical heating capacity of a maximum of 17 MW$_{el}$. At that specific design point, the CAPEX for the 30 MW$_{el}$ and 210 MWh$_{el}$ Brayton CB systems indicate a linear cost savings of 30 €/kWh$_{el}$ for every percentage point loss in RTE. This energy-specific cost saving can be further enhanced to nearly 60 €/kWh/1% pt. RTE by implementing a heating capacity of 27 MW$_{el}$ resulting in a further efficiency reduction of 41% RTE.

This techno-economic analysis underlined with the technical approach using the specific technical work w_t can allow researchers and stakeholders to make a straightforward evaluation of CAPEX, particularly when applying the introduced linear cost function (Eq. [30] from Sec. 2.4.5.1) based on w_t for future investigations and investment decisions. Moreover, the parameters p and c of the linear CAPEX function from Eq. (30) can be customized to consider changes in the cost structure resulting from fluctuations in commodity prices and other cost-driven factors to ensure accurate future cost estimations. Overall, the proposed methodology allows for more reliable decision-making by researchers and stakeholders while offering flexibility to customize the cost estimation function.

The impact of cost reduction at the expense of RTE has been examined in previous studies, such as [33] for A-CAES and [35] for a hybrid storage system incorporating HT-PTES with an ORC cycle. For example, Benato [35] presented a similar idea for cost reduction by implementing an EFH downstream of the HP compressor. The author assumed heater equipment costs of up to 850 €/kW without specifying the heating method or heater design. Nevertheless, cost expressions from Benato's work were applied in the system model outlined in Sec. 2.4 to verify the robustness of the main outcomes of this study using independent cost functions. This robustness check confirmed the main cost reduction outcome by incorporating additional electrical heating capacity. However, Benato's cost function for the EFH indicated a notably higher equipment cost than the 160 €/kW for the utility-scale induction air heater. Although Benato's electric heating component had significantly higher costs at around 850 €/kW, the results still confirmed the cost reduction effect. However, this effect diminished at the marginal cost of approximately 950 €/kW, resulting in higher system CAPEX and lower RTE. Consequently, the tradeoff between

CAPEX and RTE was only established for heater costs below 950 €/kW. This marginal cost is high enough to cover most heating technologies.

3.3.3 Practical implications for alternative heating technologies

Instead of integrating a PtH component upstream of the HT-STES into the heat pump cycle, the discussed elevation of the maximum system temperature $T_{3,EFH}$ can alternatively be achieved by incorporating a natural gas or hydrogen-fired air heater in the heat engine cycle downstream of the HT-STES. While these alternative heating methods, which are beyond the scope of this thesis, are expected to yield similar effects and outcomes, there is a notable difference: the HT-STES embraces a lower energy density, leading to higher equipment costs than the supply of HT heat for the HT-STES using an EFH during the heat pump cycle. On the other hand, while a natural gas burner has lower CAPEX than the EFH, its operation causes CO_2 emissions, which have a negative environmental impact and lead to additional CO_2 certificate expenses. Therefore, a hydrogen-fired air heater may be an alternative heating method providing external HT heat without CO_2 emissions. However, the operational expenses are highly dependent on the hydrogen price and its availability. Therefore, this alternative heating method requires additional techno-economic analysis to evaluate its cost effectiveness for the application in the Brayton CB.

The ability to provide electrical heating capacity on the order of megawatts with high start-up times enables the EFH to participate in secondary reserve markets to generate additional revenue for the operator. Thus, integrating EFH allows project stakeholders and operators to flexibly maximize the revenue potential and minimize the amortization period of the EES system by optimizing both CAPEX and RTE.

3.4 Conclusions and outlook

This section gives the outcomes of the leading objectives and uses them to evaluate the main hypothesis of this work. To this end, it interprets the quantified impact of PtH on system cost and RTE related to the central research question and discusses the resulting tradeoff. Furthermore, it concludes the discussion about the elaborated EFH solution and its suitability for high-temperature applications in Brayton CB and practical industrial settings.

The previous discussion revealed remarkable cost reduction potential for incorporating a high-temperature induction air heater outweighing the minor penalty on the RTE. This discussion validates the main hypothesis by providing evidence of the economic viability of the elaborated induction air heater design solution and its potential to enhance the overall performance of the Brayton CB system. Furthermore, a comparison with findings from other techno-economic studies provided further evidence of the consistency and significance of the observed tradeoff between CAPEX and RTE, confirming the validity of the main hypothesis. This tradeoff requires accurately evaluating the balance between cost reduction and maintaining an acceptable RTE. To provide an optimal balance, further research and development efforts should focus on optimizing the PtH integration and investigating alternative heating technologies, such as hydrogen-fired air heaters, including conducting advanced design studies for the heater component and investigating techniques to mitigate the negative impacts on RTE or exploit heat losses for an improvement in system efficiency.

The discussion at the meso scale concluded that the elaborated induction air heater design based on a compact SiSiC PB is well-suited for the high-temperature application in the Brayton CB and industrial process heat. The proposed induction air heater design has proven to be a cost-

efficient utility-scale PtH solution due to its compactness, demonstrating power densities up to 4.5 MW/m^3 with a maximum PtH efficiency of 87%. Despite the drawback of the lower PtH efficiency, this EFH concept achieves a notably higher element temperature and a longer lifetime compared to available resistance air heaters with up to 98% PtH efficiency and power density below 1 MW/m^3. Therefore, the proposed SiSiC-based induction air heater concept is a unique EFH solution for air heating purposes above 900 °C, which extends the existing knowledge and state of the art in the field of EFH.

Furthermore, the discussion about practical implications provided valuable insights into the applicability and associated limitations of the inductively heated PB solution in a practical industrial setting, where the air-circulating tunnel kiln was proposed as a suitable industrial application for a retrofit of natural gas burner with the novel EFH solution. However, the practical implementation of the developed induction PB air heater has certain limitations for an industrial application in air-circulating furnaces, particularly its employment in a vertical PB setup. Hence, further research should focus on developing novel horizontal induction heater settings combined with the identified SiSiC material to address such system integration requirements.

Chapter 4

Summary

Developing new storage technologies for utility-scale EES is crucial in future flexible electricity transmission systems. Indeed, electricity storage in the Brayton CB can substantially contribute to this goal. For further improvements in system flexibility and cost-efficiency, modifications of the partial adiabatic process are presented utilizing PtH inside the heat pump cycle.

The underlying idea of this work is to provide high-temperature heat by incorporating an induction air heater component downstream of the heat pump compressor of the Brayton CB to enhance the energy density of the system and consequently reduce CAPEX. In addition to the heat produced through compression, high-temperature heat is generated using induction heating and transported to HT-TES during the charging cycle. Consequently, the increased energy density enables a decrease in component size, resulting in a cost reduction. The main drawback of PtH integration is the reduction in RTE caused by the lower coefficient of performance during the charging cycle on the one

hand and the limited Carnot efficiency of the gas turbine cycle on the other.

The leading objectives of this work are to quantify the tradeoff between system CAPEX and RTE arising from the integration of the additional induction heating while providing novel design solutions for such a high-temperature electric heater component. To this end, a multi-scale approach was applied to address these objectives on the micro, meso, and macro scales, where technical key requirements were defined on the macro scale and passed on to lower scales, ensuring application-specific heater technology development.

Firstly, the model-based technological development on the micro and meso scales revealed the inductively heated pebble bed air heater concept in combination with SiSiC ceramics as a favorable high-temperature PtH solution. The investigated induction air heater design demonstrated power densities up to 4.5 MW/m^3 with a PtH efficiency of 80% at the laboratory scale and a maximum of 87% at the meso scale. The experimental results were used to validate the numerical multi-physics model and prove the suitability of this novel heater solution for application in the Brayton CB.

The techno-economic analysis on a macro scale was conducted for a Brayton CB air system with 210 MWh of energy storage capacity. Component models for the central components, including the revealed induction air heater solution, were developed on the meso and macro scales. Finally, these component models were implemented in the system model with associated cost functions to investigate the closed-loop Brayton CB under cyclic steady-state operating conditions.

The techno-economic study revealed that integrating a compact SiSiC-based induction air heater downstream of the heat pump compressor is

a highly cost-effective approach to reducing system CAPEX. However, integrating the additional high-temperature heat at a maximum of 1050 °C is associated with a loss in RTE. Therefore, a tradeoff was observed between RTE and system CAPEX, wherein the system CAPEX was significantly reduced by 23% to 277 €/kWh with a penalty in RTE of 5% to 49.2%.

The findings validated the study's main hypothesis, revealing the significant cost advantage of integrating a compact electric air heater in the Brayton CB. However, it is crucial to further address the tradeoff with RTE and conduct advanced design optimization studies for the heater component, investigating techniques to mitigate the negative impact on RTE and achieve an optimal balance between cost and efficiency.

Altogether, the research contributions provided valuable insights into developing and integrating the induction air heater solution for high-temperature applications in the Brayton CB and industrial furnaces for retrofitting natural gas-fired systems. The discussion revealed that the proposed SiSiC-based induction air heater concept is a unique PtH solution for air heating above 900 °C, extending the existing state of the art in this field. These findings further strengthen the focus of research efforts on industrial PtH applications and pave the way for future advancements in cost-efficient and energy-efficient Brayton CB systems.

References

[1] REN21, P. R. S. (2022). Renewables 2022 global status report. Renewable Energy Policy Network for the 21st Century (REN21) [Online]. Available: https://www.ren21.net/wp-content/uploads/2019/05/GSR2022_Full_Report.pdf.

[2] McPherson, Madeleine, and Samiha Tahseen. "Deploying storage assets to facilitate variable renewable energy integration: The impacts of grid flexibility, renewable penetration, and market structure." Energy 145 (2018): 856-870.

[3] World Energy Council. (2016). E-storage: shifting from cost to value—wind and solar applications.

[4] International Energy Association. (2019). Tracking energy integration.

[5] Xue, Haobai, and Alexander White. "A comparative study of liquid, solid and hybrid adiabatic compressed air energy storage systems." Journal of Energy Storage 18 (2018): 349-359.

[6] Luo, Xing, et al. "Overview of current development in electrical energy storage technologies and the application potential in power system operation." Applied energy 137 (2015): 511-536.

[7] Olympios, Andreas V., et al. "Progress and prospects of thermo-mechanical energy storage—a critical review." Progress in Energy 3.2 (2021): 022001.

[8] Jülch, Verena. "Comparison of electricity storage options using levelized cost of storage (LCOS) method." Applied energy 183 (2016): 1594-1606.

[9] Smallbone, Andrew, et al. "Levelised Cost of Storage for Pumped Heat Energy Storage in comparison with other energy storage technologies." Energy Conversion and Management 152 (2017): 221-228.

[10] Murray, C.. (2023). Construction starts on first utility-scale BESS projects in Idaho. Enregy Storage News [Online]. Mach, 9th 2023. Available: https://www.energy-storage.news/construction-starts-on-first-utility-scale-bess-projects-in-idaho/

[11] Pritil Gunjan, Maria Chavez, Dan Power (2022). Vanadium Redo Flow batteries [Online]. Available: https://vanitec.org/images/uploads/Guidehouse_Insights-Vanadium_Redox_Flow_Batteries.pdf

[12] Dumont, Olivier, et al. "Carnot battery technology: A state-of-the-art review." Journal of Energy Storage 32 (2020): 101756.

[13] Vecchi, Andrea, et al. "Carnot Battery development: A review on system performance, applications and commercial state-of-the-art." Journal of Energy Storage 55 (2022): 105782.

[14] Novotny V, Basta V, Smola P, Spale J. Review of Carnot Battery Technology Commercial Development. Energies. 2022; 15(2):647. https://doi.org/10.3390/en15020647

[15] A. Benato, A. Stoppato, Pumped Thermal Electricity Storage: a technology overview, Thermal Science and Engineering Progress (2018), doi:https://doi.org/10.1016/j.tsep.2018.01.017

[16] Rabi, Ayah Marwan, Jovana Radulovic, and James M. Buick. "Comprehensive review of compressed air energy storage (CAES) technologies." Thermo 3.1 (2023): 104-126.

[17] Budt, M., Wolf, D., Span, R., Yan, J.. A review on compressed air energy storage: Basic principles, past milestones and recent developments. Applied Energy 2016;170:250–268. doi:10.1016/j.apenergy.2016.02.108

[18] De Sisternes, F. J., Jenkins, J. D., and Botterud, A., 2016, "The Value of Energy Storage in Decarbonizing the Electricity Sector," Applied Energy, 175, pp. 368–379.

[19] Barnhart, Charles J., et al. "The energetic implications of curtailing versus storing solar-and wind-generated electricity." Energy & Environmental Science 6.10 (2013): 2804-2810.

[20] Houssainy, S., Janbozorgi, M., & Kavehpour, P. (2018). Thermodynamic performance and cost optimization of a novel hybrid thermal-compressed air energy storage system design. Journal of Energy Storage, 18, 206-217. https://doi.org/10.1016/j.est.2018.05.004

[21] F. Marguerre, Über ein neues Verfahren zur Aufspeicherung elektrischer Energie, Mitteilungen der Vereinigung der Elektrizitatswerke 354 (1924) 27–35.

[22] B. Weissenbach, Thermal energy storage device, patent No. EP/0003980 A1 (1979).

[23] J. Ruer, "Installation and methods for storing and recovering electrical energy," 2008. WO/2008/148962 A2

[24] J. MacNaghten and J. S. Howes, “Energy Storage,” no. WO2009044139 A2, 2009.

[25] Desrues, T., Ruer, J., Marty, P., Fourmigué, J.. A thermal energy storage process for large scale electric applications. Applied Thermal Engineering.

[26] Howes, Jonathan. "Concept and development of a pumped heat electricity storage device." Proceedings of the IEEE 100.2 (2011): 493-503.

[27] White, Alexander, Geoff Parks, and Christos N. Markides. "Thermodynamic analysis of pumped thermal electricity storage." Applied Thermal Engineering 53.2 (2013): 291-298.

[28] White, Alexander J. "Loss analysis of thermal reservoirs for electrical energy storage schemes." Applied energy 88.11 (2011): 4150-4159.

[29] McTigue, Joshua D., Alexander J. White, and Christos N. Markides. "Parametric studies and optimisation of pumped thermal electricity storage." Applied Energy 137 (2015): 800-811.

[30] Ameen, Muhammad Tahir, et al. "Demonstration system of pumped heat energy storage (PHES) and its round-trip efficiency." Applied Energy 333 (2023): 120580.

[31] S. Zunft, V. Dreissigacker, M. Bieber, A. Banach, C. Klabunde and O. Warweg, "Electricity storage with adiabatic compressed air energy storage: Results of the BMWi-project ADELE-ING," in Proc. 2017 International ETG Congress, Bonn, Germany, pp. 1-5.

[32] Zunft, S., Krüger, M., Dreißigacker, V., Belik, S., Hahn, J., & Knödler, P. (2017). ADELE-ING: Engineering-Vorhaben für die

Errichtung der ersten Demonstrationsanlage zur adiabaten Druckluftspeichertechnik: official report. Ed. Züblin AG. Stuttgart

[33] Dreißigacker, Volker, and Sergej Belik. "System Configurations and Operational Concepts for Highly Efficient Utilization of Power-to-Heat in A-CAES." Applied Sciences 9.7 (2019): 1317.

[34] Singh, Ranjit, R. P. Saini, and J. S. Saini. "Simulated performance of packed bed solar energy storage system having storage material elements of large size-Part I." The Open Fuels & Energy Science Journal 1.1 (2008).

[35] Benato, Alberto. "Performance and cost evaluation of an innovative Pumped Thermal Electricity Storage power system." Energy 138 (2017): 419-436.

[36] Chen, Long Xiang, et al. "Thermodynamic analysis of a high temperature pumped thermal electricity storage (HT-PTES) integrated with a parallel organic Rankine cycle (ORC)." Energy Conversion and Management 177 (2018): 150-160.

[37] Sergio, L. Fundamentals of Electroheat. In Electrical Technologies for Process Heating; Springer: Cham, Switzerland, 2017.

[38] Schniewindt. Flow Heaters, https://www.schniewindt.de/en/csn-flow-heaters/ [Online]; 2021 [Available]

[39] Ohmex. Electrical Process Flow Heaters datasheet, https://www.ohmex.de/en/wp-content/uploads/sites/3/2020/03/electric-process-heater_STR_2020-03.pdf; [Online]; 2021 [Available]

[40] From: Frogner, K., Andersson, M., Cedell, T., Siesing, L., Jeppsson, P., & Ståhl, J. E. (2011). Industrial heating using energy

efficient induction technology. In Proceedings of the 44th CIRP International Conference on Manufacturing Systems (pp. 01-03).

[41] Lupi, S.; Michele, F.; Aleksandr, A. Induction and Direct Resistance Heating; Springer: Cham, Switzerland, 2015.

[42] Unver, U.; Yuksel, A.; Kelesoglu, A.; Yuksel, F.; Unver, H.M. Analysis of a novel high performance induction air heater. Therm. Sci. 2018, 22 (Suppl. 3), 843–853.

[43] Unver, U. Efficiency analysis of induction air heater and investigation of distribution of energy losses. Teh. Vjesn. 2016, 23, 1259–1267. https://doi.org/10.17559/TV-20151122224719.

[44] Proceeding of UIE 2021: XIX International UIE Congress on Evolution and New Trends in Electrothermal Processes. 1.-3.2021, Pilsen, Faculty of Electrical Engineering, University of West Bohemia, Czech Republic, 2021, p. 45-46

[45] Belik, Sergej (2015) Entwicklung von Konzepten der induktiven Erwärmung in thermischen Hochtemperatur-Energiespeichern. Masterarbeit, HS für Technik, Wirtschaft und Kultur Leipzig.

[46] Sommer, Kai (2021) Experimentelle Studie zur Modellparametrisierung eines induktiv beheizten Strömungserhitzers. Masterarbeit, Universität Stuttgart.

[47] Ismail, K. A., & Stuginsky Jr, R. (1999). A parametric study on possible fixed bed models for pcm and sensible heat storage. Applied Thermal Engineering, 19(7), 757-788

[48] Wagner, Walter. Heat Transfer Technique with organic fluids, Vogel Buchverlag, 2019. ProQuest Ebook Central, https://ebookcentral.proquest.com/lib/dlr-ebooks/detail.action?docID=5964116.

[49] Riesun. Hot bar 1600°C heating elements. Technical documentation. [Online]. Available: https://en.risesun.co/upload/file/1665456748.pdf

[50] Heavy duty industrial fans. TLT-Turbo. Technical documentation. 2019.